

Universidade de São Paulo
Instituto de Astronomia, Geofísica e Ciências Atmosféricas
Departamento de Astronomia

Gabriel de Oliveira Gomes

Equilibrium tides on planets and stars

São Paulo

2022

Gabriel de Oliveira Gomes

Equilibrium tides on planets and stars

Tese apresentada ao Departamento de Astronomia do Instituto de Astronomia, Geofísica e Ciências Atmosféricas da Universidade de São Paulo como requisito parcial para a obtenção do título de Doutor em Ciências.

Área de Concentração: Astronomia

Orientador: Prof. Dr. Sylvio Ferraz-Mello

Versão Corrigida. O original encontra-se disponível na Unidade.

São Paulo

2022

*Para meus pais
Alexandre e Viviane, por seu
amor, paciência e companhia*

Acknowledgements

Eu gostaria de agradecer a todas as pessoas que, de alguma forma, me ajudaram para que eu pudesse fazer esta tese.

A Deus, pela sua presença e guia constante em minha vida.

Ao Prof. Sylvio Ferraz-Mello pela oportunidade, orientação, apoio, paciência, confiança ao longo da realização deste trabalho e seus conselhos não somente limitados aos assuntos desta tese, que me moldaram ao longo destes maravilhosos quatro anos de estudo.

À Prof. Tatiana Michtchenko, pelas sugestões e discussões que aumentaram a qualidade deste trabalho.

À Professora Silvia Rossi e o Professor Ramachrisna Teixeira pelos excelentes cursos ministrados ao longo de meu doutorado, que serviram como base para várias discussões nesta tese.

Ao Professor Mariano de Souza e o Professor Tadashi Yokoyama, pelo interesse em minhas atividades e conselhos mesmo após o término de de minha Graduação.

À toda minha família, em particular meus primos Douglas, Débora, Lilian, Rafael e Caio e meus tios Fernando, Mônica, Carlos, Heliana, Edson e Valdina, pelo constante incentivo e interesse nos meus estudos.

Aos meus avós Marcos e Leonice, pelo seu constante apoio e conselhos.

Aos meus pais, pelo constante apoio incondicional às minhas decisões ao longo do meu doutorado.

Aos meus colegas de doutorado: Leonardo, Manu, Alex Segovia, Alex Revol, Raphael, Hugo, Eduardo e Irapuan, pelo incentivo e frutíferas discussões que, mesmo indiretamente, possam ter contribuído para este trabalho.

Aos meus amigos, os quais considero como parte da minha família: Isabela, Breno,

Flavio, Danyellen, Adriano, Monique e Lucas, pelos incentivos e constante interesse nos meus estudos.

Aos meus supervisores de estágio durante minha estadia no Observatório de Genebra, Emeline Bolmont e Sergi Blanco-Cuaresma, pelas discussões não só limitadas a marés mas também a outros assuntos de pesquisa, que contribuíram para meu desenvolvimento durante meu doutorado.

Ao pessoal do Observatório de Genebra pela recepção e apoio durante a minha estadia no ano de 2020.

À equipe de informática do IAG, pelo apoio sempre que era necessário.

À FAPESP, pelo apoio financeiro ao longo de todo este projeto de doutorado através dos processos 2017/25224-0 e 2019/21201-0.

Ao Instituto de Astronomia, Geofísica e Ciências Atmosféricas-IAG/USP por ter me dado todas as condições necessárias para a realização deste trabalho.

“It was Grandfather’s watch and when Father gave it to me he said I give you the mausoleum of all hope and desire; it’s rather excruciatingly apt that you will use it to gain the reducto absurdum of all human experience which can fit your individual needs no better than it fitted his or his father’s. I give it to you not that you may remember time, but that you might forget it now and then for a moment and not spend all your breath trying to conquer it.”

William Faulkner, *The Sound and the Fury*

“Porque para Deus nada é impossível.”

Lucas 1:37, A Bíblia Sagrada

Resumo

A maioria das aplicações atualmente feitas usando teorias de marés de equilíbrio são baseadas no uso de defasagens de maré *ad hoc*. Nos casos de aplicações feitas com a teoria clássica de Darwin, por exemplo, a previsão para o estágio final da evolução rotacional é o sincronismo para o caso de órbitas circulares e o supersincronismo para órbitas excêntricas (onde o excesso de rotação em relação ao sincronismo é dado por $\approx 6ne^2$, onde n é o movimento orbital médio e e é a excentricidade orbital). Recentemente, uma formulação para marés de equilíbrio que considera uma solução linearizada da equação de Navier-Stokes foi feita no IAG (ver Ferraz-Mello 2013, 2015). A teoria permite a descrição de marés de equilíbrio tanto em corpos rígidos (como super-Terras) quanto em corpos gasosos (como mini-Netunos e Júpiteres quentes) ajustando apenas um parâmetro, que é o coeficiente de viscosidade uniforme η .

A primeira versão da teoria da maré de fluência (ou seja, a versão proposta em Ferraz-Mello 2013, 2015) foi baseada em uma expansão em série da chamada equação de fluência. Nessa estrutura, a taxa de rotação do corpo deformado por maré foi considerada constante ao resolver a equação de fluência. Em seguida, a taxa de rotação foi evoluída considerando a expressão de torque relacionada às interações de maré. Este método não é consistente quando se trata da evolução da taxa de rotação do corpo deformado por maré. Uma das consequências de considerar a taxa de rotação constante para o corpo ao resolver a equação da fluência é que as librações da taxa de rotação no regime de rotação síncrona são muito pequenas para corpos rígidos. Este resultado é inconsistente com a amplitude de libração da taxa de rotação e o ângulo de defasagem das marés dos satélites planetários do Sistema Solar.

Uma nova formulação da teoria da maré de fluência foi proposta em Folonier et al.

(2018). A nova versão da teoria leva a um tratamento consistente da dinâmica de rotação do corpo deformado por maré, onde librações forçadas em torno da solução síncrona (que são características no caso de corpos rígidos, como super-Terras e satélites planetários) são reproduzidas. Além disso, a nova versão da teoria da maré de fluência permite um estudo da figura de equilíbrio do corpo deformado por maré de uma maneira muito mais simples do que a versão anterior da teoria. Nesta tese, apresentamos aplicações da teoria das marés de fluência a vários casos, onde são considerados tanto planetas gigantes gasosos quanto planetas rígidos semelhantes à Terra. Também discutimos em detalhes as diferenças entre a primeira versão da teoria da maré de fluência (ver Ferraz-Mello 2013, 2015) e a nova versão (ver Folonier et al. 2018).

Abstract

Most of the applications currently made using theories of equilibrium tides are based on the use of *ad hoc* tidal lags. In the cases of applications made using Darwin's classical theory, for example, the prediction for the final stage of rotational evolution is the synchronism for the case of circular orbits and the super-synchronism for eccentric orbits (where the excess rotation with respect to synchronism is given by $\approx 6ne^2$, where n is the orbital mean motion and e is the orbital eccentricity). Recently, a formulation for equilibrium tides that considers a linearized solution of the Navier-Stokes equation was made at IAG (see Ferraz-Mello 2013, 2015). The theory allows for the description of equilibrium tides in both stiff bodies (such as super-Earths) as well as gaseous bodies (such as mini-Neptunes and hot Jupiters) by tuning only one parameter, which is the uniform viscosity coefficient η .

The first version of the creep tide theory (i.e., the version proposed in Ferraz-Mello 2013, 2015) was based on a series expansion of the so-called creep equation. In such framework, the rotation rate of the tidally-deformed body was considered constant when solving the creep equation. Afterwards, the rotation rate was evolved by considering the torque expression related to the tidal interactions. This method is not consistent when it comes to the evolution of the rotation rate of the tidally-deformed body. One of the consequences of considering the constant rotation rate for the body when solving for the creep equation is that the librations of the rotation rate in the synchronous rotation regime are very small for stiff bodies. This result is inconsistent with the amplitude of libration of the rotation rate and the tidal lag angle of planetary satellites of the Solar System.

A new formulation of the creep tide theory was proposed in Folonier et al. (2018). The new version of the theory leads to a consistent treatment of the rotation dynamics of the

tidally-deformed body, where forced librations around the synchronous solution (which are characteristic in the case of stiff bodies, such as super-Earths and planetary satellites) are reproduced. Additionally, the new version of the creep tide theory allows for a study of the equilibrium figure of the tidally-deformed body in a much simpler way than the previous version of the creep tide theory. In this thesis, we present applications of the creep tide theory to several cases, where both gaseous giant planets as well as stiff Earth-like planets are considered. We also discuss in details the differences between the first version of the creep tide theory (see Ferraz-Mello 2013, 2015) and the new version (see Folonier et al. 2018).

List of Figures

2.1	Geometrical elements of the static equilibrium tide figure	28
2.2	Geometrical elements of the dynamic equilibrium tide figure	32
5.1	Evolution of a HJ for an initially fast-rotating M star	66
5.2	Evolution of a HJ for an initially slow-rotating M star	67
5.3	Evolution of a HJ for an initially fast-rotating K star	69
5.4	Evolution of a HJ for an initially slow-rotating K star	69
5.5	Evolution of a HJ for an initially fast-rotating G star	70
5.6	Evolution of a HJ for an initially slow-rotating G star	71
5.7	Evolution of a HJ for an initially fast-rotating F6V star	72
5.8	Evolution of a HJ for an initially slow-rotating F6V star	72
5.9	Evolution of a HJ for an initially fast-rotating F star	74
5.10	Evolution of a HJ for an initially slow-rotating F star	74
5.11	Period evolution tracks for M, K, G and F stars	75
5.12	Kepler exoplanets data on the periods diagram	76
5.13	Survival timescales as a function of the stellar relaxation factor	78
5.14	Relaxation factor values corresponding to the Q value determined by Penev et al.	81
7.1	Typical memory and concurrency problems in C and Fortran	97
7.2	Ownership and borrowing examples in Rust	98
7.3	Spin-orbit evolution of K2-265 b using Posidonius and secular evolution code	107
7.4	Case 1 for the spin-orbit evolution of the CoRoT-7 b-c system	109
7.5	Case 2 for the spin-orbit evolution of the CoRoT-7 b-c system	110

7.6	Case 3 for the spin-orbit evolution of the CoRoT-7 b-c system	110
A.1	Posidonius code main structure	143
A.2	Posidonius code functioning	144

List of Tables

5.1	Physical parameters of the stars used in the simulations	66
5.2	Linear fit coefficients for the G star case	79
7.1	Parameters for K2-265 b used in our numerical simulations	106
7.2	Currently estimated parameters for CoRoT-7 b-c	108

Contents

1. <i>Introduction</i>	21
2. <i>The creep tide theory</i>	25
2.1 Introduction	25
2.2 The static equilibrium tide	27
2.3 The dynamic equilibrium tide	29
2.3.1 The Navier Stokes equation approach	29
2.3.2 From the creeping motion to the creep equation	30
2.4 The parametric equations (Folonier et al., 2018)	31
2.5 The tidal forces and torques	33
3. <i>Rotation and figure evolution in the creep tide theory: a new approach and application to Mercury</i>	35
4. <i>Secular spin-orbit evolution of two-body systems</i>	57
4.1 Introduction	57
4.2 Orbital evolution equations	57
4.2.1 Free rotating bodies	58
4.2.1.1 Bodies in stationary rotation	59
4.3 Rotational evolution equations	59
4.4 The complete group of spin-orbit evolution equations	60
4.4.1 Star + hot Jupiter	61
4.4.2 Star + low-mass planet	63

5. <i>Spin-orbit evolution of hot Jupiters around M, K, G and F stars</i>	65
5.1 Introduction	65
5.2 Spin-orbit evolution of hot Jupiters around M, K, G and F stars	65
5.2.1 Evolution results for M star	66
5.2.2 Evolution results for K star	68
5.2.3 Evolution results for G star	70
5.2.4 Evolution results for a F6V star	71
5.2.5 Evolution results for a late F IV (subgiant) star	73
5.2.6 Comparison to Kepler exoplanetary systems	75
5.3 Survival timescale of hot Jupiters for M, K and G stars	77
5.3.1 Dependence on the relaxation factor and eccentricity	77
5.3.2 Discussions regarding the estimations of Penev et al. (2018)	79
6. <i>Tidal evolution of exoplanetary systems hosting potentially habitable exoplanets.</i>	
<i>The cases of LHS-1140 b-c and K2-18 b-c</i>	83
7. <i>The Posidonius N-body code and implementation of the creep tide equations</i>	95
7.1 Introduction	95
7.2 The Posidonius code	96
7.2.1 The Rust programming language	96
7.2.2 Numerical integration methods	98
7.2.2.1 The WHFast integrator (Rein and Tamayo, 2015)	98
7.2.2.2 The IAS15 integrator (Rein and Spiegel, 2015)	101
7.3 Implementation of the creep tide equations	104
7.4 Application: The K2-265 b planet	105
7.5 Application: The CoRoT-7 b-c system	107
7.6 Final considerations	111
8. <i>Influence of equilibrium tides on transit-timing variations of close-in super-Earths</i>	113
9. <i>Conclusion</i>	127
<i>Bibliography</i>	131

<i>Appendix</i>	139
<i>A. Structure and usage of Posidonius</i>	141
A.1 Installation of requirements	141
A.2 Installation of Posidonius	142
A.3 Code structure and functioning	142
A.4 Performing simulations	143
A.5 Plotting and analysing results	144

Introduction

Tidal interactions are essential for describing the spin and orbital evolution of close-in exoplanets¹. For more distant planets (i.e., the planets with orbital periods larger than 10 days), tides play an important role mainly on the spin evolution, with the timescale of tidal orbital evolution being much longer. In any of the two aforementioned cases, a key component concerning the tidal evolution of the systems is the chosen model for the tidal interactions.

In standard Darwin's theory (e.g., Darwin 1880) and its variations (see e.g., Kaula 1964; Mignard 1979; Ferraz-Mello et al. 2008), the gravitational potential of the deformed body is expanded in a Fourier series. The static component of the tide is then defined as the instantaneous response of the equilibrium figure of the deformed body to the time-varying position of the (point-mass) companion. Thus, the static tide corresponds to the limiting case of an inviscid body (i.e., a body with zero viscosity). The dynamic component of the tide is often introduced by considering exactly the same Fourier expansion procedure as the static tide, with the introduction of *ad hoc* lags on the arguments of the periodic terms of the Fourier expansion of the tidal potential.

All the aforementioned theories predict the existence of a stationary rotation. If the tidal lags are assumed to be independent of the tidal forcing frequencies (as in MacDonald 1964; Goldreich 1966), the stationary rotation rate is given by $\Omega_{\text{stat}} \approx n(1 + 9.5e^2)$. If the tidal lags are assumed to be proportional to the tidal forcing frequencies (e.g., as in Mignard 1979; Ferraz-Mello et al. 2008), the stationary rotation rate becomes $\Omega_{\text{stat}} \approx n(1 + 6e^2)$. There are three main aspects of these results which must be kept in mind: (i) there is

¹ For the purposes of this work, we will define close-in planets as the ones for which the orbital period is smaller than 10 days, while planets with periods larger than 10 days are defined as more distant planets.

no explicit dependence of the stationary rotation on the rheology of the body (e.g., the body's viscosity) and (ii) the theories predict that there are no other equilibrium states for the rotation rate in a coplanar eccentric system other than the pseudo-synchronism. Synchronous rotations or spin-orbit resonant states (such as Mercury's current 3/2 spin-orbit resonance) are only obtained by considering an additional torque due to a permanent equatorial deformation of the body.

Additionally to the three points mentioned above, estimations of the tidal energy dissipation and orbital evolution timescales using standard Darwin's theory lead to ambiguities due to the introduction of the so-called tidal quality factor Q . Essentially, the quality factor measures the quality of an oscillator in keeping free oscillations alive. The extension of the quality factor to characterize tidal dissipation as a forced oscillation leads to a dichotomy in its definition. Essentially, Q has a different definition for synchronous bodies when compared to free rotating bodies. For highly-eccentric orbits, this dichotomy represents a major problem, since the stationary rotation may deviate significantly from synchronism. As a consequence of such a deviation, multiple frequencies may cause tidal dissipation and it becomes difficult to choose the best value of Q to be employed.

Recently, a theory of equilibrium tides² for viscous bodies has been proposed by Ferraz-Mello (2013, 2015). In this Newtonian creep theory, an approximate solution of the Navier-Stokes equation is used to compute the instantaneous surface deformation of the extended body. The deformation is assumed to be proportional to the stress, and the proportionality constant (namely, the relaxation factor γ) depends on the mass, radius and uniform viscosity coefficient of the extended body. The Newtonian creep theory can reproduce both the characteristic spin-orbit resonant states for rocky bodies (such as Mercury-like planets) in non-circular orbits as well as the pseudo-synchronous rotation for gaseous bodies (such as mini-Neptunes and Jupiter-like planets). The only parameter that needs to be tuned to make the transition between these two regimes is the uniform viscosity coefficient of the body.

In a more recent work, a new version of the Newtonian creep theory was proposed (Folonier et al., 2018). This new version considers that the time-varying shape of the deformed body is an ellipsoid with unknown equatorial prolateness, polar oblateness and lag angle. As a result, three first-order ordinary differential equations must be integrated

² We refer to equilibrium tides as the tides caused by the time-varying shape of the extended body.

to solve for the shape of the body, while the rotation rate can be evolved by using the torque expression. The new version of the creep tide theory allows for a self-consistent treatment of the short-period rotation rate variations when solving for the shape of the body. The amplitude of oscillation of the rotation rate around the synchronous motion is much larger than the value predicted by employing the previous version of the theory.

The main objectives of this work are: 1) To revisit the development of the creep tide theory and make a comparison between the results obtained considering the old and new version of the theory, 2) to apply the creep tide theory to study the figure and spin evolution of a non-rigid homogeneous Mercury and 3) to apply the creep tide theory to study the orbital evolution of exoplanetary systems.

This thesis is organized as follows: In Chapter 2, we revisit the main concepts of the development of the Newtonian creep tide theory. We briefly discuss the approximations made in the Navier-Stokes equation to obtain the creep equation and the posterior spin-orbit and shape evolution equations. In Chapter 3, we present an application of the creep tide theory to study the spin and shape evolution of Mercury. Chapter 4 is dedicated to a presentation of the equations ruling the spin and orbit evolution of a two-body system in which both bodies can be considered as the tide-raising body. In Chapter 5, we consider an application of the creep tide theory to the orbital evolution of hot Jupiters. Our focus is the analysis of the relaxation factor values for these systems which are consistent with both the age estimations of the systems as well as their current orbital and rotational parameters. Chapter 6 regards an application of the creep tide theory to study the secular spin-orbit evolution of two exoplanetary systems containing potentially habitable exoplanets: the LHS-1140 b-c and K2-18 b-c systems. In Chapter 7, we present an implementation of the creep tide equations in the Posidonius N-body code (see Blanco-Cuaresma and Bolmont 2017a). In Chapter 8, we study how the transit-timing variations are affected by planetary tidal interactions. For that end, we use the Posidonius code with the creep tide theory implementation presented in the Chapter 7. Finally, Chapter 9 regards the conclusions of our studies.

The creep tide theory

2.1 Introduction

Several theories of tidal interactions are based on the adjustment of the equilibrium figure of a deformed body due to the gravitational potential of a disturbing companion. These theories are called *equilibrium tide* theories. The first theory to model equilibrium tides was proposed by Darwin in the XIX century (see Darwin 1880). Since such a pioneer work of Darwin, equilibrium tides have been treated following different approaches. In the hydrodynamical approach of the creep tide theory (see Ferraz-Mello 2012, 2013) and also other approaches such as the Maxwell model (see Correia and Rodríguez 2013; Correia et al. 2014), the starting point for the development of the theory is the *static equilibrium tide*. The static equilibrium tide is herein defined as the hydrostatic equilibrium figure of the tidally deformed body should its viscosity be zero (a.k.a the inviscid fluid limit). The effects of the *dynamic equilibrium tide* are afterwards introduced, in which case the response of the tidally deformed body considering the effects of a non-zero viscosity value are taken into account.

In the case of a homogeneous tidally deformed body, the developments of the creep tide theory have been treated in several previous works (Ferraz-Mello, 2012, 2013, 2015; Folonier et al., 2018). In the work of Ferraz-Mello (2012, 2013), the creep tide equations were developed considering that the static tide is given by a Jeans prolate spheroid (see Chandrasekhar 1969). Only the equatorial part of the tidal deformation was used to compute the equations for the tidal forces. The deformation of the body due to its rotation was not taken into account. In Ferraz-Mello (2015), the creep tide theory was applied to study the spin dynamics of planets and stars. In such work, the effect of tides on the

polar oblateness of the body as well as the effect of the rotation rate on the primary's shape were included in order to obtain the tidal forces and torques. In both the works of Ferraz-Mello (2012, 2013) and Ferraz-Mello (2015), the creep tide theory was developed using the first approximation that the rotation rate is constant. This assumption considers the rotation rate of the tidally deformed body as a constant to solve the equation for the shape of the tidally deformed body. Afterwards, the rotational evolution is computed by using the reaction of the torque acting on the point-mass companion. Such approach of the creep tide theory is sufficient to reproduce several interesting aspects of the spin-orbit dynamics of tidally-evolving bodies (see e.g., applications made in Ferraz-Mello 2015 and Gomes et al. 2019). However, the first approximation of the constant rotation rate is not self-consistent and may lead to an underestimation of the amplitude of oscillation of the rotation rate of stiff bodies around synchronous motions.

In the work of Folonier et al. (2018), the development of the creep tide theory for the homogeneous body case was revisited. The parametric approach presented in such work consistently considers the rotation rate evolution of the tidally deformed body from the first steps of the development of the theory. In such framework, the resulting equilibrium figure of the tidally deformed body due to the dynamic equilibrium tide is given by a triaxial ellipsoid, the shape, orientation and rotation of which are unknown parameters to be determined. The resulting figure of the tidally deformed body is obtained by solving four first-order ordinary differential equations. Additionally to the fact that the parametric approach presented in Folonier et al. (2018) allows a simpler development of the creep tide equations, it also naturally leads to an easier way to study the resulting equilibrium figure of the tidally deformed body. In what concerns the results obtained employing the parametric approach, Folonier et al. (2018) verified that considering the rotation rate as a variable from the first steps of the development of the theory leads to larger amplitudes of oscillation of the rotation rate around the synchronous attractor for bodies with large viscosity values. This is the case of bodies like super-Earths and planetary satellites (see Ferraz-Mello 2013, Table 1).

In this chapter, we will revisit the developments of the creep tide theory presented in Folonier et al. (2018) and present the equations necessary to study the spin-orbit and shape evolution of a given system.

2.2 The static equilibrium tide

The basis of the static tide is the following: We consider a homogeneous extended body (hereafter the primary) of mass m under the action of a tidal potential due to a second body (hereafter the companion) of mass M situated in its neighborhood, in the equatorial plane of the primary¹. The equilibrium figure of the primary under the action of (i) the tidal potential and (ii) the body's rotation may be approximated by a triaxial ellipsoid of surface equation $\rho = \rho(\hat{\theta}, \hat{\varphi}, t)$, where $\hat{\theta}$ and $\hat{\varphi}$ correspond to the co-latitude and longitude w.r.t the center of gravity of the primary. Additionally, ρ is the distance between the point on the surface of the ellipsoid and the center of gravity. The equation for the equilibrium surface of the body can be completely defined by two flattening coefficients: the equatorial prolateness ϵ_ρ and the polar oblateness ϵ_z . Their expressions are given by (see e.g., Chandrasekhar 1969; Folonier et al. 2015 and references therein)

$$\epsilon_\rho = \frac{15}{4} \left(\frac{M}{m} \right) \left(\frac{R_e}{r} \right)^3, \quad (2.1)$$

and

$$\epsilon_z = \frac{5\Omega^2 R_e^3}{Gm} + \frac{\epsilon_\rho}{2}. \quad (2.2)$$

In Eqs. (2.1) and (2.2), the symbols G , R_e and r correspond to the gravitational constant, the equatorial radius² of the primary and the instantaneous distance between the primary and the companion, respectively.

To obtain the expression for ρ in terms of the flattenings, let us first remind the equation for a generic triaxial ellipsoid. With respect to the principal axes, such equation is given by

$$\frac{X^2}{a^2} + \frac{Y^2}{b^2} + \frac{Z^2}{c^2} = 1, \quad (2.3)$$

with $a > b > c$.

To bring the system whose axes are the principal axes into the adopted system of reference (the latter being the system where the bulge instantaneously follows the movement

¹ We will assume that the companion is always in the equatorial plane of the primary. Such approximation is commonly referred to as the coplanar case.

² The equatorial radius of the primary is not constant, but varies with the value of ϵ_z , as it will be discussed in a forthcoming section.

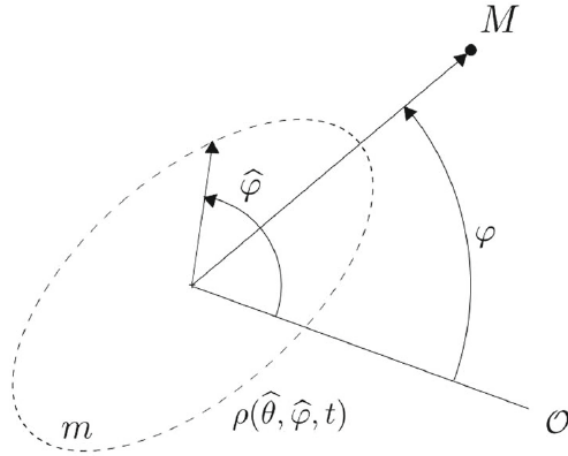


Figure 2.1: Equatorial section of the equilibrium figure corresponding to the static tide. Figure partially adapted from Folonier et al. (2018). The angles φ and $\hat{\varphi}$ are the longitudes w.r.t a fixed reference system, indicated by \mathcal{O} . As it can be seen, in the case of the static tide, the tidal bulge always points towards the point-mass companion.

of the companion in the equatorial plane), we need to perform a rotation around the Z axis. The coordinates of a point on the surface of the body, in such a reference system, are given by $(x, y, z) = (\rho \sin \hat{\theta} \cos \hat{\varphi}_F, \rho \sin \hat{\theta} \sin \hat{\varphi}_F, \rho \cos \hat{\theta})$. Considering that ϖ is the longitude of the pericenter and v is the true anomaly of the companion, the angle between the systems (X, Y, Z) and (x, y, z) is $\varpi + v$ (where ϖ is counted from the origin fixed in the rotating body). Thus, we have (see Ferraz-Mello 2015, Online Supplement for a more detailed calculation in terms of the rotation matrix)

$$\begin{aligned} X &= \rho \sin \hat{\theta} \cos(\hat{\varphi} - \omega - v), \\ Y &= \rho \sin \hat{\theta} \sin(\hat{\varphi} - \omega - v), \\ Z &= \rho \cos \hat{\theta}. \end{aligned} \quad (2.4)$$

Substituting Eqs. (2.4) in Eq. (2.3) and using the expressions linking the semi-major axes of the ellipsoid to the flattenings, given by $A = R_e \left(1 + \frac{1}{2}\epsilon_\rho\right)$, $B = R_e \left(1 - \frac{1}{2}\epsilon_\rho\right)$ and $C = R_e(1 - \epsilon_z)$, we obtain

$$\rho(\hat{\theta}, \hat{\varphi}, t) = R_e \left[1 + \frac{1}{2}\epsilon_\rho \sin^2 \hat{\theta} \cos(2\hat{\varphi} - 2\omega - 2v) - \epsilon_z \cos^2 \hat{\theta} \right]. \quad (2.5)$$

An illustration of the geometrical elements of the triaxial ellipsoid corresponding to Eq. (2.5) is given in Fig. 2.1.

At this point, it is worth mentioning that, to obtain the Eq. (2.5), we considered the Taylor expansion $(1 + \epsilon)^\alpha \approx 1 + \alpha\epsilon$, which is sufficient for $\epsilon \ll 1$ (ϵ corresponds to the flattenings).

2.3 The dynamic equilibrium tide

In the previous section, we derived the equation for the equilibrium surface of the primary considering that its viscosity is zero. In such case, the tidal bulge always points towards the companion and the flattenings of the primary are well known in terms of the physical and spatial parameters of the two-body system. If the primary's viscosity is non-zero (which corresponds to the dynamic equilibrium tide), we have to consider that the response of the primary to the movement of the companion is not instantaneous, but delayed.

There are several ways to include the delay of the primary's figure on the tidal theory. In the creep tide theory, the inclusion of the effect of the viscosity is made by employing the Navier-Stokes equation.

2.3.1 The Navier Stokes equation approach

In this section, we briefly present the main form of the Navier-Stokes equation for an incompressible fluid (i.e., a fluid with constant density d) with constant viscosity η . The equation reads (see e.g., Happel and Brenner 1983, Chapter 2 and references therein)

$$d \underbrace{\left(\frac{\partial \vec{v}}{\partial t} + \vec{v} \cdot \nabla \vec{v} \right)}_{\text{inertia terms}} = -\nabla p + \eta \nabla^2 \vec{v} + d \vec{F}, \quad (2.6)$$

where p is the hydrostatic pressure the fluid would be supporting if it were at rest at its local density, \vec{F} is the external force vector exerted on the fluid per unit mass and \vec{v} is the fluid velocity vector.

One of the most complicated problems when solving the Navier-Stokes in the general case of an arbitrary flow is that of turbulence. The Navier-Stokes equation as it is written in Eq. (2.6) is complicated to solve and, often, assumptions regarding the nature of the flow have to be made. In the case of the creep tide theory, we consider the so-called Stokes flow (also called the creeping motion). Such approximation consists on completely neglecting

the inertial terms in Eq. (2.6)³. Additionally, we omit the external force term since we are studying the immediate neighborhood of the equilibrium surface. In such case, the stress in that neighborhood is already considered in the pressure term. The aforementioned approximations allow us to write the creeping motion equation as

$$\nabla p = \eta \nabla^2 \vec{v}. \quad (2.7)$$

2.3.2 From the creeping motion to the creep equation

The Eq. (2.7) is written in terms of the fluid velocity vector. In the creep tide theory, we study only the radial displacement of the body w.r.t the equilibrium position. Additionally, we assume that the radial component of the velocity vector (namely, v_r) is independent of the azimuthal variables. In such specific case, we can rewrite the equation as

$$\frac{\partial^2 v_r}{\partial \zeta^2} + \frac{2}{\zeta} \frac{\partial v_r}{\partial \zeta} - \frac{2v_r}{\zeta^2} = \frac{\nabla p}{\eta}, \quad (2.8)$$

where ζ is the surface equation of the body considering the dynamic equilibrium tide.

The solution to the second-order differential equation shown in Eq. (2.8) can be written as

$$v_r(\zeta) = C_1 \zeta + \frac{C_2}{\zeta^2} + \frac{\nabla p}{4\eta} \zeta^2. \quad (2.9)$$

The constants C_1 and C_2 require two boundary conditions to be fully determined. The adopted conditions are:

- The velocity vanishes in the equilibrium position, namely $v_r(\zeta = \rho) = 0$;
- The approximation is linear, thus $v_r'' \equiv 0$.

Applying the two aforementioned conditions in Eq. (2.9) allows us to obtain that $C_1 = -\frac{\rho \nabla p}{6\eta}$ and $C_2 = -\frac{\rho^4 \nabla p}{12\eta}$. Linearizing the equation in the neighbourhood of $\zeta = \rho$ allows us to write

³ Such approximation is valid for Low-Reynolds-number flows, that is, when the role of the viscosity term is much larger than the role of inertial forces to describe the motion of the fluid. For more details, see discussions in Happel and Brenner (1983), Chapter 2, Section 2.6.

$$\dot{\zeta} = \frac{3gm}{8\pi R^2\eta}(\rho - \zeta), \quad (2.10)$$

where g is the surface gravity of the body and R its mean radius.

The term multiplying $(\rho - \zeta)$ in Eq.(2.10) is normally referred to as the relaxation factor γ . Thus, we have

$$\gamma = \frac{3gm}{8\pi R^2\eta}. \quad (2.11)$$

The creep equation can finally be written in a compact form as

$$\dot{\zeta} = \gamma(\rho - \zeta). \quad (2.12)$$

We can therefore define the creep equation as the equation allowing for the inclusion of the effect of viscosity on the creep tide theory, neglecting transversal displacements. It is the result of employing a linear approximation of the Navier-Stokes equation for a Low-Reynolds-number flow (i.e., in the case where viscous forces within the fluid are much stronger than inertial forces).

2.4 The parametric equations (Folonier et al., 2018)

The creep equation presented in Eq. (2.12) is a first-order ordinary differential equation (hereafter ODE) the solution of which allows us to determine the instantaneous equilibrium figure equation of the primary, considering the action of the dynamic equilibrium tide.

We will proceed as in Folonier et al. (2018) and write the instantaneous equilibrium figure of the primary ζ as the equation of a triaxial ellipsoid with unknown equatorial prolateness and polar oblateness coefficients (namely, \mathcal{E}_ρ and \mathcal{E}_z) and a deviation angle of the tidal bulge (namely, δ) with respect to the position of the companion. Fig.2.2 shows the geometrical elements corresponding to the dynamic equilibrium tide case.

The equation of the resulting triaxial ellipsoid can thus be written as

$$\zeta(\hat{\theta}, \hat{\varphi}, t) = R \left[1 + \frac{1}{2}\mathcal{E}_\rho \sin^2 \hat{\theta} \cos(2\hat{\varphi} - 2\varphi_B) + \mathcal{E}_z \left(\frac{1}{3} - \cos^2 \hat{\theta} \right) \right]. \quad (2.13)$$

At this point, it is worth mentioning an important difference between Eqs. (2.5) and (2.13). We employed the mean radius R instead of the equatorial radius R_e due to the

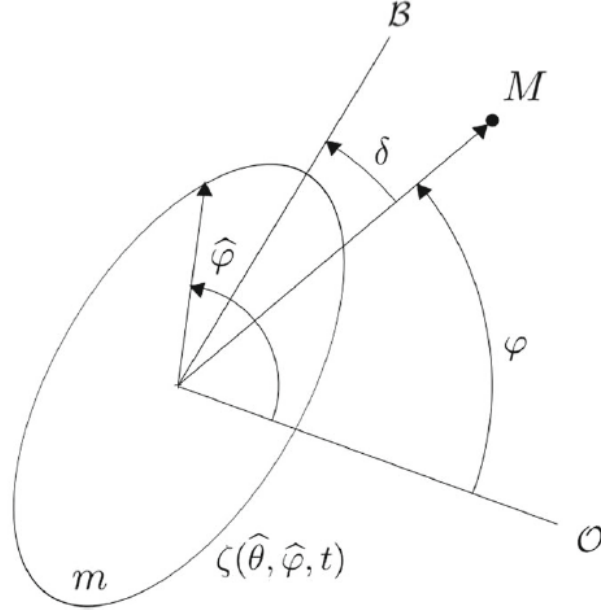


Figure 2.2: Equatorial section of the equilibrium figure corresponding to the dynamic tide. Figure partially adapted from Folonier et al. (2018). The angle δ corresponds to the deviation angle between the tidal bulge and the point-mass companion, and ζ corresponds to the equation of a point on the surface of the body considering the dynamic tide.

fact that, when the equatorial prolateness varies due to a variation in the distance of the primary to the companion, the polar flattening and R_e vary according to $R_e = R(1 + \epsilon_z/3)$ (see discussions in Folonier et al. 2018)⁴.

To obtain the evolution of the flattenings of the resulting ellipsoid as well as the deviation angle, we can substitute Eq. (2.13) in Eq. (2.12). Decomposing the resulting equation and matching the terms with the same trigonometric arguments allows us to write the creep equation as three first-order ODEs, which are the so-called parametric equations (Folonier et al., 2018). The calculations are straightforward and the resulting ODEs are given by

$$\dot{\delta} = \Omega - \dot{\varphi} - \frac{\gamma\epsilon_\rho}{2\mathcal{E}_\rho} \sin 2\delta, \quad (2.14)$$

$$\dot{\mathcal{E}}_\rho = \gamma(\epsilon_\rho \cos 2\delta - \mathcal{E}_\rho), \quad (2.15)$$

$$\dot{\mathcal{E}}_z = \gamma(\epsilon_z - \mathcal{E}_z). \quad (2.16)$$

While the parametric equations allow us to study the time evolution of the primary's

⁴ To obtain the expression for ρ in terms of the mean radius, it suffices to change the sign of the last term on the right hand side of Eq. (2.5) and replace the coefficient multiplying ϵ_z from $\cos^2 \hat{\theta}$ to $\frac{1}{3} - \cos^2 \hat{\theta}$.

shape and orientation, they are not complete in the sense that the time dependence of the rotation rate is unknown. To consider a complete and self-consistent treatment of the spin-orbit and shape evolution, we need the equations for the forces (which allow us to study the orbital evolution of the system) and the torques (which allow us to study the rotational evolution of the primary). Such calculations will be carried out in the next section.

2.5 The tidal forces and torques

To obtain the equation for the tidal forces, we first write the equation for the potential caused by the triaxial ellipsoid in terms of the flattenings and the tidal bulge angle. The expression for the disturbing potential (namely, δU) reads (see Folonier et al. 2018; Ferraz-Mello et al. 2020)

$$\delta U = -\frac{GC}{2r^3}\mathcal{E}_\rho(3\cos^2\Psi_B - 1) - \frac{GC}{2r^3}\left(\mathcal{E}_z - \frac{1}{2}\mathcal{E}_\rho\right), \quad (2.17)$$

where Ψ_B is the angle between the direction of the point where the potential is taken and the direction of the bulge vertex.

The calculation of the gradient of the disturbing potential allows us to write the force expression acting on the companion through $\vec{F} = -M\nabla\delta U$. Since we are dealing with the case where the companion lies always on the equatorial plane of the primary, we have $\hat{\theta} = \pi/2$. In such case, the force components can be written as

$$F_1 = -\frac{3GMC\mathcal{E}_\rho}{2r^4}(3\cos^2\delta - 1) - \frac{3GMC}{2r^4}\left(\mathcal{E}_z - \frac{1}{2}\mathcal{E}_\rho\right), \quad (2.18)$$

$$F_2 = 0, \quad (2.19)$$

$$F_3 = \frac{3GMC\mathcal{E}_\rho}{2r^4}\sin 2\delta. \quad (2.20)$$

The group of Eqs. (2.18)-(2.20) can be used to study the orbital evolution of the system. They also allow us to compute the torque expression. The calculation is straightforward and we obtain

$$\mathbf{M} = rF_3\hat{\mathbf{z}} = \frac{3GMC\mathcal{E}_\rho}{2r^3}\sin 2\delta\hat{\mathbf{z}}. \quad (2.21)$$

The reaction of the torque acting on the companion is the torque dictating the rotational evolution of the primary. The resulting equation for the rotational evolution of the primary is, thus

$$\dot{\Omega} = -\frac{3GM\mathcal{E}_\rho}{2r^3} \sin 2\delta. \quad (2.22)$$

It is worth mentioning that we neglected the contribution of the variation of the moment of inertia (namely, the term $\dot{C}\Omega$) of the primary to obtain Eq. (2.22). Such contribution is relatively small and can be neglected in most of the applications to the planetary systems discovered so far (see also discussions in Folonier et al. 2018).

The equations presented in this section were computed with no assumptions on the relative masses of the bodies. Thus, the combined action of the tides of both bodies can be computed by inverting the roles of the primary and the companion (see e.g., discussions in Ferraz-Mello et al. 2008; Ferraz-Mello 2015).

Rotation and figure evolution in the creep tide theory: a new approach and application to Mercury

The following article addresses an implementation of the creep tide theory (Folonier et al., 2018) to study the rotation and figure evolution of a homogeneous non-rigid Mercury. The approach allows for arbitrary eccentricity values and a straightforward formalism to study the rotation, orientation of the tidal bulge and shape of the planet. We focus our analysis on the study of the 3/2 and 2/1 spin-orbit resonances, since Mercury is currently in the 3/2 spin-orbit resonance. We also study of the range of possible values of the relaxation factor of Mercury which could lead to its current spin configuration (i.e., a 3/2 spin-orbit resonant state) considering that its eccentricity was never below $e = 0.1$ (Laskar, 1996). Finally, we discuss some consequences of our results regarding the estimation of Mercury's uniform viscosity coefficient to its shape evolution. We compare the predictions of the creep tide theory with recent data coming from the MESSENGER observations (Perry et al., 2015).

The results of the article allow us to conclude that, for any non-synchronous spin-orbit resonant states, the tidal lag angle for a non-rigid homogeneous Mercury (namely, δ) always circulates with a period which depends on the given spin-orbit resonance. Moreover, the angle $\varphi_B = \varphi + \delta$ (where φ is the true anomaly of Mercury) circulates with the same period of the rotation rate, for low values of the relaxation factor (γ). For high values of γ , δ oscillates around 0, where the amplitude of the oscillation depends on the value of the relaxation factor.

In what concerns the analysis of Mercury's relaxation factor value leading to its current spin-orbit configuration, we have concluded that the relaxation factor is such that $4.8 \times$

$10^{-9} \text{ s}^{-1} \leq \gamma \leq 4.8 \times 10^{-8} \text{ s}^{-1}$. This range of values of the relaxation factor corresponds to a range of values of the uniform viscosity coefficient of $5.1 \times 10^{17} \text{ Pa s} \leq \eta \leq 5.0 \times 10^{18} \text{ Pa s}$. The range of values for γ (and, consequently, for η) were determined by considering three hypotheses: (i) Mercury's eccentricity was never below 0.1 (Laskar, 1996), (ii) for $e = 0.1$, Mercury cannot remain trapped in the 2/1 spin-orbit resonance and (iii) for $e = 0.1$ Mercury remains trapped in the 3/2 spin-orbit resonance (otherwise the planet would escape to the synchronous rotation rate configuration).

Lastly, the predictions for the shape and orientation evolution of Mercury in the frame of the creep tide theory allowed us to conclude that the equatorial prolateness (\mathcal{E}_ρ) and polar oblateness (\mathcal{E}_z) of Mercury are of the order $\mathcal{E}_\rho = 1.1 \times 10^{-6}$ and $\mathcal{E}_z = 2.2 \times 10^{-6}$. These values are in agreement with estimations performed using the Darwin-Kaula expansion method presented in Matsuyama and Nimmo (2009). According to MESSENGER data, however, the observations indicate that the actual values of Mercury's flattenings are of the order $\mathcal{E}_\rho = 5.5 \times 10^{-4}$ and $\mathcal{E}_z = 9.6 \times 10^{-4}$. These values are approximately two orders of magnitude larger than the values predicted by the creep tide theory or any other equilibrium tide theory. Thus, the results suggest the existence of a fossil component which may be responsible for Mercury's current shape.



Rotation and figure evolution in the creep tide theory: a new approach and application to Mercury

G. O. Gomes¹ · H. A. Folonier¹ · S. Ferraz-Mello¹

Received: 14 June 2019 / Revised: 24 October 2019 / Accepted: 1 November 2019
© Springer Nature B.V. 2019

Abstract

This paper deals with the rotation and figure evolution of a planet near the 3/2 spin–orbit resonance and the exploration of a new formulation of the creep tide theory (Folonier et al. in *Celest Mech Dyn Astron* 130:78, 2018). This new formulation is composed by a system of differential equations for the figure and the rotation of the body simultaneously (which is the same system of equations used in Folonier et al. 2018), different from the original one (Ferraz-Mello in *Celest Mech Dyn Astron* 116:109–140, 2013; *Celest Mech Dyn Astron* 122:359–389, 2015a. [arXiv: 1505.05384](https://arxiv.org/abs/1505.05384)) in which rotation and figure were considered separately. The time evolution of the figure of the body is studied for both the 3/2 and 2/1 spin–orbit resonances. Moreover, we provide a method to determine the relaxation factor γ of non-rigid homogeneous bodies whose endpoint of rotational evolution from tidal interactions is the 3/2 spin–orbit resonance, provided that (i) an initially faster rotation is assumed and (ii) no permanent components of the flattenings of the body existed at the time of the capture in the 3/2 spin–orbit resonance. The method is applied to Mercury, since it is currently trapped in a 3/2 spin–orbit resonance with its orbital motion and we obtain $4.8 \times 10^{-8} \text{ s}^{-1} \leq \gamma \leq 4.8 \times 10^{-9} \text{ s}^{-1}$. The equatorial prolateness and polar oblateness coefficients obtained for Mercury’s figure with such range of values of γ are the same as the ones given by the Darwin–Kaula model (Matsuyama and Nimmo in *J Geophys Res* 114, E01010, 2009). However, comparing the values of the flattenings obtained for such range of γ with those obtained from MESSENGER’s measurements (Perry et al. in *Geophys. Res. Lett.* 42, 6951–6958, 2015), we see that the current values for Mercury’s equatorial prolateness and polar oblateness are 2–3 orders of magnitude larger than the values given by the tidal theories.

Keywords Planetary tide · Mercury · Flattenings · Spin-orbit

G. O. Gomes
gabrielogomes@usp.br

H. A. Folonier
hugofolonier@gmail.com

S. Ferraz-Mello
sylvio@iag.usp.br

¹ Instituto de Astronomia Geofísica e Ciências Atmosféricas, Universidade de São Paulo, São Paulo, Brazil

1 Introduction

It is known that Mercury's current rotation is in a $3/2$ spin–orbit resonance with its orbital motion. This means that it rotates on its axis three times for every two revolutions made around the Sun. The scenario used to explain Mercury's current rotational configuration by means of tidal interactions usually involves the assumption that Mercury was initially in a fast rotating state and then evolved under the action of tidal interactions which slowed down the rotation of Mercury until it reached the $3/2$ spin–orbit resonance (see e.g. Noyelles et al. 2014). The tidal models used to evaluate the torque that slowed down the rotation of Mercury are usually based on classical tidal theories. In these works, the existence of an additional torque arising from a permanent equatorial asymmetry is generally assumed to capture Mercury's rotation in the $3/2$ spin–orbit resonance (see e.g. Bartuccelli et al. 2017).

Recently, Ferraz-Mello (2012, 2013, 2014, 2015a) proposed a theory of tidal interactions based on an approximate solution of the Navier–Stokes equation for a flux that has a low Reynolds number. Considering this theory, the equatorial asymmetry ensues as a consequence of tidal interactions and the capture in spin–orbit resonances can be explained without the assumption of an extra torque due to a permanent equatorial asymmetry of the body. This result was also reported by Makarov and Efroimsky (2013) and confirmed by Correia et al. (2014) with a modeling based on a Maxwell viscoelastic rheology. In the framework of the creep tide theory, tidal interactions alone may be responsible for the evolution of the spin of a non-rigid body and whether or not the body is trapped in a spin–orbit resonance depends on its eccentricity and relaxation factor γ .

In this work, we study the rotational evolution of a homogeneous non-rigid Mercury in the frame of the creep tide theory of Ferraz-Mello (2012, 2013) using the decomposition of the creep equation in three separated equations, as proposed in Folonier et al. (2018). These new equations are virtually equivalent to the equations used in studies employing the Maxwell viscoelastic model (Correia et al. 2014), and they allow for a self-consistent version of the creep tide theory to be constructed. Their simplicity also allows us to use some analytical approximations. We confirm that the capture in spin–orbit resonances depends on γ , the eccentricity e and the initial value of the rotation rate. The evolution of the equilibrium ellipsoid is discussed for the $3/2$ and $2/1$ spin–orbit resonances. (The synchronous case was already studied in Folonier et al. (2018)). We calculate the range of values of the relaxation factor of a non-rigid homogeneous Mercury for which it would currently be in the $3/2$ spin–orbit resonance, provided that it was initially in a fast rotating prograde configuration and that its eccentricity minimum value was never below $e = 0.1$. We do not make more specific assumptions since there are no observational clues to support them.

The report starts with a brief recapitulation of the new formulation of the creep tide theory (Folonier et al. 2018). The differential equations ruling the shape and spin–orbit dynamics in this framework are deduced in Sect. 2. In Sect. 3, we present the solution of such equations corresponding to the approximation where $\dot{\Omega} \approx 0$. In Sect. 4, we study the full model, characterized by the numerical integration of the equations, and use Mercury's physical and orbital parameters to study the rotational dynamics and evolution of its figure. Section 5 is dedicated to an application of the equations to the determination of the constraints for the relaxation factor of a body for which the rotational configuration is the $3/2$ spin–orbit resonance. We apply our analysis to the case of Mercury's rotation, since this is the only body whose rotation is known to be trapped in a $3/2$ spin–orbit resonance. In Sect. 6, we discuss Mercury's current figure evolution in the frame of the creep tide theory and compare

our results to the ones obtained from the MESSENGER mission (Perry et al. 2015). The conclusions are given in Sect. 7.

2 Creep tide theory: Folonier equations

Let us consider that an extended body m of mass m (primary) experiences the gravitational potential from a point mass body M of mass M (companion). The combined action of the centrifugal potential caused by the primary’s rotation and the gravitational potential generated by the companion’s gravitational attraction causes a deformation on the primary. The equilibrium surface is given by a triaxial ellipsoid (to first order in the flattenings, see Chandrasekhar 1969 and Folonier et al. 2015). In the case of an inviscid fluid (also known as static case), the equilibrium figure of the triaxial ellipsoid is given by

$$\rho(\hat{\theta}, \hat{\varphi}, t) = R \left[1 + \frac{1}{2} \epsilon_\rho \sin^2 \hat{\theta} \cos(2\hat{\varphi} - 2\varphi) + \epsilon_z \left(\frac{1}{3} - \cos^2 \hat{\theta} \right) \right], \tag{1}$$

with $\hat{\theta}$ and $\hat{\varphi}$ being the colatitude and longitude of a generic point on the surface of the equilibrium ellipsoid, respectively. R and φ are the mean radius of the primary and the true anomaly of the companion. The coefficients ϵ_ρ and ϵ_z are the equatorial prolateness and polar oblateness of the resulting ellipsoid, respectively, which depend on the physical and orbital parameters of the system through

$$\epsilon_\rho = \frac{15M}{4m} \left(\frac{R}{a} \right)^3 \left(\frac{a}{r} \right)^3 \equiv \bar{\epsilon}_\rho \left(\frac{a}{r} \right)^3, \tag{2}$$

$$\epsilon_z = \frac{\epsilon_\rho}{2} + \frac{5}{4} \frac{\Omega^2 R^3}{Gm} \tag{3}$$

with G being the gravitational constant, Ω the rotation rate. In the general case, where we have a fluid with a given viscosity η , the equilibrium figure of the resulting ellipsoid is given by $\zeta(\hat{\theta}, \hat{\varphi}, t)$, which is the solution of the creep equation

$$\dot{\zeta} = \gamma(\rho - \zeta), \tag{4}$$

where the relaxation factor γ is inversely proportional to the uniform viscosity coefficient η (see Ferraz-Mello 2013, Eq. (3)). Explicitly, we have

$$\gamma = \frac{wR}{2\eta}, \tag{5}$$

where w is the specific weight on the surface of the body.

Folonier et al. (2018) assumed that the solution of the creep equation may be approximated by a generic triaxial ellipsoid with unknown equatorial prolateness, polar oblateness and deviation angle w.r.t the companion (namely, \mathcal{E}_ρ , \mathcal{E}_z and δ), whose equation is

$$\zeta(\hat{\theta}, \hat{\varphi}, t) = R \left[1 + \frac{1}{2} \mathcal{E}_\rho \sin^2 \hat{\theta} \cos(2\hat{\varphi} - 2\varphi - 2\delta) + \mathcal{E}_z \left(\frac{1}{3} - \cos^2 \hat{\theta} \right) \right]. \tag{6}$$

Substituting Eq. (6) into Eq. (4) and comparing the terms with the same trigonometrical arguments of $\hat{\varphi}$ and $\hat{\theta}$, we obtain three differential equations to be solved, namely

$$\dot{\delta} = \Omega - \dot{\varphi} - \frac{\gamma \mathcal{E}_\rho}{2\mathcal{E}_\rho} \sin 2\delta, \tag{7}$$

$$\dot{\mathcal{E}}_\rho = \gamma(\epsilon_\rho \cos 2\delta - \mathcal{E}_\rho), \quad (8)$$

$$\dot{\mathcal{E}}_z = \gamma(\epsilon_z - \mathcal{E}_z). \quad (9)$$

From the expression for the torque at the companion generated by the primary, we can calculate its reaction ruling the rotational evolution of the primary. The calculations are straightforward (see Folonier et al. 2018). The result is

$$\dot{\Omega} = -\frac{3GM}{2r^3} \mathcal{E}_\rho \sin 2\delta. \quad (10)$$

Equations (7)–(10) rule the evolution of the orientation, shape and rotation of the body. These equations can be integrated numerically to the desired precision.

2.1 Change of variables

The system of equations presented in the previous section can be simplified if we consider a transformation given by

$$x = E_\rho \cos 2\delta, \quad (11)$$

$$y = E_\rho \sin 2\delta, \quad (12)$$

where

$$E_\rho = \frac{\mathcal{E}_\rho}{\epsilon_\rho}. \quad (13)$$

The differential equations involving x and y can be easily obtained directly from the above equations. The calculations are straightforward, and the resulting differential equations are

$$\dot{x} = \gamma \left(\frac{a}{r} \right)^3 - \gamma x - y(2\Omega - 2\dot{\varphi}), \quad (14)$$

$$\dot{y} = -\gamma y + x(2\Omega - 2\dot{\varphi}), \quad (15)$$

$$\dot{\Omega} = -\frac{3GM}{2r^3} \bar{\epsilon}_\rho y. \quad (16)$$

It is worth mentioning that the above system of differential equations cannot be solved analytically in the general eccentric case. The terms carrying $\dot{\varphi}$ and $(a/r)^3$ are solutions of the Keplerian motion. Another interesting characteristic of the system of differential equations is that the equation for \mathcal{E}_z [see Eq. (9)] is decoupled from the other three differential equations. Thus, it can be treated separately.

3 Simplified approach with constant rotation

In this section, we discuss a simplification of the equations of the new formulation of the creep tide theory. In application to Mercury, we see in Fig. 1 that the variation of the rotation rate is small for short time intervals for both regimes of the relaxation factor γ ($\gamma \gg n$ and $\gamma \ll n$, where n is the orbital mean motion). Thus, for short time intervals, we can approximate the rotation rate to a constant value. The rotation is rapidly driven to a quasi-steady state. Figure 2 shows the solution of the differential equations for $\gamma = 4 \times 10^{-8} \text{ s}^{-1}$. The figure shows both the transient and the quasi-steady state.

In order to understand the dynamics associated with the quasi-steady state reached after the transient, we consider initially the simplification in our equations that result when we assume a constant rotation.

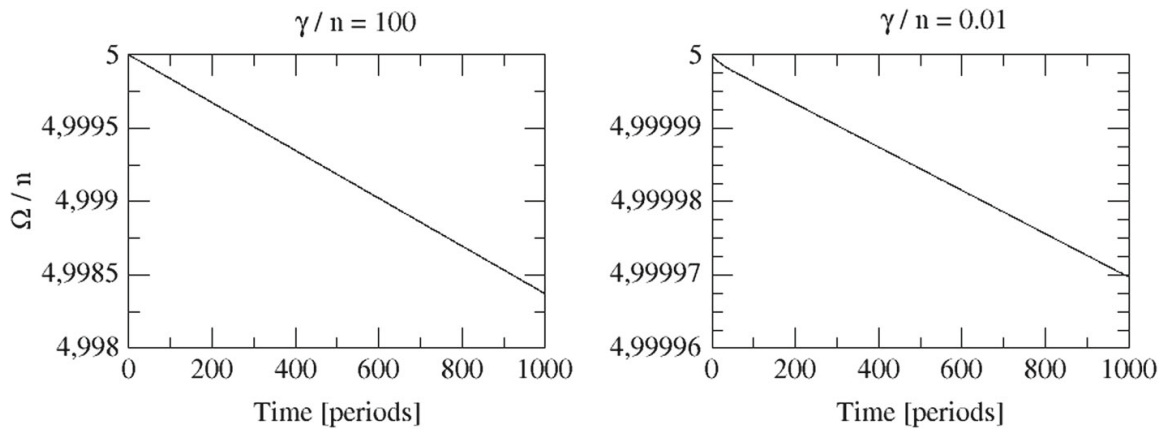
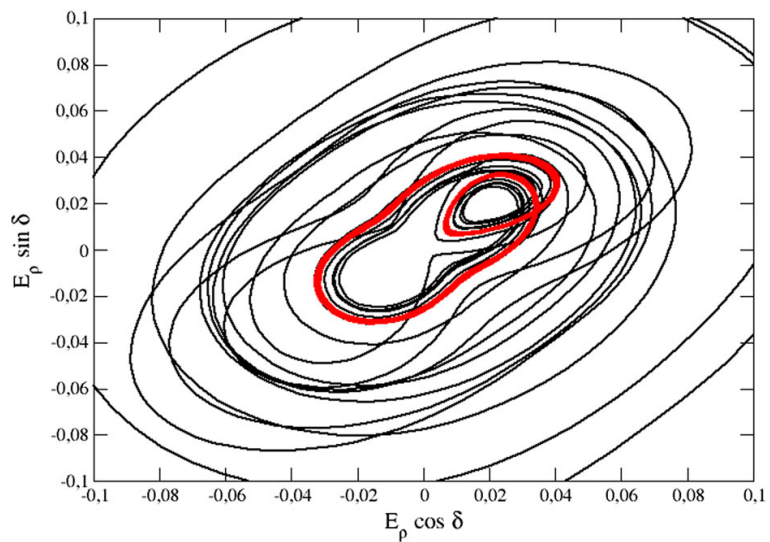


Fig. 1 Numerical integration of Eqs. (7)–(10) for a homogeneous non-rigid Mercury considering two different values of γ/n as indicated in the figure. The eccentricity is $e = 0.2$. In both regimes ($\gamma \gg n$ on the left and $\gamma \ll n$ on the right), we see that the value of the rotation rate changes slowly, in a timescale much larger than the orbital period of Mercury of 88 days

Fig. 2 Plot of the solutions considering $e = 0.15$, $\Omega/n = 2.45$ and $\gamma/n = 4.83 \times 10^{-2}$. After the transient (black curve in the plot), the solution is trapped in a quasi-stationary closed curve (red curve in the plot)



To solve the system of differential equations for x and y , we define the complex variable

$$Z = x + iy, \tag{17}$$

and rewrite the equations for \dot{x} and \dot{y} in the simple form

$$\dot{Z} + [\gamma - i(2\Omega - 2\dot{\varphi})]Z = \gamma \left(\frac{a}{r}\right)^3. \tag{18}$$

The general solution of Eq. (18) is (see Arfken 2005)

$$Z(t) = \frac{\gamma \int e^{\int f(t)dt} \left(\frac{a}{r}\right)^3 dt + c}{e^{\int f(t)dt}}, \tag{19}$$

where

$$f(t) = \gamma - i(2\Omega - 2\dot{\varphi}).$$

The integration is straightforward and we use the expansions of the Keplerian motion in Fourier series (see Ferraz-Mello 2015a. Online Supplement):

$$\left(\frac{a}{r}\right)^3 e^{2i\varphi} = \sum_{k \in \mathbb{Z}} E_{2,2-k} e^{ik\ell}, \quad (20)$$

where $E_{2,j}$ are Cayley coefficients and ℓ is the mean anomaly of the companion.

The term carrying the constant c in Eq. (19) is transient, and it can be neglected. It carries an exponential term and decreases with time tending to zero. The term of $Z(t)$ related to the quasi-steady solution is

$$Z(t) = \gamma \left[\sum_{k \in \mathbb{Z}} E_{2,2-k} \int e^{\gamma t + i(k\ell - 2\widehat{\varphi})} dt \right] e^{-\gamma t + 2i(\widehat{\varphi} - \varphi)}. \quad (21)$$

The calculation is trivial and the resulting expression for $Z(t)$ reads

$$Z(t) = \gamma \sum_{k \in \mathbb{Z}} \frac{E_{2,2-k}}{\gamma + i(kn - 2\Omega)} e^{i(k\ell - 2\varphi)}. \quad (22)$$

To obtain x and y , we just need to use the identity $Z = x + iy$ and identify the real and imaginary parts of $Z(t)$. The resulting expressions are

$$x(t) = \sum_{k \in \mathbb{Z}} \frac{\gamma E_{2,2-k}}{\gamma^2 + (2\Omega - kn)^2} [\gamma \cos(k\ell - 2\varphi) - (2\Omega - kn) \sin(k\ell - 2\varphi)], \quad (23)$$

$$y(t) = \sum_{k \in \mathbb{Z}} \frac{\gamma E_{2,2-k}}{\gamma^2 + (2\Omega - kn)^2} [\gamma \sin(k\ell - 2\varphi) + (2\Omega - kn) \cos(k\ell - 2\varphi)]. \quad (24)$$

From the expressions for x and y thus obtained, we can calculate the corresponding variation in the rotation rate. From Eqs. (16) to (24), we obtain for $\dot{\Omega}$ that

$$\dot{\Omega} = -\frac{3GM\bar{\epsilon}_\rho}{2a^3} \sum_{k \in \mathbb{Z}} \frac{\gamma E_{2,k}}{\sqrt{\gamma^2 + (v + kn)^2}} \left\{ \sum_{j \in \mathbb{Z}} E_{2,k+j} \sin \left[j\ell + \arctan \left(\frac{v + kn}{\gamma} \right) \right] \right\}, \quad (25)$$

where $v = 2\Omega - 2n$ is the semidiurnal frequency.

Equation (25) is exactly the same expression presented in Eq. (36) of Ferraz-Mello (2015a). Thus, we see that the old creep tide theory (Ferraz-Mello 2013, 2015a) and the new version of the theory reproduce the same results if we initially consider $\Omega \approx \text{const.}$ and then obtain $\Omega(t)$ from the torque expression.¹ However, we emphasize that the above construction of the solution for constant Ω is not self-consistent, since we firstly assumed a constant Ω to obtain x and y and then obtained $\dot{\Omega}$ from the torque expression. As discussed in Folonier et al. (2018), the oscillations in Ω are significant when studying the energy dissipation in synchronous stiff bodies (see also Efroimsky 2018a, b).

¹ It is worth noting that this equation is also the same equation as Eq. (39) of Correia et al. (2014) notwithstanding the differences of the Maxwell viscoelastic model adopted by those authors and the creep tide model. This coincidence confirms the fact that the addition of an elastic term to the creep does not change the torque acting on the system, as discussed in Ferraz-Mello (2012, 2013).

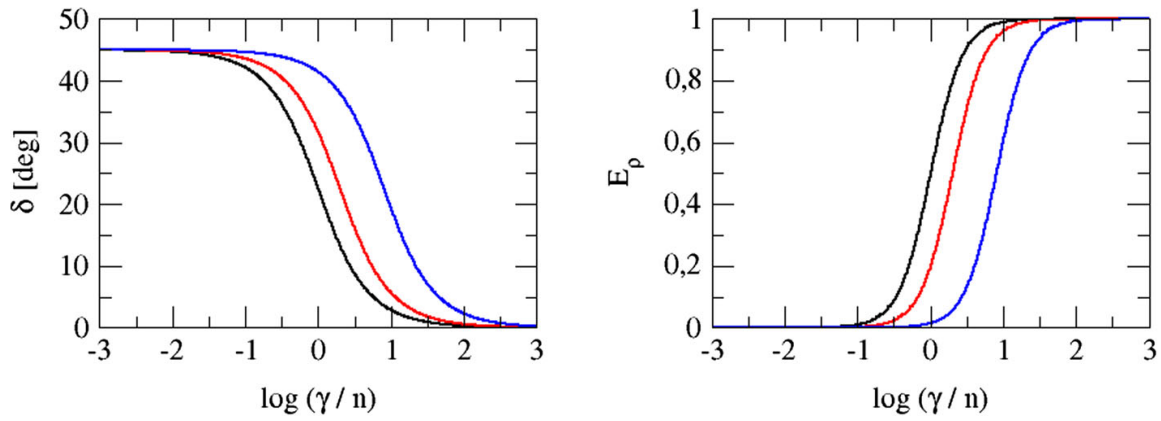


Fig. 3 Deviation angle δ (on the left) and normalized equatorial prolateness E_ρ (on the right) in the circular case for three different values of Ω/n . We have $\Omega/n = 1.5, 2$ and 5 on the black, red and blue curves, respectively

3.1 Circular case

For the sake of showing in a simpler way some of the consequences of the current simplified approach, we turn our attention to the circular case. In this case, we have $E_{2,0} = 1$ and all the other Cayley coefficients equal 0. Then, the solutions for x and y become

$$x(t) = \frac{\gamma^2}{\gamma^2 + v^2}, \tag{26}$$

$$y(t) = \frac{\gamma v}{\gamma^2 + v^2}. \tag{27}$$

For δ and E_ρ , we obtain

$$\delta = \frac{1}{2} \arctan\left(\frac{v}{\gamma}\right), E_\rho = \frac{\gamma}{\sqrt{\gamma^2 + v^2}} = \cos 2\delta. \tag{28}$$

Figure 3 shows the functions δ and E_ρ for the circular case considering different values of Ω/n . We see that for $\gamma \ll n$, the deviation angle δ is 45° and E_ρ is small, of the order 10^{-4} . As γ increases, the value of δ decreases until it reaches 0° . while E_ρ increases until $E_\rho = 1$.

Figure 4 shows a comparison of the circular case and the eccentric case. In the circular case, the trajectory in the diagram is given by a single point in each panel. The eccentricity introduces forced oscillations around the circular case whose amplitude increases when the eccentricity increases.

3.2 Spin-orbit resonances

It was already shown by Makarov and Efroimsky (2013) that, for solid planets and moons (which, in the frame of the creep tide theory, are characterized by a small value of γ , typically $\gamma \ll n$), there may be several stationary values of the rotation rate other than the synchronous state. These stationary non-synchronous configurations of the rotation are the spin-orbit resonances.

The simplified approach of the new version of the creep tide theory explains how spin-orbit resonances ensue in a given system. For this sake, we calculate the average of $\dot{\Omega}$ (see Eq. 25) which gives

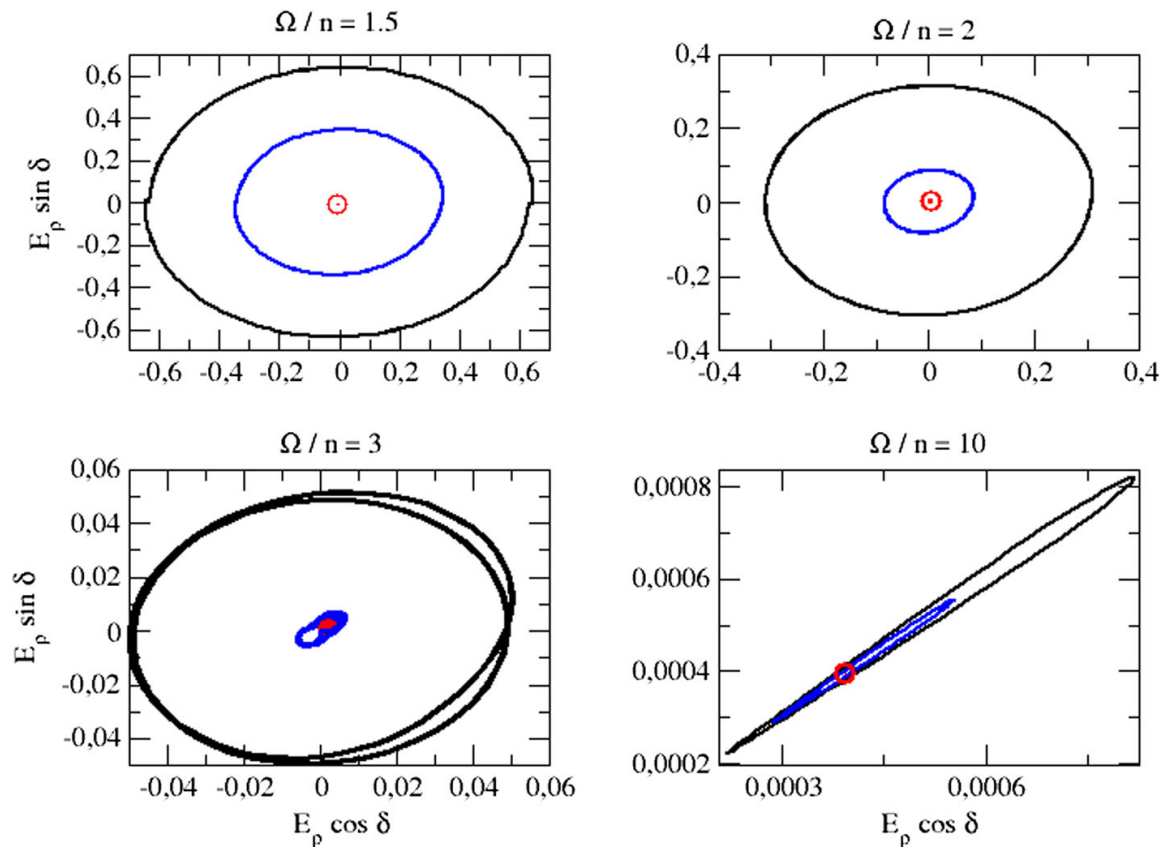


Fig. 4 Solution of the simplified equations for $\gamma/n = 0.01$ in the circular case (corresponding to the center of the red circle) and two eccentric cases, with $e = 0.1$ (blue) and $e = 0.2$ (black)

$$\langle \dot{\Omega} \rangle = -\frac{3GM\bar{\epsilon}_\rho}{2a^3} \sum_{k \in \mathbb{Z}} \frac{\gamma(\nu + kn)E_{2,k}^2}{\gamma^2 + (\nu + kn)^2}. \tag{29}$$

When the rotation is trapped in a spin-orbit resonance, we have $\langle \dot{\Omega} \rangle = 0$. However, in general, the sum of Eq. (29) is not exactly 0. The equilibrium does not occur at the exact commensurability, but in a neighborhood of it. For a given commensurability, there is a term in the sum of the terms that corresponds to $\nu + kn \approx 0$. We call the index k related to such term as k' . Then, the condition for a spin-orbit resonance to be effective becomes

$$\frac{\gamma(\nu + k'n)E_{2,k'}^2}{\gamma^2 + (\nu + k'n)^2} = - \sum_{k \in \mathbb{Z}, k \neq k'} \frac{\gamma(\nu + kn)E_{2,k}^2}{\gamma^2 + (\nu + kn)^2}. \tag{30}$$

In the right-hand side of the above equation, we can consider the exact commensurability for all the terms in the sum, that is $\nu = -k'n$. Then, taking into account that the term with $k = k'$ equals 0, we can write

$$\frac{\gamma(\nu + k'n)E_{2,k'}^2}{\gamma^2 + (\nu + k'n)^2} = - \sum_{k \in \mathbb{Z}} \frac{\gamma(-k'n + kn)E_{2,k}^2}{\gamma^2 + (-k'n + kn)^2}. \tag{31}$$

The coefficient of $E_{2,k'}^2$ is of the form $(x + 1/x)^{-1}$ and, thus, its maximum value (in absolute value) is attained for $x = \pm 1$ or, in this case, when $\gamma = |\nu + k'n|$, for which the coefficient equals $1/2$. Then, the left-hand side term is never larger than $E_{2,k'}^2/2$. As a consequence, the above equation has a solution only if

$$\frac{E_{2,k'}^2}{2} \geq \left| \sum_{k \in \mathbb{Z}} \frac{\gamma n(k - k') E_{2,k}^2}{\gamma^2 + (k - k')^2 n^2} \right|. \tag{32}$$

For each spin-orbit resonance associated to a given $k' \approx -\nu/n$, the equality on the above equation gives the relation between the minimum eccentricity and the relaxation factor for which the possibility of capture in the given spin-orbit resonance exists. (That is, the rotation may be trapped in the resonance as Ω/n approaches the value corresponding to the resonance.) It is important to mention that Eq. (32) is the same as the one presented in Correia et al. (2014).

One application of Eq. (32) is that we can obtain an analytic relation between the minimum eccentricity for which a given spin-orbit resonance can exist and the relaxation factor γ . For the 3/2 spin-orbit resonance (corresponding to $k' = -1$), we can expand the Cayley coefficients $E_{2,k}^2$ to order e^4 and obtain a quartic equation to be solved in e . Since there are only even powers of e (we have $E_{2,k}^2$ only), it can be reduced to a quadratic equation. The only real root gives us the relation between e_{min} and γ . The calculations are straightforward and the relation for the 3/2 spin-orbit resonance is

$$e_{min}^{(3/2)} = \frac{2\sqrt{2}}{7} \left(\frac{\gamma}{n}\right)^{1/2} - \frac{27\sqrt{2}}{2401} \left(\frac{\gamma}{n}\right)^{3/2} + \mathcal{O}(\gamma^{5/2}). \tag{33}$$

In a similar way, for the 2/1 spin-orbit resonance, we obtain

$$e_{min}^{(2/1)} = \sqrt{\frac{2}{17}} \left(\frac{\gamma}{n}\right)^{1/4} + \frac{59}{51\sqrt{34}} \left(\frac{\gamma}{n}\right)^{3/4} + \mathcal{O}(\gamma^{5/4}). \tag{34}$$

It is worth mentioning that the lower the value of k' (corresponding to higher-order spin-orbit resonances), the higher is the order of expansion needed for the Cayley coefficients. For the 7/2 spin-orbit resonance, for instance, we would need at least an expansion of order e^{10} .

4 Complete model: the neighborhood of the resonances

In this section, we study the evolution of a non-rigid homogeneous body for initial values of the rotation rate close to two spin-orbit resonances: the 3/2 and 2/1 spin-orbit resonances.

4.1 The 3/2 spin-orbit resonance

The 3/2 spin-orbit resonance is the last one encountered by a tidally evolving body before it reaches synchronization. Fig. 5 shows the evolution of the shape, orientation and rotation of a non-rigid homogeneous Mercury when the rotation already evolved and reached the 3/2 spin-orbit resonant configuration.

The numerical results presented in Fig. 5 show that once the rotation is trapped in the 3/2 spin-orbit resonance, the equatorial prolateness and polar oblateness suffer only small oscillations around a mean value. The same behavior holds for the rotation rate Ω/n . However, for the orientation of the equatorial tidal bulge δ , we observe that the behavior is given by a non-uniform circulation with a period that equals the orbital period of Mercury. Thus, it behaves almost like a rigid body regarding the orientation of the equatorial tidal bulge. This can be seen if we consider Eq. (7) and make $\gamma = 0$ (corresponding to a rigid body). In this case, the differential equation becomes

$$\dot{\delta} = \Omega - \dot{\varphi}, \tag{35}$$

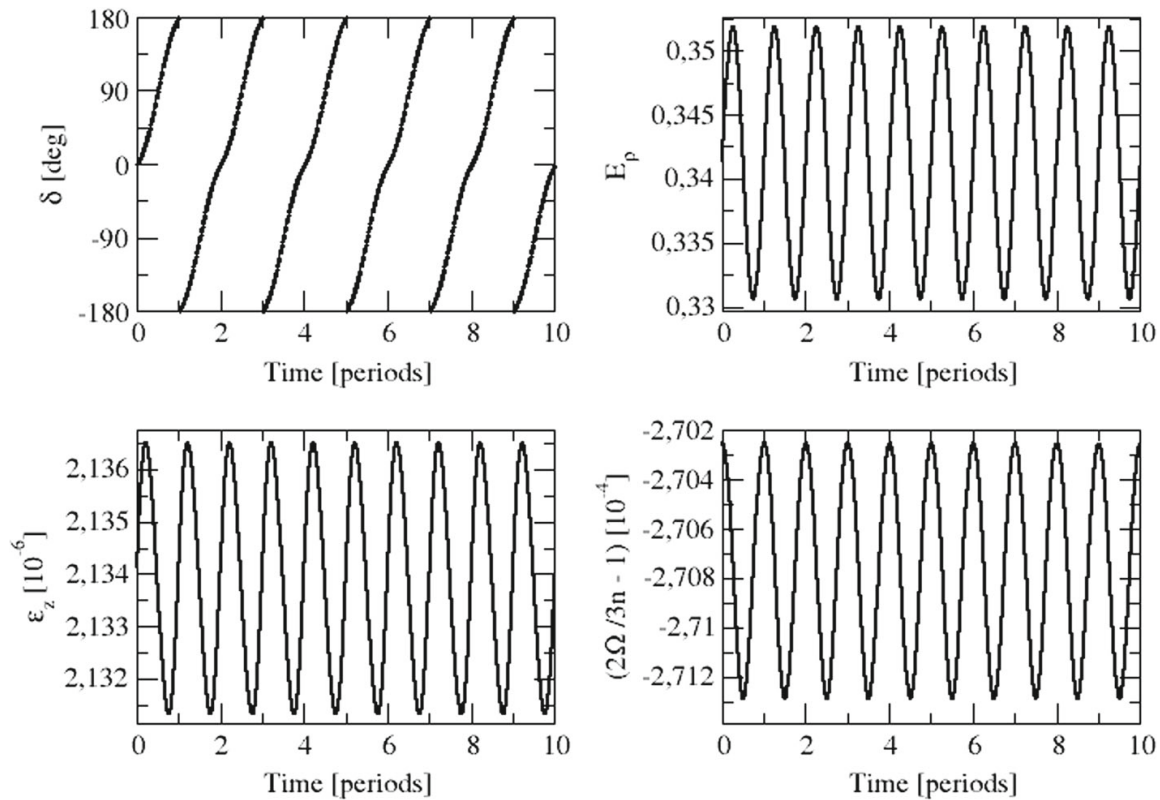


Fig. 5 Evolution of the lag (δ), flattenings (E_ρ and E_z) and rotation velocity (Ω) of the resulting ellipsoid for the $3/2$ spin-orbit resonance, considering a homogeneous non-rigid Mercury with eccentricity $e = 0.1$. In this case, we adopted $\gamma/n = 0.01$ (corresponding to $\gamma = 8.27 \times 10^{-9} \text{ s}^{-1}$)

the solution of which shows that δ circulates with a period

$$T_\delta = \frac{2\pi}{\Omega - \dot{\varphi}}. \quad (36)$$

Since we have, in the $3/2$ spin-orbit resonance, $\Omega/n \approx 3/2$, it follows that $T_\delta = 4\pi/n$. Thus, in the case of a rigid body in the $3/2$ spin-orbit resonance, δ circulates with a period equal to twice the orbital period of Mercury. Fig. 5 shows the evolution of the shape, orientation and rotation of the body when $\gamma/n = 0.01$ for the $3/2$ spin-orbit resonance. For smaller values of γ/n , the mean value of Ω in the $3/2$ spin-orbit resonance is higher, and the amplitudes of the oscillations become smaller.

Figure 6 shows the evolution of δ in the neighborhood of the $3/2$ spin-orbit resonance for four different values of γ/n . The behavior of δ strongly depends on the value of γ/n . As γ increases, there is a critical point where the regime of δ changes from circulation to oscillation. The transition between the two regimes can be seen comparing the blue and the red curves in the figure. The results in Fig. 6 show that the body behaves almost like a rigid body even for values of γ/n for which the body is not necessarily trapped in the spin-orbit resonance. It is worth emphasizing that the $3/2$ spin-orbit resonance is the case of Mercury's rotational configuration.

Figure 7 shows the geometrical configuration of the ellipsoidal figure of the body, with bulges indicated by black areas for different times. From the figure, it can be seen that it behaves almost like a rigid body when it is trapped in the $3/2$ spin-orbit resonance. For every 2 orbital periods, δ circulates from 0 to 2π .

Fig. 6 Evolution of δ in the neighborhood of the condition $\Omega/n = 3/2$. The γ/n factor varies in each curve in the following way: $\gamma/n = 0.251, 0.316, 0.398$ and 0.501 in the black, red, blue and green curves, respectively. In all cases, the eccentricity is fixed as $e = 0.1$. The behavior of δ depends not only on the value of Ω/n , but also on the ratio γ/n . We see from the red and blue curves that the limit value for which δ circulates or oscillates lies between 0.398 and 0.316

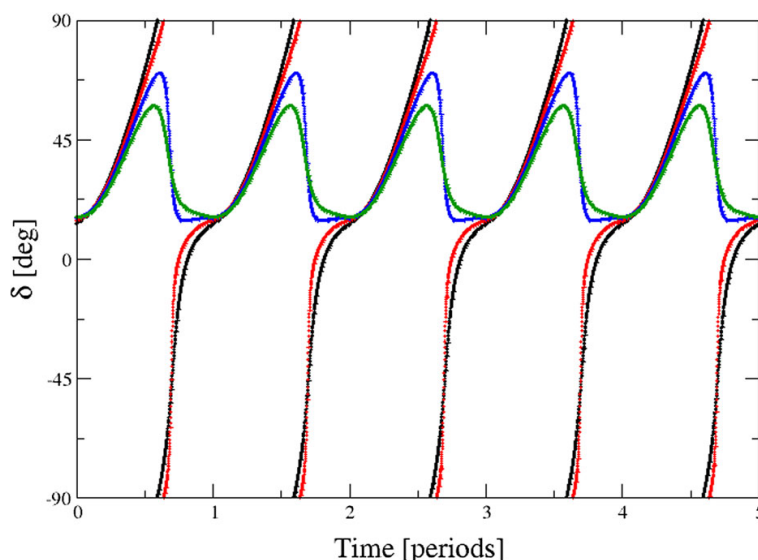
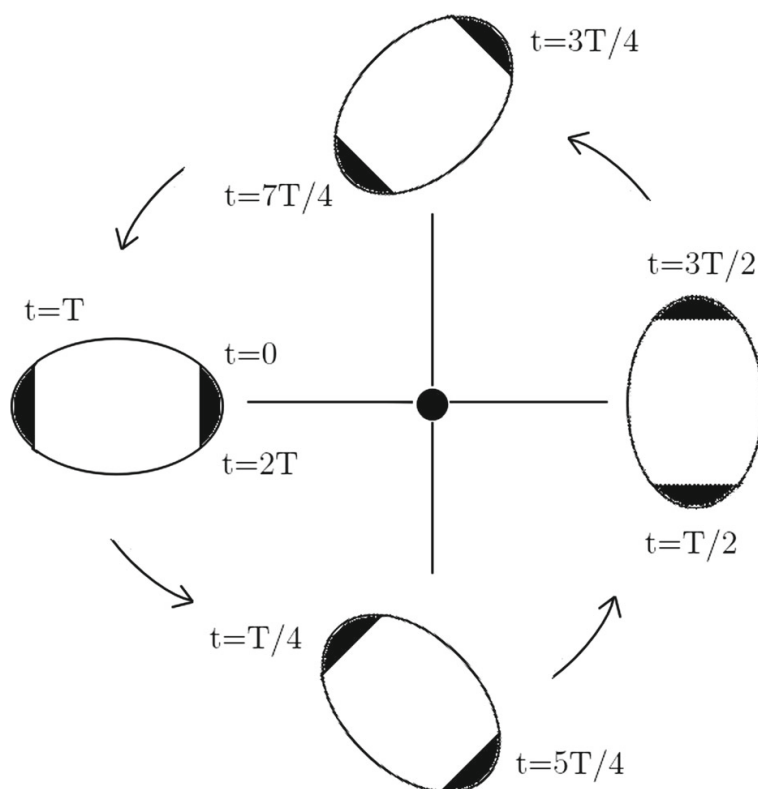


Fig. 7 Geometrical configuration of the resulting ellipsoid of Mercury in the case of the $3/2$ spin-orbit resonance when γ is very small. In this case, the body behaves like a rigid body. The configuration at different times is shown along with the respective time on the side of the black areas. After one orbital revolution, the orientation of the ellipsoid is reversed (i.e., the orientation of the ellipsoid is rotated by 540 deg.). The arrows indicate the chronological sequence of the figures



4.2 The $2/1$ spin-orbit resonance

In this subsection, we perform a discussion similar to the one presented in the previous subsection, but for the $2/1$ spin-orbit resonance.

The results in Fig. 8 show the same qualitative features for the equatorial prolateness, polar oblateness and rotation rate as it was done in the case of the $3/2$ spin-orbit resonance. The only additional interesting feature is that for the $2/1$ spin-orbit resonance, the oscillations in E_ρ and Ω/n have two noticeable harmonic components. One of the components has a period of $2\pi/n$, while the second component has a period of π/n (cf. top graph on the right in Fig. 8). Regarding the behavior of δ , the period of circulation in the case of the $2/1$ spin-orbit resonance is equal to the orbital period of Mercury. This result is important because, as in

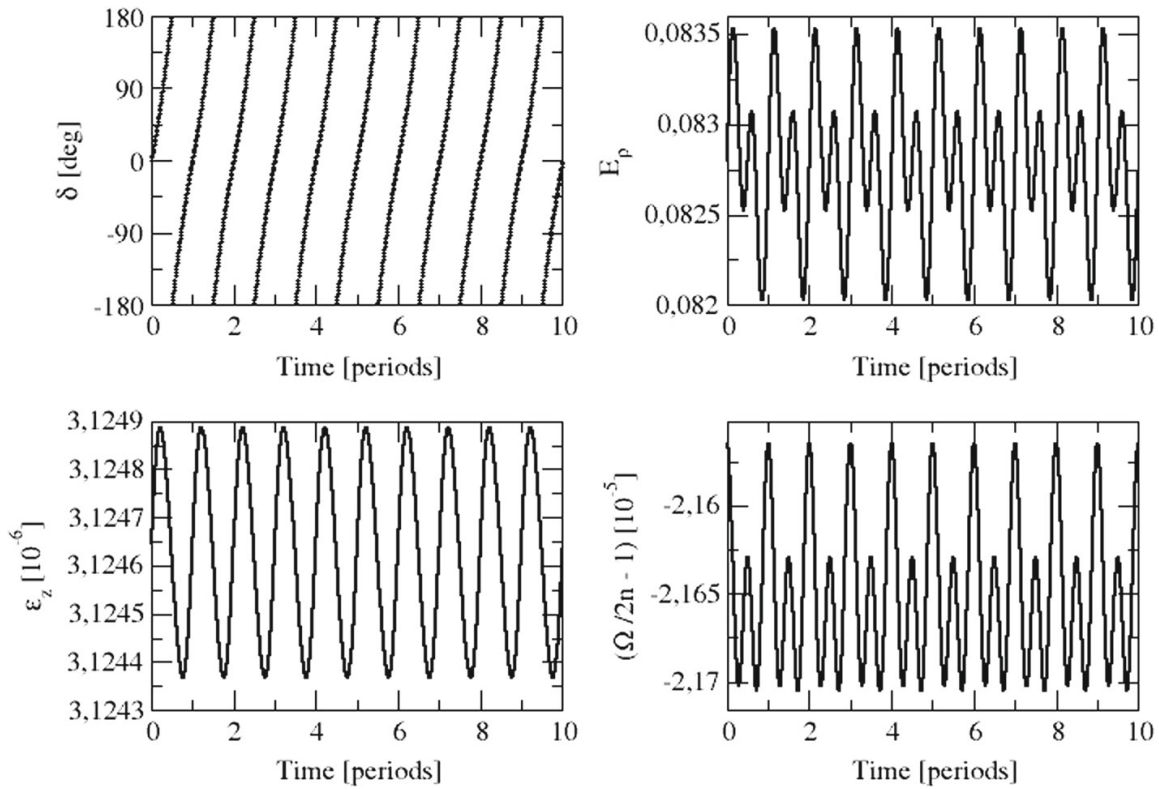
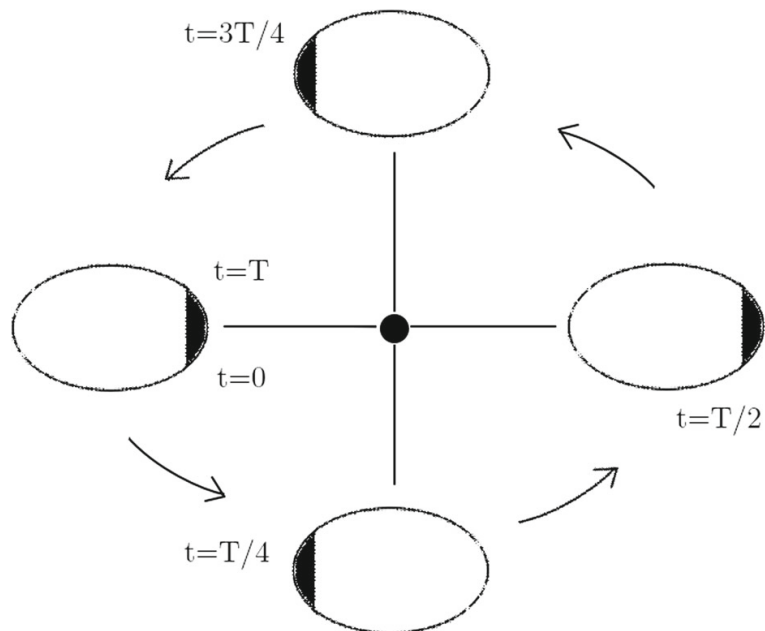


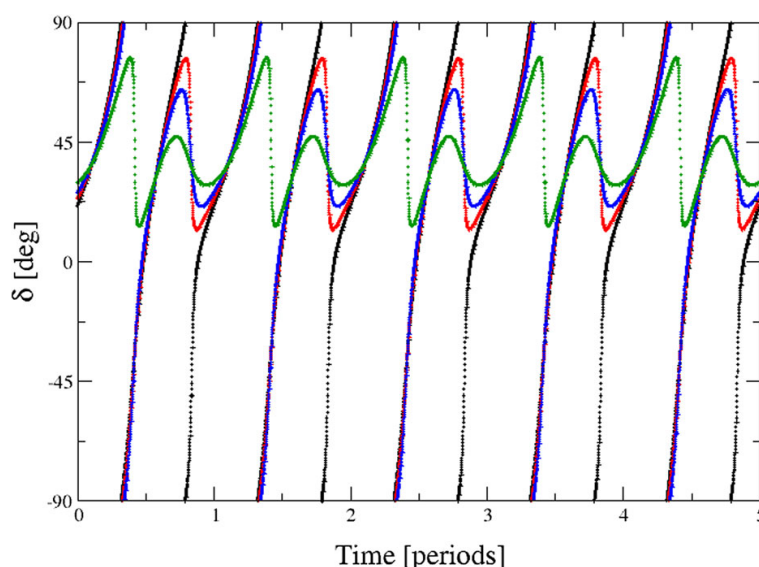
Fig. 8 Evolution of the lag (δ), flattenings (E_ρ and E_z) and rotation rate Ω of a non-rigid body in the 2/1 spin-orbit resonance with $\gamma/n = 0.001$ (corresponding to $\gamma = 8.27 \times 10^{-10} \text{ s}^{-1}$) and $e = 0.1$. The behavior of E_ρ , E_z and Ω/n is qualitatively the same as in the 3/2 spin-orbit resonance

Fig. 9 Geometrical configuration of the resulting ellipsoid in the case of the 2/1 spin-orbit resonance when γ is very small. In this case, the body behaves like a rigid body. As in the Fig. 7, the arrows indicate the chronological sequence of the figures



the case of the 3/2 spin-orbit resonance, the body behaves almost like a rigid body when it is trapped in the spin-orbit resonance [also in agreement with Eq. (36)]. The geometrical configuration of the body's figure can be seen in Fig. 9. The ellipsoidal bulge rotates around the body's center of mass with the same period as the orbital motion w.r.t the position of the companion (which corresponds to δ). If we considered $\varphi_B = \varphi + \delta$, corresponding to an origin in a fixed point in space, the period would be half of the orbital period.

Fig. 10 Evolution of δ in the neighborhood of the condition $\Omega/n = 2$. The γ/n factor is equal to 0.1, 0.126, 0.158 and 0.3 in the black, red, blue and green curves, respectively. In the black curve, the period of circulation of δ is equal to half of the orbital period. In the blue and red curves, the period of circulation increases to one orbital period and in the green curve, δ oscillates around 45 deg



In Fig. 10, we repeat the analysis done for the 3/2 spin–orbit resonance regarding the evolution of δ in the proximity of the resonance. We can see that even for a value of γ/n higher than the critical value necessary for the 2/1 spin–orbit to exist, δ circulates with a period equal to the orbital period (see black curve in Fig. 10). Thus, there is a range of values for γ/n for which the period of circulation is equal to the orbital period. If γ/n is higher than such range of values, the period of circulation becomes twice the orbital period, which was the case for the 3/2 spin–orbit resonance (see red and blue curves in Fig. 10). Finally, the green curve in Fig. 10 shows that δ oscillates around 45 deg. when γ/n is even higher than the range for which δ circulates with a period equal to twice the orbital period. Therefore, for the 2/1 spin–orbit resonance, there are three possible behaviors for δ that depend on the value of γ/n .

5 Trapping into the 3/2 spin–orbit resonance

In this section, we use the same equations as Folonier et al. (2018) to study the rotational evolution of a body that is captured in the 3/2 spin–orbit resonance as a consequence of tidal interactions and analyze the range of values of γ able to drive the body’s rotation to this spin–orbit configuration.

Figure 11 shows the secular variation of the quasi-steady rotation rate $\Delta_{QS}(\Omega/n)$ as a function of the rotation rate Ω/n . To obtain the secular variation of the rotation rate, we integrated Eqs. (7)–(10) with a given initial rotation rate until the rotation was captured in a quasi-steady state. Then, for each 100 orbital periods, we calculated the difference Ω/n w.r.t the previous value 100 periods before. Many aspects are presented in Fig. 11. We see that, for $\gamma \ll n$, the number of possible spin–orbit resonances is larger for higher eccentricities (compare the panels on Fig. 11). The appearance of stable points (i.e., possible spin–orbit resonances) for larger eccentricities and low values of γ/n was already studied in Correia et al. (2014) and Ferraz-Mello (2015a). The results presented in Fig. 11 are in agreement with both these works.

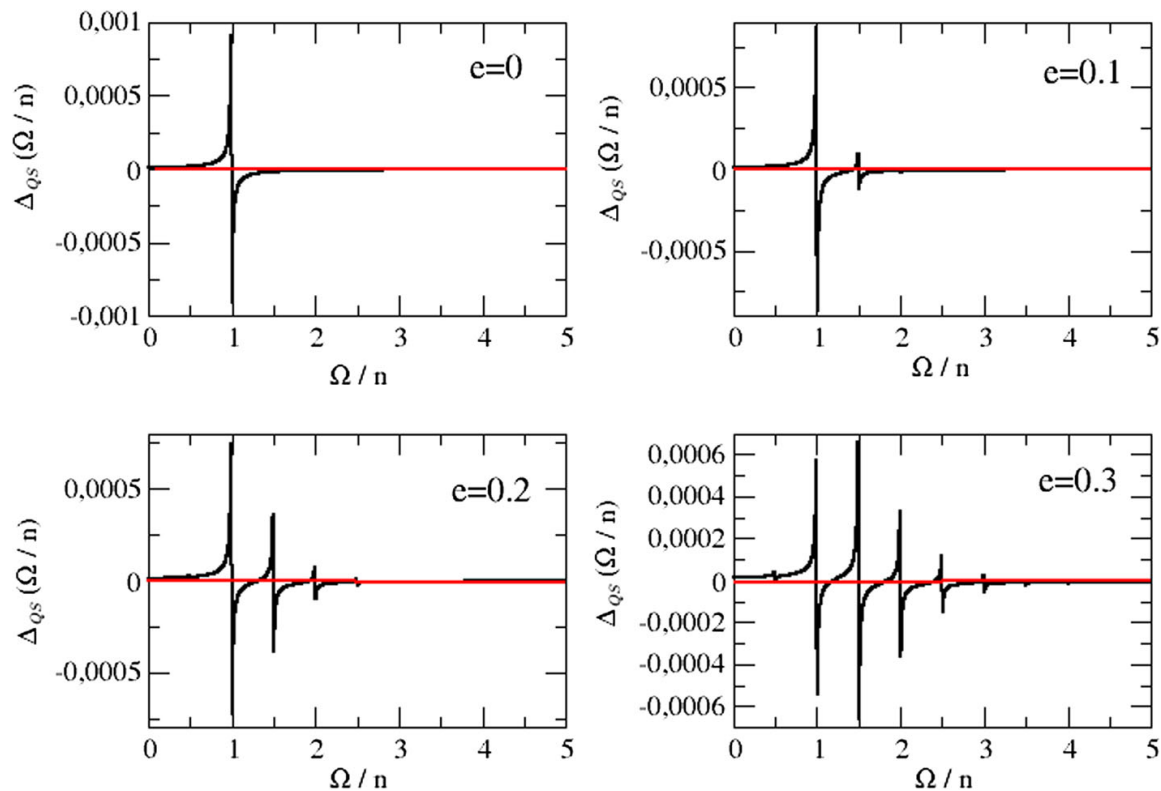


Fig. 11 Secular variation of the rotation rate $\Delta(\Omega/n)$ as a function of the rotation rate Ω normalized by the mean motion when $\gamma/n = 10^{-2}$. When the eccentricity increases, the number of visible stable solutions also grows, as can be seen by comparing the panels in the figure

5.1 Constraints for the relaxation factor

In order to evaluate the relaxation factor of a body whose final rotational configuration is the 3/2 spin–orbit resonance, we perform full numerical integrations of Eqs. (7)–(10) for selected initial conditions just above the 3/2 and 2/1 spin–orbit resonances.

Figure 12 shows the rotational evolution of a non-rigid homogeneous Mercury considering two values of eccentricity and initial values of rotation rate for different values of γ . We can see that the final equilibrium value of the rotation rate depends on all those parameters. Thus, the value of γ must be in a range such that the current rotational configuration is obtained considering the eccentricity variations of the body. There are two conditions that must be taken into account. Firstly, the relaxation factor must be such that the body does not escape the 3/2 spin–orbit resonance when its eccentricity reaches the minimum value. Also, the body may have passed the 2/1 spin–orbit resonance without remaining captured into it even when the minimum eccentricity was reached. In the case of Mercury, studies on its eccentricity history for the last 200 Myr have shown that the eccentricity oscillated between 0.1 and 0.3 (see Laskar 1996). For $e = 0.1$ and by following the two criteria established just above, we obtain $5.8 \times 10^{-3} \leq \gamma/n \leq 5.8 \times 10^{-2}$, which corresponds to $4.8 \times 10^{-9} \text{ s}^{-1} \leq \gamma \leq 4.8 \times 10^{-8} \text{ s}^{-1}$ (using $n = 8.2677 \times 10^{-7} \text{ s}^{-1}$ as it is the case of Mercury’s orbit).

Figure 13 summarizes our results for the relaxation factor of the non-rigid body whose final rotational configuration is the 3/2 resonance. We performed numerical integrations of Eqs. (7)–(10) for the body assuming, initially, that $\Omega/n = 2.2$ for a range of γ/n between 10^{-1} and 10^{-3} . We see that the only necessary information to determinate the boundary values for the relaxation factor is the minimum eccentricity of the body. The red line in the figure represents the minimum eccentricity for Mercury in the past 200 Myr. The intersection

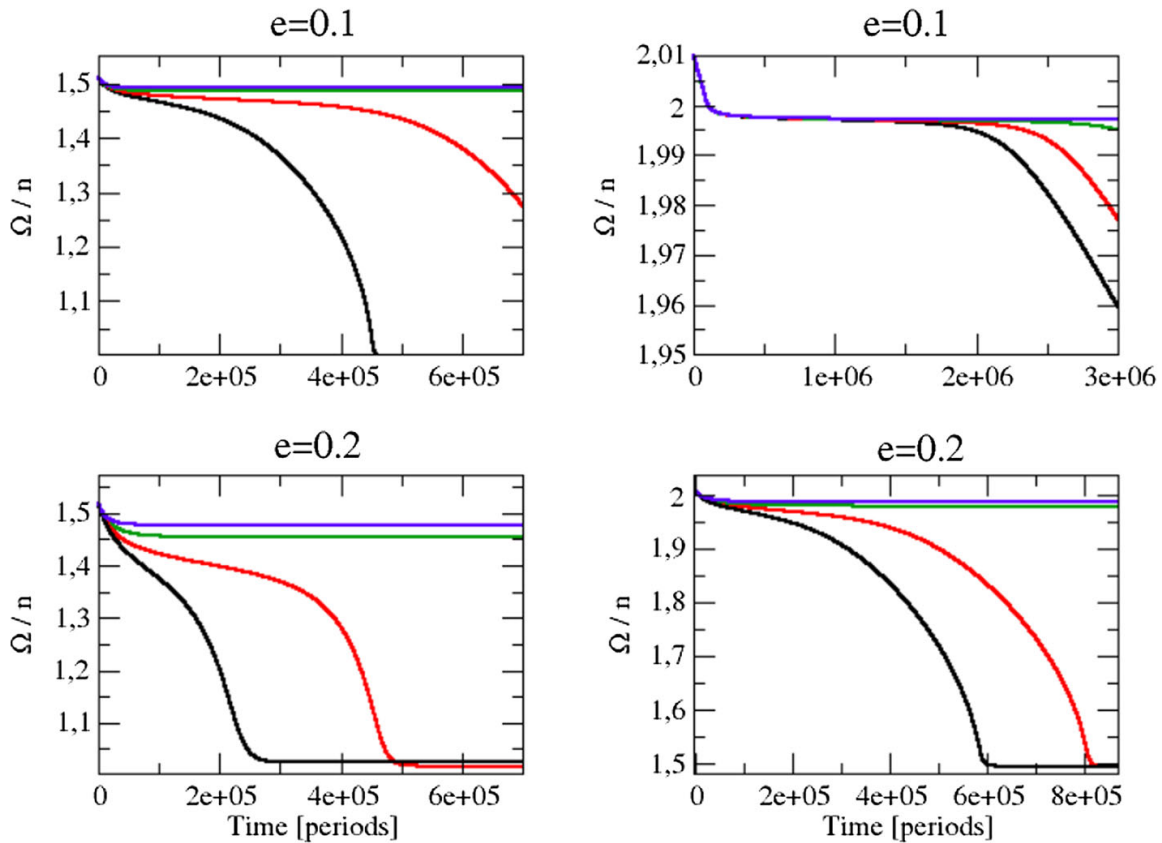
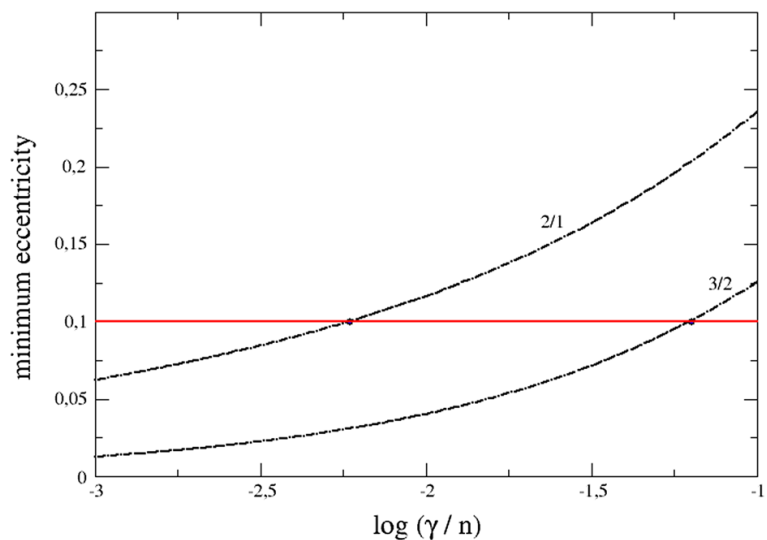


Fig. 12 Evolution of the rotation rate of the body considering different values of γ (varying in uniform steps from the blue to the black curve from the lowest to the highest values) and for two eccentricities. We have $e = 0.1$ on the panels on the top and $e = 0.2$ on the panels on the bottom. In the top left panel, we have γ/n between 0.07 and 0.04 (corresponding to η between 4.0×10^{17} Pa s and 6.9×10^{17} Pa s) from the black to the blue curve. For the top right panel, γ/n is between 0.0059 and 0.0058 (corresponding to η between 4.9×10^{18} Pa s and 5.0×10^{18} Pa s). In the bottom left panel, γ/n varies between 0.30 and 0.15 (corresponding to η between 9.7×10^{16} Pa s and 1.9×10^{17} Pa s). On the bottom right panel γ/n is between 0.07 and 0.05 (corresponding to η between 4.1×10^{17} Pa s and 5.8×10^{17} Pa s)

Fig. 13 Minimum possible eccentricity for two spin-orbit resonances as a function of $\log(\gamma/n)$. The red line shows the minimum eccentricity for Mercury and, thus, establishes the upper and lower boundary values for its γ/n (see also Fig. 5 of Correia et al. 2014)



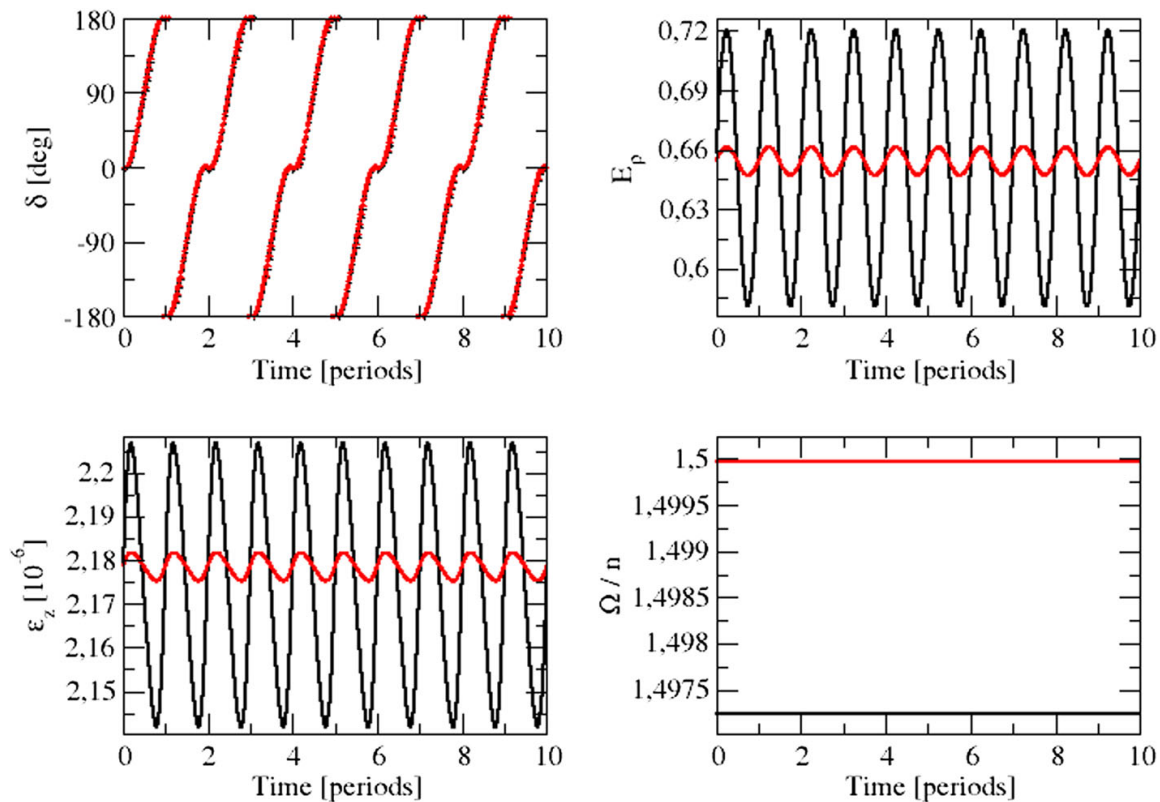


Fig. 14 Deviation angle (δ), normalized equatorial prolateness (E_ρ), polar oblateness (\mathcal{E}_z), and mean value of the rotation rate as a function of the time. The black curve corresponds to $\gamma = 4.8 \times 10^{-8} \text{ s}^{-1}$ and the red curve to $\gamma = 4.8 \times 10^{-9} \text{ s}^{-1}$. In both cases, we adopted $e = 0.2056$

of the two black curves and the red line determinates the boundary values for Mercury's γ/n . It is important to emphasize that, for Mercury, the rotation could have been captured in other spin-orbit resonances before the 3/2 resonant configuration was reached. If we assume, for instance, a previous fast rotating Mercury with $\Omega/n > 2$ and $e > 0.1$, the rotation could have been temporarily trapped in the 2/1 spin-orbit resonance, provided γ was closer to the inferior boundary value (see red line in Fig. 13). However, when Mercury reached the minimum eccentricity, the rotation would have escaped the 2/1 resonance and evolved to the 3/2 resonance.

6 Time variation of the shape and orientation of the figure

Figure 14 shows the time variation of the shape and orientation of a non-rigid homogeneous Mercury's figure and the mean value of the rotation rate for the boundary values of γ established in the previous section, based on its current rotational configuration. The mean value of the rotation is larger for the smallest value of γ . Also, the amplitudes of the oscillations of E_ρ and \mathcal{E}_z are larger for the highest value of γ .

Table 1 shows some results of Mercury's polar oblateness and equatorial prolateness, namely the flattenings mean values of the hydrostatic case (Eqs. 2 and 3, corresponding to $\gamma \rightarrow \infty$), the flattenings mean values of the hydrodynamic equilibrium case of the creep tide theory (cf. Fig. 14), the results obtained by converting the values of J_2 and C_{22} obtained by Matsuyama and Nimmo (2009; Eq. (43)) using the Darwin-Kaula model in the case of a

Table 1 Values of the equatorial prolateness and polar oblateness of a homogeneous non-rigid Mercury in the 3/2 spin-orbit resonance, for $e = 0.2056$

Reference	Equatorial prolateness	Polar oblateness
Static case (Eqs. 2 and 3). Mean values	1.697×10^{-6}	2.966×10^{-6}
Creep tide (cf. Fig. 14). Mean values	1.11×10^{-6}	2.18×10^{-6}
Darwin-Kaula model (Matsuyama and Nimmo 2009)	1.1×10^{-6}	2.2×10^{-6}
MESSENGER data (Perry et al. 2015)	5.45×10^{-4}	9.61×10^{-4}

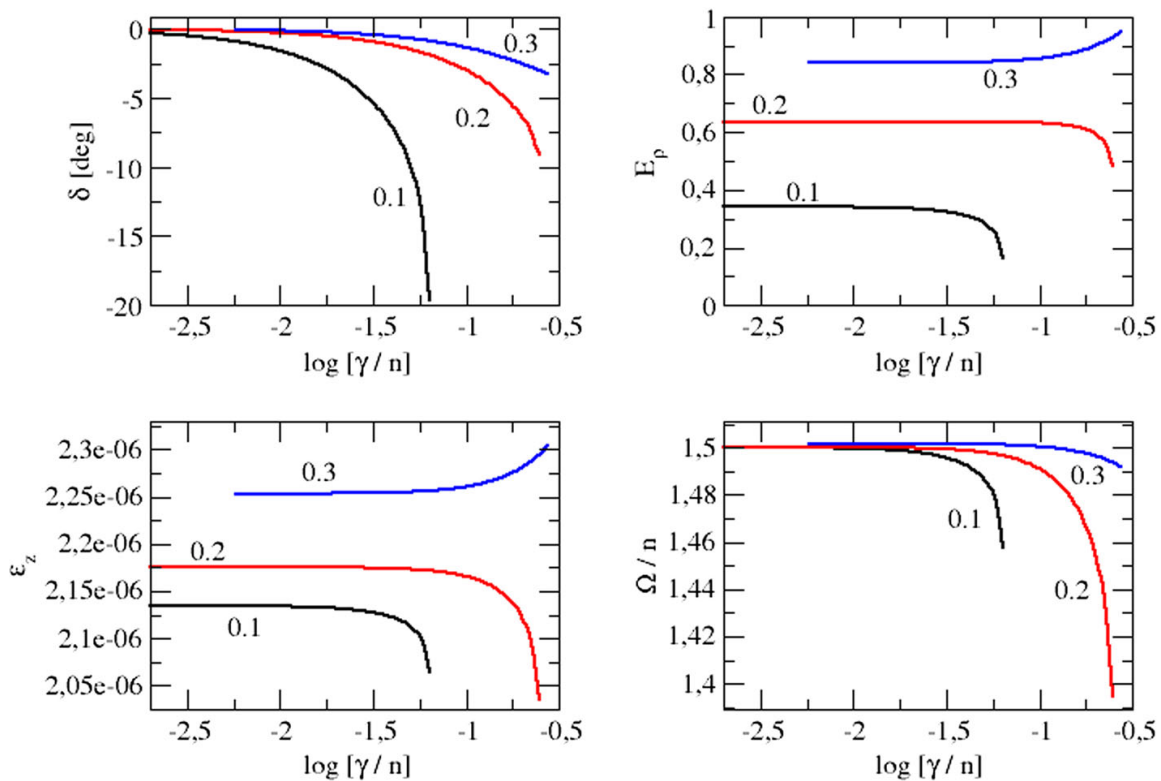


Fig. 15 Values of the deviation angle (δ), normalized equatorial prolateness (E_ρ), polar oblateness (\mathcal{E}_z), and mean value of the rotation rate in the periapsis of Mercury’s orbit for three values of eccentricities as a function of $\log(\gamma/n)$. We have $e = 0.1$, $e = 0.2$ and $e = 0.3$ on the black, red and blue curves, respectively

homogeneous fluid Mercury ($k_2^{T*} = 3/2$), and the values obtained by converting the values of J_2 and C_{22} obtained from MESSENGER’s measurements (Perry et al. 2015).

Because of the rotation of δ and its periodicity, it is useful to characterize the figure parameters by their values at a well defined moment, namely the time of perihelion passage.

In Fig. 15, we can see the values of the equatorial prolateness (in units of $\bar{\epsilon}_\rho$), polar oblateness, rotation rate and deviation angle at the perihelion of the orbit for a range of values of γ . For smaller γ , the rotation rate is closer to the exact 3/2 spin-orbit resonance, and δ is close to zero. As γ increases, δ increases significantly until approximately 20° in the case of $e = 0.1$ (see black curve on the top left panel of Fig. 15). Also, the value of Ω/n becomes significantly lower than 1.5 for higher values of γ .

Since we have shown a method to determinate the boundary values for γ based on the final rotational configuration of the body, and applied such method to Mercury, we can now

compare our results to the observed data for Mercury. Perry et al. (2015) give the values of Mercury's principal axes and deviation angle, based on MESSENGER's data. Our range of values for δ at the perihelion of Mercury's orbit encompasses the values given by Perry et al. However, for E_ρ and \mathcal{E}_z , the creep tide theory predicts a value two orders of magnitude smaller than the value reported by Perry et al. There are no values of γ for which Perry's values for E_ρ and \mathcal{E}_z could be obtained by considering tidal interactions alone. In addition, this discrepancy between the results is independent of the tidal model used. The observed values for Mercury's E_ρ and \mathcal{E}_z cannot be obtained by any tidal theory for Mercury's figure evolution, assuming hydrodynamic equilibrium.

Currently, it is well-known that Mercury's internal structure is not homogeneous. One attempt to solve the problem concerning the differences in E_ρ and \mathcal{E}_z is the extension of the creep tide theory for the case of a differentiated Mercury. We performed numerical integrations for a differentiated Mercury with three layers considering an approximation of the model for Mercury's interior structure proposed in Steinbrügge et al. (2018). The value for the crust's relaxation factor that we have from such interior structure model is four orders of magnitude smaller than the lower boundary value that we determined for a homogeneous Mercury. However, the results taking into account Mercury's differentiated structure yield approximately the same order of magnitude for E_ρ and \mathcal{E}_z when compared to the homogeneous model. (The values for the differentiated case are, in fact, smaller than the homogeneous ones.) Moreover, a model taking into account the differentiation of Mercury and the lower viscosity of the fluid core of the planet should be responsible for a tidal deformation of the order of the static tide of the homogeneous model (Steinbrügge et al. 2018), thus creating a tidal torque efficient to drive the system to the capture into the 3/2 resonance. To study Mercury's rotational evolution with the current observed values for E_ρ and \mathcal{E}_z , we would need to consider that there are permanent components for both the equatorial prolateness and polar oblateness coefficients (see e.g., Bartucelli et al. 2017).

7 Conclusion

We have used the new version of the creep tide theory (Folonier et al. 2018) to study the rotational evolution of a homogeneous non-rigid body for various rotational configurations. We considered a homogeneous viscous body which is under the action of the centrifugal potential from its own rotation and the gravitational attraction of a companion. No permanent equatorial asymmetry is assumed.

The creep tide theory allows us to obtain the time evolution of the body's figure as well as its rotation. The differential equations to be solved in this new version of the creep tide theory are significantly simpler than the equations of the previous formulation of the theory (Ferraz-Mello 2012, 2013, 2015a). Moreover, in the new formulation of the creep tide theory, we do not assume a constant rotation rate in the early steps of the development of the theory as a working hypothesis, as it was previously done. It is worth noting that the equations of the new formulation of the creep tide theory are virtually equivalent to the equations of the Maxwell viscoelastic model studied by Correia et al. (2014). In fact, the two models become equivalent when the elastic terms are neglected (see Ferraz-Mello 2015b).

The dynamics of capture of a non-rigid Mercury in the 3/2 resonance was revisited. Studies of the dynamics of capture in spin-orbit resonances have been thoroughly discussed before by Makarov and Efroimsky (2013), Correia et al. (2014) and Ferraz-Mello (2014, 2015a) and much of their findings are repeated in this paper for the sake of completeness. It was shown

that spin–orbit resonances ensue for bodies with a low value of the relaxation factor, and the number of spin–orbit resonances in which an initially fast rotating body may be captured increases with the eccentricity. Analytical expressions for the minimum eccentricity for which the possibility of capture in the 3/2 and 2/1 spin–orbit resonances exists were presented, their results being in excellent agreement with numerical experiments. For the comparison with the numerical experiments, we considered several numerical integrations of the equations for the time evolution of the ellipsoid’s shape and the rotational evolution of the body, where the initial rotation rate was set very close to the exact values of the spin–orbit resonances (e.g. $\Omega = 3n/2$ for the 3/2 spin–orbit resonance). In each numerical integration, we considered a value for the relaxation factor sufficiently close to the limit value for such resonance to exist.

Additionally to the study of the capture in spin–orbit resonances, we also studied the figure evolution of the body when it is trapped in the 3/2 and 2/1 spin–orbit resonances. It was shown that the tidal lag (δ) can either circulate or oscillate around 0. For instance, in the case of the 3/2 spin–orbit resonance, the angle $\varphi_B = \delta + \varphi$ circulates with the same period of the rotation, for low values of γ . For big values of γ , δ oscillates around 0; thus, the bulge oscillates around the line oriented toward the companion. For the 2/1 spin–orbit resonance, it was shown that for sufficiently low values of γ , the period of circulation of φ_B can be either half or 2/3 of the orbital period, the former corresponding to the behavior of a rigid body. When γ is increased, δ oscillates around 0, and φ_B circulates with the period of the orbital motion.

In what concerns the application of the creep tide theory to the determination of the relaxation factor of a non-rigid Mercury based on its current spin–orbit resonant state, it was shown that the capture in the 3/2 resonance constrains the relaxation factor to be in the interval given by $4.8 \times 10^{-9} \text{ s}^{-1} \leq \gamma \leq 4.8 \times 10^{-8} \text{ s}^{-1}$ (corresponding to $5.1 \times 10^{17} \text{ Pa s} \leq \eta \leq 5.0 \times 10^{18} \text{ Pa s}$) when we assume, as working hypotheses, that (i) Mercury’s eccentricity has never been below $e = 0.1$, (ii) its rotation rate was initially faster than the current value, and (iii) no permanent components of the flattenings existed at the time of capture in the 3/2 spin–orbit resonance. These estimated values for η are much smaller than the values used by Steinbrügge et al. (2018), who assumed that $\eta = 10^{23} \text{ Pa s}$ (which corresponds to γ of the order 10^{-13} s^{-1}) for Mercury’s crust. Some numerical experiments were performed, supposing a differentiated structure for Mercury (based on the theory of Folonier and Ferraz-Mello 2019), using the internal structure model proposed by Steinbrügge et al. (2018). We verified that Mercury’s 3/2 spin–orbit resonant state can be maintained for the value of Mercury’s crust viscosity of Steinbrügge et al. (2018), if the viscosity of the liquid core is small. These preliminary experiments have shown that the rotation of the core may be rapidly driven to the 3/2 spin–orbit resonance when we consider a linear friction acting between the crust and the core.

Finally, the results for the values of the equatorial prolateness and polar oblateness of a non-rigid homogeneous Mercury were compared to the data obtained from the MESSENGER mission. The predicted flattenings, which are at most $\mathcal{E}_\rho = 1.1 \times 10^{-6}$ and $\mathcal{E}_z = 2.2 \times 10^{-6}$ according to the tidal theories, were compared to the values obtained from MESSENGER observations, which give $\mathcal{E}_\rho = 5.5 \times 10^{-4}$ and $\mathcal{E}_z = 9.6 \times 10^{-4}$ (see Perry et al. 2015). The observed equatorial prolateness and polar oblateness coefficients are two orders of magnitude bigger than the values predicted by the tidal theories. This discrepancy between the results for the flattenings holds for any tidal theory based on hydrodynamic equilibrium. We may add that, in the case of a model considering a differentiated structure for Mercury, the values of the crustal flattenings are even smaller than the values of the flattenings of the homogeneous model. These facts suggest the existence of a fossil component, responsible for Mercury’s current shape.

Acknowledgements We thank the two referees for the fruitful discussions about tides and equilibrium figures, which led to an improvement of this paper. This investigation is funded by the National Research Council, CNPq, Grant 302742/2015-8 and by FAPESP, Grants 2016/20189-9 and 2017/25224-0. This investigation is part of the thematic project FAPESP 2016/13750-6.

Compliance with ethical standards

Conflict of interest The authors declare no competing interests.

References

- Arfken, G.: *Mathematical Methods for Physicists*. Chap. IX. Elsevier Academic Press, Cambridge (2005)
- Bartuccelli, M., Deane, J., Gentile, G.: Periodic and quasi-periodic attractors for the spin-orbit evolution of Mercury with a realistic tidal torque. *Mon. Not. R. Astron. Soc.* **469**, 127–150 (2017)
- Chandrasekhar, S.: *Ellipsoidal Figures of Equilibrium*. Chap. VIII. Yale University Press, New Haven (1969)
- Correia, A.C.M., Boué, G., Laskar, J., Rodríguez, A.: Deformation and tidal evolution of close-in planets and satellites using a Maxwell viscoelastic rheology. *Astron. Astrophys.* **571**, A50 (2014)
- Efroimsky, M.: Tidal viscosity of Enceladus. *Icarus* **300**, 223–226 (2018a)
- Efroimsky, M.: Dissipation in a tidally perturbed body librating in longitude. *Icarus* **306**, 328–354 (2018b)
- Ferraz-Mello, S.: Dissipation and Synchronization due to creeping tides. *Comm. AAS/DDA* **43**, #8.06 ([ArXiv:1204.3957v1](https://arxiv.org/abs/1204.3957v1) astro-ph.EP) (2012)
- Ferraz-Mello, S.: Tidal synchronization of close-in satellites and exoplanets. A rheophysical approach. *Celest. Mech. Dyn. Astron.* **116**, 109–140 (2013)
- Ferraz-Mello, S.: 2014, Tidal Synchronization of Close-in Satellites and Exoplanets, Host Stars and Mercury *Comm. AAS/DDA* **45**, #202.01 (2014)
- Ferraz-Mello, S.: Tidal synchronization of close-in satellites and exoplanets: II. Spin dynamics and extension to Mercury and exoplanets host stars. *Celest. Mech. Dyn. Astron.* **122**, 359–389 (2015a) [arXiv: 1505.05384](https://arxiv.org/abs/1505.05384). Errata: *Celest. Mech. Dyn. Astr.* **130**, 78, pp. 20–21 (2018)
- Ferraz-Mello, S.: The small and large lags of the elastic and anelastic tides. The virtual identity of two rheophysical theories. *Astron. Astrophys.* **579**, A97 (2015b)
- Folonier, H.A., Ferraz-Mello, S., Kholshchevnikov, K.V.: The flattenings of the layers of rotating planets and satellites deformed by a tidal potential. *Celest. Mech. Dyn. Astron.* **122**, 183–198 (2015)
- Folonier, H.A., Ferraz-Mello, S., Andrade-Ines, E.: Tidal synchronization of close-in satellites and exoplanets. III. Tidal dissipation revisited and application to Enceladus. *Celest. Mech. Dyn. Astron.* **130**, 78 (2018)
- Folonier, H.A., Ferraz-Mello, S.: Tidal dissipation in synchronous differentiated icy satellites. Application to Enceladus. (submitted to publication) (2019)
- Laskar, J.: Large scale chaos and marginal stability in the solar system. *Celest. Mech. Dyn. Astron.* **64**, 115–162 (1996)
- Makarov, V., Efroimsky, M.: No pseudosynchronous rotation for terrestrial planets and moons. *Astrophys. J.* **764**, 27 (2013)
- Matsuyama, I., Nimmo, F.: Gravity and tectonic patterns of Mercury: effect of tidal deformation, spin-orbit resonance, nonzero eccentricity, despinning, and reorientation. *J. Geophys. Res.* **114**, E01010 (2009)
- Noyelles, B., Frouard, J., Makarov, V., Efroimsky, M.: Spin-orbit evolution of Mercury revisited. *Icarus* **241**, 26–44 (2014)
- Perry, M.E., Neumann, G.A., Phillips, R.J., et al.: The low-degree shape of Mercury. *Geophys. Res. Lett.* **42**, 6951–6958 (2015)
- Steinbrügge, G., Padovan, S., Hussmann, H., Steinke, T., Stark, A., Oberst, J.: Viscoelastic tides of Mercury and the determination of its inner core size. *J. Geophys. Res. Planets* **123**, 2760–2772 (2018)

Publisher's Note Springer Nature remains neutral with regard to jurisdictional claims in published maps and institutional affiliations.

Secular spin-orbit evolution of two-body systems

4.1 Introduction

In this chapter we present the group of differential equations used to compute the evolution of the orbital and rotational parameters of a two-body system. Both bodies are assumed to be extended bodies (i.e., they contribute to the overall tidal orbital evolution process). The theoretical bases of the equations are given by the works of Ferraz-Mello (2015); Ferraz-Mello et al. (2015), Folonier et al. (2015), Folonier et al. (2018), Gomes et al. (2019) and Ferraz-Mello et al. (2020).

4.2 Orbital evolution equations

Following Ferraz-Mello et al. (2020) and references therein, we first write the equation for the evolution of the semi-major axis due to the existence of a disturbing force \mathbf{F} . In terms of the time derivative of the work done by the disturbing force (with $\dot{W} = \mathbf{F} \cdot \mathbf{v}$, where \mathbf{v} is the velocity vector), we have

$$\frac{da}{dt} = \frac{2a^2}{GMm} \dot{W}. \quad (4.1)$$

It is worth mentioning that Eq.(4.1) was obtained by using the definition of orbital energy as $E_{orb} = -\frac{GMm}{2a} + M\delta U$ because of the explicit time dependence of the potential.

The eccentricity evolution equation is obtained by considering the expression for the orbital angular momentum (namely, \mathcal{L}_{orb}), which reads

$$\mathcal{L}_{orb} = \frac{GMm}{na} \sqrt{1 - e^2}. \quad (4.2)$$

Differentiating Eq. (4.2) with respect to time and rearranging to get the expression for the time evolution of the eccentricity leads to

$$\frac{de}{dt} = \frac{1 - e^2}{e} \left(\frac{\dot{a}}{2a} - \frac{\dot{\mathcal{L}}_{\text{orb}}}{\mathcal{L}_{\text{orb}}} \right). \quad (4.3)$$

4.2.1 Free rotating bodies

In the case of free rotating bodies, the expression for the variation of the semi-major axis and the eccentricity due to tidal interactions can be calculated by neglecting the short-period oscillations of the rotation rate. In other words, we can use the equation for the time derivative of the work as calculated in Ferraz-Mello (2015). Using Eqs. (4.1) and (4.3) then leads to¹ (using the semidiurnal frequency $\nu = 2\Omega - 2n$ instead of the rotation rate)

$$\left(\frac{da}{dt} \right)^{(\text{FR})} = \frac{R_i^2 n \bar{\epsilon}_{\rho,i} \alpha_i}{2a} \sum_{k \in \mathbb{Z}} \left[3(2 - k) \frac{\gamma_i (\nu_i + kn) E_{2,k}^2}{\gamma_i^2 + (\nu_i + kn)^2} - \frac{k^2 \gamma_i n E_{0,k}^2}{\gamma_i^2 + k^2 n^2} \right], \quad (4.4)$$

$$\left(\frac{de}{dt} \right)^{(\text{FR})} = -\frac{3R_i^2 n \bar{\epsilon}_{\rho,i} \alpha_i}{4a^2 e} \sum_{k \in \mathbb{Z}} \left[\frac{P_k^{(1)} \gamma_i (\nu_i + kn) E_{2,k}^2}{\gamma_i^2 + (\nu_i + kn)^2} + \frac{P_k^{(2)} \gamma_i n E_{0,k}^2}{\gamma_i^2 + k^2 n^2} \right], \quad (4.5)$$

where the superscript *FR* indicates the free rotating body case and

$$P_k^{(1)} = 2\sqrt{1 - e^2} - (2 - k)(1 - e^2); \quad P_k^{(2)} = \frac{(1 - e^2)k^2}{3}. \quad (4.6)$$

The coefficient α appearing in Eqs. (4.4) and (4.5) is related to the Love number k_2 through

$$\alpha_i = \frac{4}{15} k_{2,i}. \quad (4.7)$$

It is worth mentioning that, for homogeneous bodies, we have $k_2 = 3/2$, thus leading to $\alpha = 2/5$. Non-homogeneous bodies have k_2 and α values always smaller than the values corresponding to the homogeneous body case (see discussions in e.g., Batygin and Adams 2013; Folonier et al. 2015 and references therein).

The Cayley coefficients $E_{q,k}$ can be calculated by direct integration of the integral

¹ Somewhere in Ferraz-Mello (2015), the approximation $n^2 a^3 = GM$ was used. This expression is valid only when $M \gg m$ (which is generally the case for the planetary tides). We did not use this assumption here. Eqs. (4.4) and (4.5) are valid for any mass values of both the primary and the companion, as in Ferraz-Mello et al. (2020), Section 6.1.

$$E_{q,k}(e) = \frac{1}{2\pi\sqrt{1-e^2}} \int_0^{2\pi} \frac{a}{r} \cos[q\varphi + (k-q)\ell] d\varphi, \quad (4.8)$$

where ℓ and φ are the mean and true anomalies, respectively.

The calculation of the Cayley coefficients following Eq.(4.8) leads to a very precise determination of the coefficients. However, the calculation of the integral in Eq.(4.8) at each timestep significantly increases the computational cost of the simulations. We thus adopted a series expansion of the Cayley coefficients to order e^7 , as given in Ferraz-Mello (2015), Appendix B.

4.2.1.1 Bodies in stationary rotation

In the case of synchronous or stationary supersynchronous rotation, we use the expression for the time evolution of the semi-major axis and eccentricity taking into account the short-period oscillations of the rotation rate. In such case, the resulting expressions for the time variation of the semi-major axis and eccentricity, to order e^2 , are given by (see Folonier et al. 2018, Ferraz-Mello et al. 2020)

$$\left(\frac{da}{dt}\right)^{(\text{Sync})} \simeq -\frac{21n\alpha R^2 \bar{\epsilon}_\rho e^2}{a} \frac{\gamma n}{\gamma^2 + n^2}, \quad (4.9)$$

$$\left(\frac{de}{dt}\right)^{(\text{Sync})} \simeq -\frac{21n\alpha R^2 \bar{\epsilon}_\rho e}{2a^2} \frac{\gamma n}{\gamma^2 + n^2}. \quad (4.10)$$

4.3 Rotational evolution equations

The rotation rate evolution equation can be written following the constant rotation rate approximation, which leads to (Ferraz-Mello, 2015)

$$\frac{d\Omega_i}{dt} = -\frac{3GM_j \bar{\epsilon}_{\rho,i}}{2a^3} \sum_{k \in \mathbb{Z}} \frac{\gamma_i (\nu_i + kn) E_{2,k}^2}{\gamma_i^2 + (\nu_i + kn)^2}. \quad (4.11)$$

In the specific case of systems in which the star is a M, K, G or late F (subgiant) star, the effect of the magnetic wind braking of the stellar rotation rate must be taken into account additionally to the tidal interaction effects. In order to include such an effect, we consider the magnetic wind braking as an angular momentum leakage effect. Several works have aimed at a description of this effect in a wide range of stellar types with different

internal structures. We cite the work of Amard et al. (2019) and references therein for a review on this topic. We use the simplified model of Bouvier et al. (1997). The torque acting on the star due to the magnetic wind braking, in such case, is given by

$$\dot{\mathcal{L}}_{\text{wind}} = -f_P K_B \Omega_\star \left(\frac{R}{R_\odot} \right)^{1/2} \left(\frac{M}{M_\odot} \right)^{-1/2} \min(\Omega_\star, \omega_{\text{sat}})^2, \quad (4.12)$$

where f_P is a factor introduced in Pätzold et al. (2012) to account for the less efficient wind braking mechanism in late F IV stars (i.e., subgiant stars), such as CoRoT-21. K_B is a constant with $K_B = 2.7 \times 10^{47} \text{ g cm}^2 \text{ s}$ (corresponding to $K_B = 2.7 \times 10^{40} \text{ kg m}^2 \text{ s}$), and ω_{sat} is the angular velocity at which saturation occurs, with $\omega_{\text{sat}} = 3\Omega_\odot$, $8\Omega_\odot$ and $14\Omega_\odot$ for stars of masses $0.5M_\odot$, $0.8M_\odot$ and $1.0M_\odot$, respectively².

It is worth mentioning that, for fully convective low-mass M stars, more complex models are used in which the coefficient K_B in Eq. (4.12) is not the same for slow and fast rotators. Typical values in the case of slow rotators range from the same value as for solar-like stars to $1.1 \times 10^{47} \text{ g cm}^2 \text{ s}$ depending on the adopted saturation value. For fast rotators, the coefficient value is taken at least one order of magnitude smaller (see Irwin et al. 2011, Section 5.2).

Finally, we mention that, when studying the evolution of two-body systems composed by a star and a gaseous planet, the planetary rotation rate evolves on a timescale much smaller than the corresponding timescales of evolution of the stellar rotation rate and orbital parameters. Thus, we can consider that the planetary rotation is already stationary and super-synchronous from the beginning of the simulation, where the stationary value depends on the eccentricity through (see Hut 1981)

$$\Omega_p = n \frac{1 + \frac{15}{2}e^2 + \frac{45}{8}e^4 + \frac{5}{16}e^6}{(1 + 3e^2 + \frac{3}{8}e^4)(1 - e^2)^{3/2}} = n \left[1 + 6e^2 + \frac{3}{8}e^4 + \mathcal{O}(e^6) \right]. \quad (4.13)$$

4.4 The complete group of spin-orbit evolution equations

In this section we present the complete group of equations to be solved in order to compute the spin and orbital evolution of a given system. In our applications regarding the secular evolution of exoplanetary systems of this thesis, we considered two types of systems:

² For stellar mass values close to but not equal to the three values presented here, we interpolated the value of ω_{sat} considering a third order polynomial interpolation procedure.

A star hosting a hot Jupiter and a star hosting a low-mass planet (i.e., a mini-Neptune or a super-Earth). For the former, both the planetary and the stellar tide may contribute to the overall orbital evolution of the system. Moreover, the planetary tidal interaction has an important contribution on the stellar rotation evolution. For the latter, however, the stellar tide may be neglected due to the small mass of the planet. Additionally, the influence of the planetary tidal interactions on the stellar rotation rate evolution is negligible.

Although we will introduce the specific group of equations of each one of the two aforementioned types of secularly-evolving systems, a comment is noteworthy: In the general case of a secularly-evolving system where we do not know the magnitude of the tidal interaction of each body, the evolution considering the tides in the two bodies must be considered. In such a case, the most general group of equations to be employed is given by Eqs. (4.4), (4.5) and (4.11), where the equation for the contribution of the tidal interactions of each body is obtained by changing the subscript of the parameters in the equations.

4.4.1 Star + hot Jupiter

In this case, the rotation rate of the planet is assumed to be super-synchronous from the beginning of the simulation. The equations for \dot{a} and \dot{e} coming from the planetary tidal contribution are then given by

$$\dot{a}_p \simeq -\frac{21n\alpha_p R_p^2 \bar{\epsilon}_{\rho,p} e^2}{a} \frac{\gamma_p n}{\gamma_p^2 + n^2}, \quad (4.14)$$

$$\dot{e}_p \simeq -\frac{21n\alpha_p R_p^2 \bar{\epsilon}_{\rho,p} e}{2a^2} \frac{\gamma_p n}{\gamma_p^2 + n^2}, \quad (4.15)$$

which are the same equations as in Eqs. (4.9) and (4.10), with the physical parameters of the planet used explicitly.

To add the contribution of the stellar equilibrium tide to the evolution of the orbital elements, we use the equations given in Sec. 4.2.1. Using the symbol \star to refer to the parameters of the star, we have

$$\dot{a}_\star = \frac{R_\star^2 n \bar{\epsilon}_{\rho,\star} \alpha_\star}{2a} \sum_{k \in \mathbb{Z}} \left[3(2-k) \frac{\gamma_\star (\nu_\star + kn) E_{2,k}^2}{\gamma_\star^2 + (\nu_\star + kn)^2} - \frac{k^2 \gamma_\star n E_{0,k}^2}{\gamma_\star^2 + k^2 n^2} \right], \quad (4.16)$$

$$\dot{e}_\star = -\frac{3R_\star^2 n \bar{\epsilon}_{\rho,\star} \alpha_\star}{4a^2 e} \sum_{k \in \mathbb{Z}} \left[\frac{P_k^{(1)} \gamma_\star (\nu_\star + kn) E_{2,k}^2}{\gamma_\star^2 + (\nu_\star + kn)^2} + \frac{P_k^{(2)} \gamma_\star n E_{0,k}^2}{\gamma_\star^2 + k^2 n^2} \right]. \quad (4.17)$$

The evolution of the orbital elements taking into account both the stellar as well as the planetary tides is thus given by

$$\dot{a} = \dot{a}_p + \dot{a}_*, \quad (4.18)$$

$$\dot{e} = \dot{e}_p + \dot{e}_*, \quad (4.19)$$

where the parameters in Eqs. (4.18) and (4.19) are defined in Eqs. (4.14)-(4.17).

For the rotational evolution equations, we remind that the planetary rotation rate is already assumed to be in the supersynchronous state from the beginning of the simulation. The rotation of the planet thus evolves as a function of the eccentricity following (see e.g., Hut 1981)

$$\Omega_p = n \frac{1 + \frac{15}{2}e^2 + \frac{45}{8}e^4 + \frac{5}{16}e^6}{(1 + 3e^2 + \frac{3}{8}e^4)(1 - e^2)^{3/2}} = n \left[1 + 6e^2 + \frac{3}{8}e^4 + \mathcal{O}(e^6) \right]. \quad (4.20)$$

For the rotational evolution of the star, we consider the effects of both the stellar tide as well as the magnetic wind braking of the stellar rotation. Thus,

$$\dot{\Omega}_* = -\frac{3GM_p\bar{\epsilon}_{\rho,*}}{2a^3} \sum_{k \in \mathbb{Z}} \frac{\gamma_*(\nu_* + kn)E_{2,k}^2}{\gamma_*^2 + (\nu_* + kn)^2} - \frac{f_P K_B \Omega_*}{\alpha_* M_* R_*^2} \sqrt{\frac{R_* M_\odot}{M_* R_\odot}} \min(\Omega_*, \omega_{\text{sat}})^2. \quad (4.21)$$

The equations to be integrated to obtain the complete spin-orbit evolution of the system are thus given by Eqs. (4.18), (4.19)³ and (4.21). The planetary rotation rate evolves as a function of the eccentricity following Eq. (4.20). However, we emphasize that the planetary rotation rate is not integrated numerically as it is the case of the orbital parameters and the stellar rotation rate. The group of differential equations we present here were integrated using the Radau 15 integrator (see Everhart 1985 for a description of the numerical integration method). The group of equations described in this section is used in Chapter 5.

³ In practice, when we perform the integration of the eccentricity evolution ODE, we used e^2 instead of e as a variable, since $d(e^2)/dt = 2ede/dt$ does not present divisions by small numbers in the small eccentricity regime.

4.4.2 Star + low-mass planet

In this case, as we briefly mentioned before, planetary tidal interactions are much more significant for the orbital evolution process than the stellar tidal interactions. Moreover, the planetary mass is too small to lead to a significant contribution to the stellar rotation rate evolution. We thus consider that, for such systems, stellar tides can be completely neglected and only the planetary tides need to be taken into account. However, one point of the applications in the case of low-mass planets must be taken into account: for mini-Neptunes, the relaxation factor is of the order of $1 - 50 \text{ s}^{-1}$ (we remind that mini-Neptunes are predominantly gaseous in composition). For super-Earths, however, the relaxation factor value can vary from 10^{-6} s^{-1} to 10^{-9} s^{-1} . In such case, the rotation of the planet can be temporarily captured in spin-orbit resonant states, especially for orbits with eccentricity values such that $e \approx 0.05$ or larger. Then, we employ the following equations to study the spin-orbit evolution

$$\dot{a}_p = \frac{R_p^2 n \bar{\epsilon}_{\rho,p} \alpha_p}{2a} \sum_{k \in \mathbb{Z}} \left[3(2-k) \frac{\gamma_p (\nu_p + kn) E_{2,k}^2}{\gamma_p^2 + (\nu_p + kn)^2} - \frac{k^2 \gamma_p n E_{0,k}^2}{\gamma_p^2 + k^2 n^2} \right], \quad (4.22)$$

$$\dot{e}_p = -\frac{3R_p^2 n \bar{\epsilon}_{\rho,p} \alpha_p}{4a^2 e} \sum_{k \in \mathbb{Z}} \left[\frac{P_k^{(1)} \gamma_p (\nu_p + kn) E_{2,k}^2}{\gamma_p^2 + (\nu_p + kn)^2} + \frac{P_k^{(2)} \gamma_p n E_{0,k}^2}{\gamma_p^2 + k^2 n^2} \right]. \quad (4.23)$$

$$\dot{\Omega}_p = -\frac{3GM_\star \bar{\epsilon}_{\rho,p}}{2a^3} \sum_{k \in \mathbb{Z}} \frac{\gamma_p (\nu_p + kn) E_{2,k}^2}{\gamma_p^2 + (\nu_p + kn)^2}. \quad (4.24)$$

The above group of differential equations is used in Chapter 6 to study the secular evolution of exoplanetary systems containing potentially habitable exoplanets.

Spin-orbit evolution of hot Jupiters around M, K, G and F stars

5.1 Introduction

In this chapter we study the spin and orbital evolution of hot Jupiters around M, K, G and F stars. We employ the equations presented in Chapter 4. We analyse the survival timescale of hot Jupiters around the stars as a function of the stellar relaxation factor and eccentricity of the planet. A comparison of the results obtained in this chapter with the results of previous works (such as McQuillan et al. 2013; Penev et al. 2018 and references therein) is also presented. All the codes used to perform the simulations presented in this chapter are provided in this GitHub repository, under the GNU Affero General Public License (see the LICENSE file for more information regarding the use and distribution of the code).

5.2 Spin-orbit evolution of hot Jupiters around M, K, G and F stars

We consider five systems, corresponding to five different stars (see Table 5.1). For each star, we consider two initial values for the rotation rate (an initially fast and an initially slow rotator, with rotation periods given in Table 5.1). For each rotation rate value, four simulations were performed, each one with a different initial eccentricity value. The values of the eccentricity were: 0, 0.05, 0.1 and 0.2. The planetary rotation rate is assumed to be super-synchronous from the beginning of the simulations. For the sake of clarity and organization of the discussions, we separate the results corresponding to each star in subsections.

Table 5.1 - Data regarding the stellar physical parameters and initial values of the stellar rotation period used in the simulations considered in this section.

System	$M_\star (M_\odot)$	$R_\star (R_\odot)$	$P_{\text{rot},0}$ [days]	$\omega_{\text{sat}} (\Omega_\odot)$	$\gamma_\star [s^{-1}]$	$\gamma_p [s^{-1}]$	Reference M-R values
M0	0.6	0.62	1.6 – 8.0	4.5	8	50	Kaltenegger and Traub (2009)
K2V	0.8	0.96	1.6 – 8.0	8.0	8	50	Cram et al. (1989)
G2V	1.0	1.0	1.6 – 8.0	14.0	8	50	No reference
F6V	1.25	1.359	2.3 – 8.0	16.0	8	50	Pecaut et al. (2012)
F8IV	1.29	1.95	2.3 – 8.0	16.0	8	50	Pätzold et al. (2012)

5.2.1 Evolution results for M star

In this case, we considered the data from the first row of Table 5.1. We considered different colours to distinguish among the eccentricity values. The black, red, blue and green curves correspond to initial eccentricity values of 0, 0.05, 0.1 and 0.2, respectively.

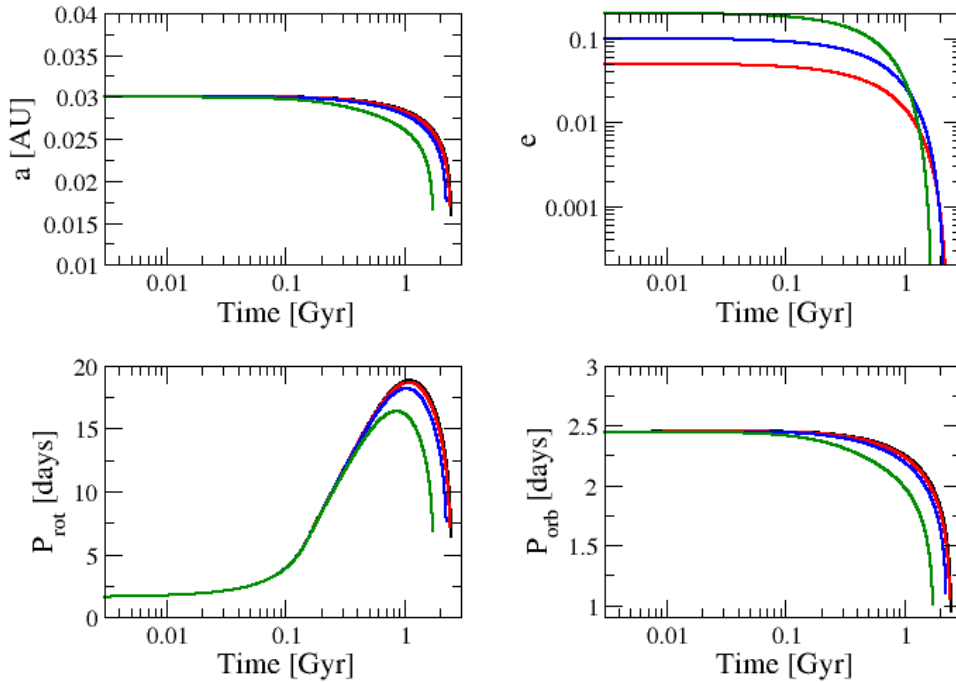


Figure 5.1: Results of the spin-orbit evolution for a close-in Jupiter-like planet around an M star with an initial period of $P_{\text{rot}} = 1.6$ days.

Figs. 5.1 and 5.2 correspond to the results for the initially fast and slow rotators, respectively. We can see that, in all the cases considered, the semi-major axis and eccentricity

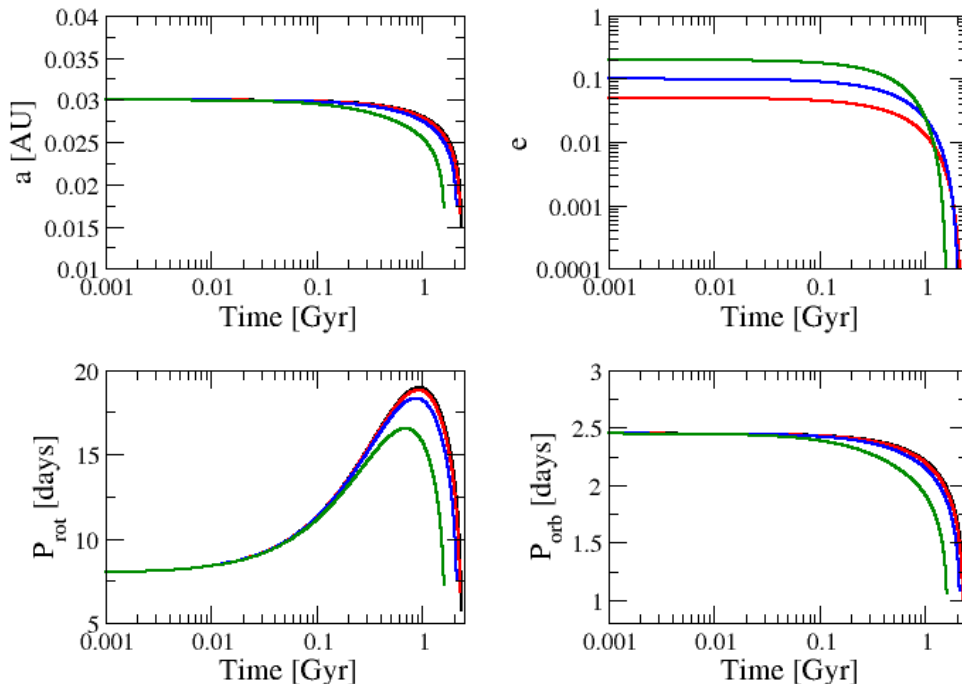


Figure 5.2: Results of the spin-orbit evolution for a close-in Jupiter-like planet around an M star with an initial period of $P_{\text{rot}} = 8.0$ days.

always decrease from the beginning of the simulation until the semi-major axis value reaches the Roche limiting value, corresponding to (see e.g., Penev et al. 2014 and references therein)

$$a_{\text{Roche}} = 2.44R_p \left(\frac{M_\star}{M_p} \right)^{1/3}. \quad (5.1)$$

When the semi-major axis value reaches the value of Eq. (5.1), the planet is destroyed and only the stellar rotation rate continues to evolve following the magnetic wind braking law (see Eq. 4.12).

Regarding the behavior of the stellar rotation period (see the bottom left panel in Figs. 5.1 and 5.2), we note that the stellar rotation period increases at the beginning of the simulation due to the action of the magnetic wind braking (i.e., the magnetic wind braking effect causes a decrease in the stellar rotation rate). The semi-major axis then decreases, which increases the magnitude of planetary tidal interactions. Afterwards, the stellar rotation period decreases as a result of the tidal interactions (i.e., the orbital angular momentum is transferred to the stellar rotational angular momentum) until the planet is finally destroyed. After the planet is destroyed, the magnetic wind braking continues to

extract angular momentum of the star, thus leading to a decrease in the stellar rotation rate (this last feature is not shown in the figures).

In what concerns the influence of the eccentricity value on the evolution of the hot Jupiter, it can be seen that the survival timescale of the planet is smaller for the cases with larger initial values of eccentricity. Such result can be easily explained if we look at Eq. (4.9). The effect of planetary tidal interaction (in the specific case of the supersynchronous rotation) is to decrease the semi-major axis. Moreover, the rate of variation of the semi-major axis is proportional to the square of the eccentricity. Thus, larger eccentricities lead to larger values of da/dt , which in turn lead to a faster orbital decay process. Therefore, the survival timescale is always smaller for the cases with larger initial eccentricity values.

One last aspect to be discussed regarding the simulations presented so far is that the initial value of the stellar rotation rate does not play an important role on the orbital evolution of the system (compare, for instance, top left and top right panels in Figs. 5.1 and 5.2).

5.2.2 Evolution results for K star

In this case, we considered the data for the stellar parameters as shown in the second row of Table 5.1. The results of the simulations are presented in Figs. 5.3 and 5.4.

The qualitative aspects of the results are the same as in the case of the M star. We can see that the semi-major axis and the eccentricity always decrease from the beginning of the simulation. The stellar rotation rate decreases in the beginning of the simulation as a result of the magnetic wind braking. When the semi-major axis becomes sufficiently small, the tidal torque becomes stronger and the orbital angular momentum is transferred to the rotational angular momentum of the star, thus increasing the stellar rotation rate.

One important aspect to be discussed is the difference in the timescale of orbital evolution for the K star in comparison with the M star. We can see that, in all the cases shown in Figs. 5.3 and 5.4, the timescale for orbital decay and planet destruction is much smaller than in the case of the M star. Indeed, the radius of the K star is significantly larger than the radius of the M star. Additionally, the larger mass of the K star leads to larger values of \dot{a}_p and \dot{e}_p . All these factors contribute to decrease the timescale of survival of the planet around the star.

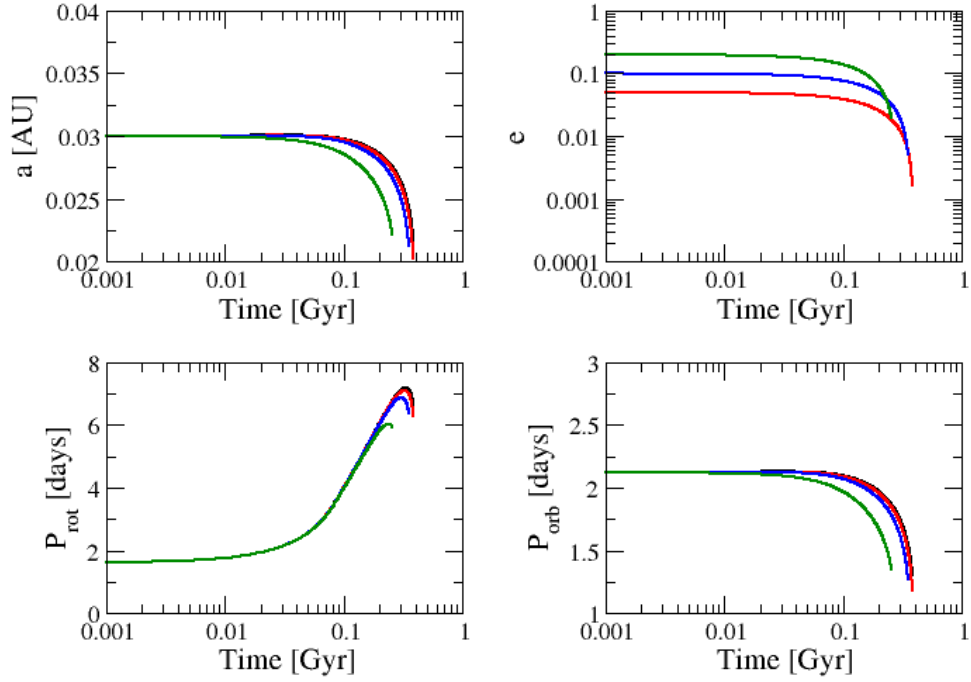


Figure 5.3: Results of the spin-orbit evolution for a close-in Jupiter-like planet around a K star with an initial period of $P_{\text{rot}} = 1.6$ days.

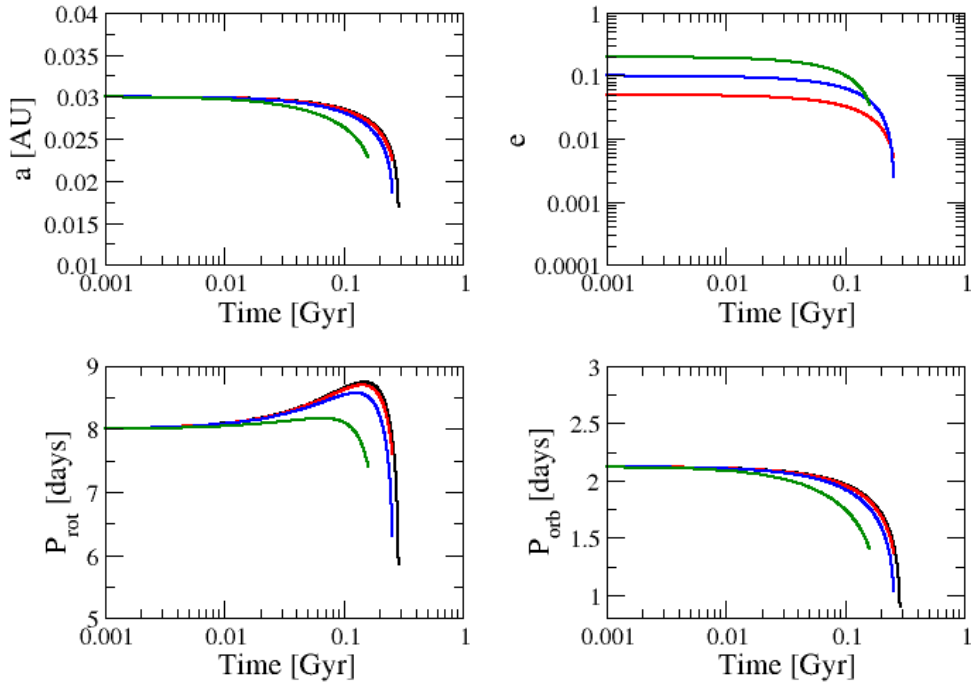


Figure 5.4: Results of the spin-orbit evolution for a close-in Jupiter-like planet around a K star with an initial period of $P_{\text{rot}} = 8.0$ days.

Finally, we point out that, for the K star, the maximum values of the stellar rotation period reached in the simulations are significantly smaller than the corresponding values

for the M star. This result is a consequence of the fact that the mass and radius values of the K star are significantly larger than the M star. As a consequence, the moment of inertia of the K star is larger than the moment of inertia of the M star, and the effect of the magnetic wind braking is weaker for the K star.

5.2.3 Evolution results for G star

In this case, we have a Solar twin hosting a hot Jupiter. The stellar parameters are the ones presented in the third row of Table 5.1. The results of the simulations are presented in Figs. 5.5 and 5.6 (corresponding to the results for the initially fast and slow rotator case, respectively).

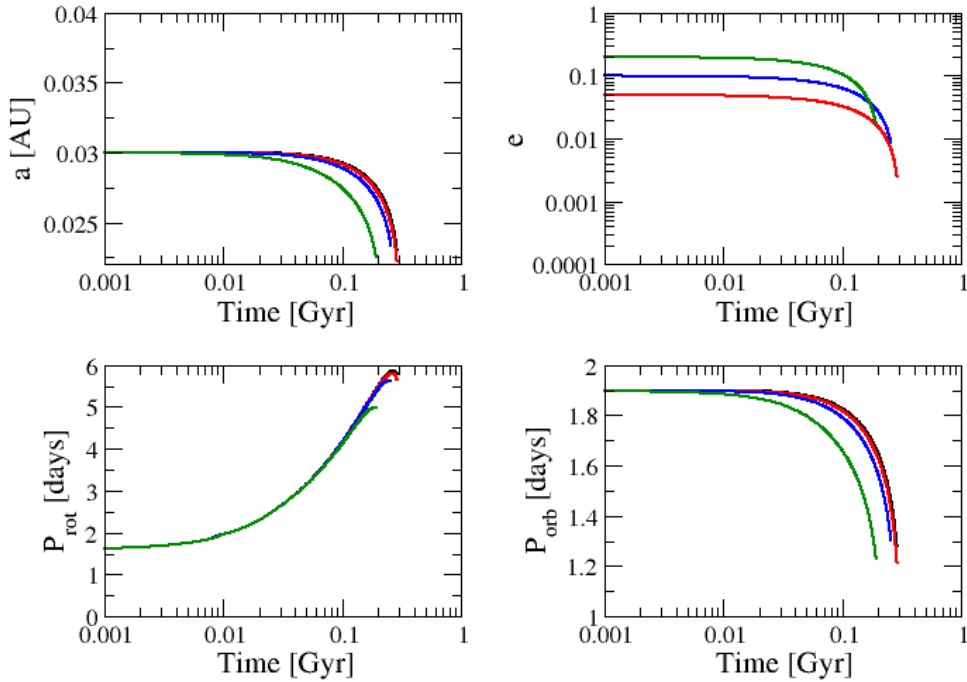


Figure 5.5: Results of the spin-orbit evolution for a close-in Jupiter-like planet around a G star with an initial period of $P_{\text{rot}} = 1.6$ days.

The phenomenological description of the results is very similar to the case of the K star. Indeed, since we adopted a radius value for the G star which is very close to the radius value of the K star, we did not expect very different results regarding the timescales of evolution of the system. The timescales for the planet destruction (i.e., semi-major axis evolution until $a = a_{\text{Roche}}$) is approximately 0.1 Gyr smaller for the G star case in comparison with the K star case results. This result is due to the fact that the mass of the

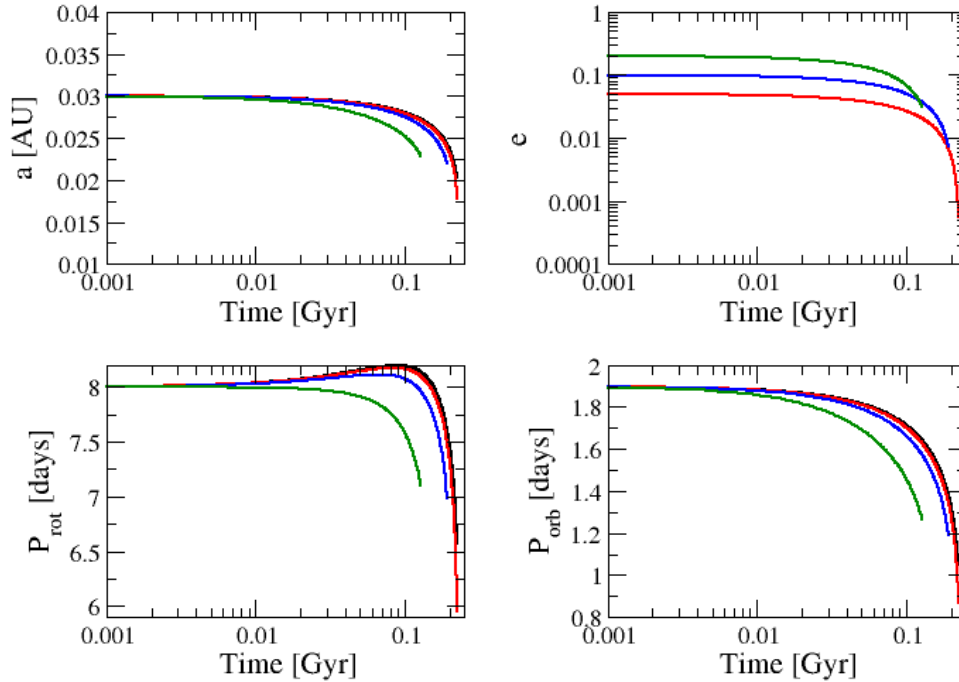


Figure 5.6: Results of the spin-orbit evolution for a close-in Jupiter-like planet around a G star with an initial period of $P_{\text{rot}} = 8.0$ days.

G star is significantly larger than the mass of the K star. Planetary tides are thus stronger for the G star.

5.2.4 Evolution results for a F6V star

Since F6 stars do not experience magnetic wind braking interactions, we neglected the magnetic wind effect by making $f_P = 0$ in the equation for $\dot{\Omega}_*$. Thus, only tidal interactions are responsible for the evolution of both the orbit and the stellar spin. The stellar parameters of this case are shown in the fourth row of Table 5.1. The results of our numerical experiments are presented in Figs. 5.7 and 5.8. It is also worth mentioning that, for the fast rotator case, we adopted $P_{\text{rot}} = 2.3$ days instead of $P_{\text{rot}} = 1.6$ days. Amard et al. (2019) argued that such value for the initial stellar rotation is more realistic since it prevents the star from exceeding its critical rotation velocity (such adjustment is only necessary for stars of masses between 1.2 and 1.5 Solar masses, see discussions in Sec. 2.6 of Amard et al. 2019).

The results of our simulations show that, differently from the cases presented for the M, K and G stars, the planet survives to the orbital evolution process for the initially fast-rotating star case. Indeed, tidal orbital expansion takes place when the rotation rate

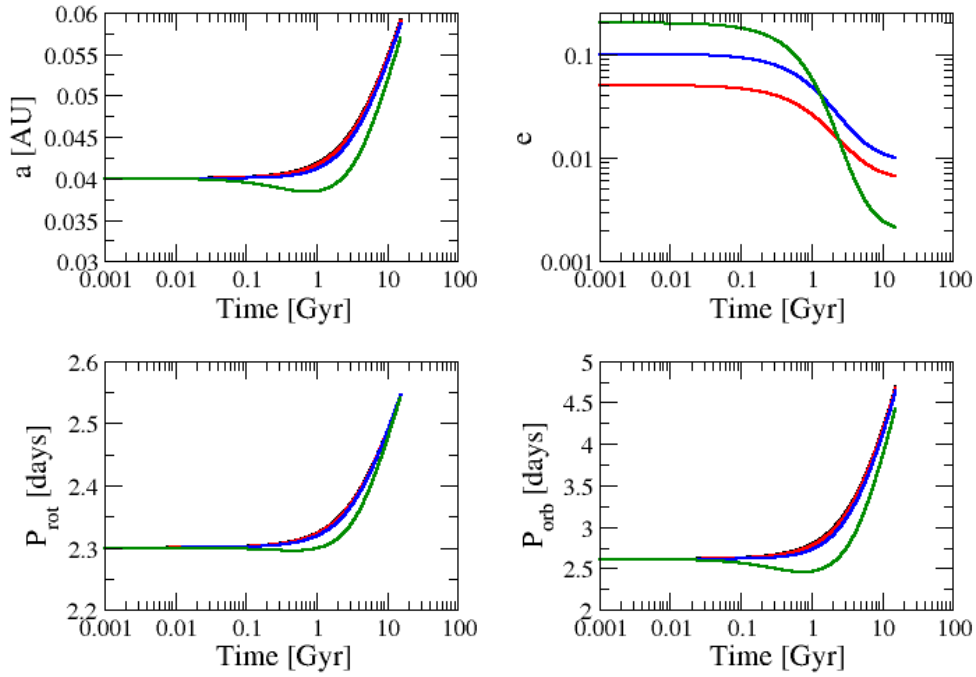


Figure 5.7: Results of the spin-orbit evolution for a close-in Jupiter-like planet around a F6V star with an initial period of $P_{\text{rot}} = 2.3$ days and with $f_P = 0$.

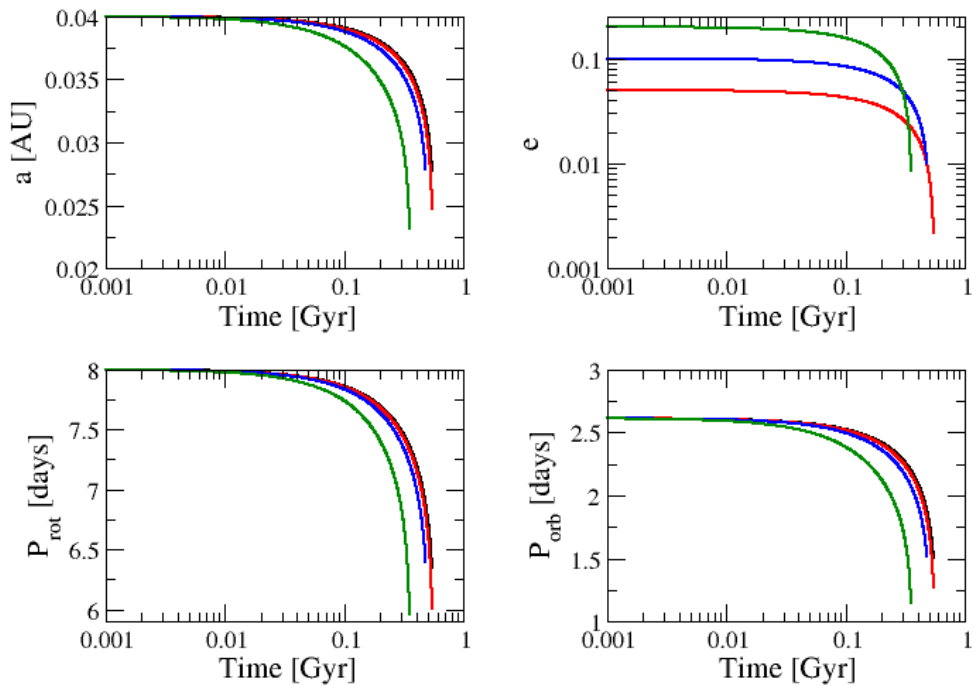


Figure 5.8: Results of the spin-orbit evolution for a close-in Jupiter-like planet around a F6V star with an initial period of $P_{\text{rot}} = 8.0$ days and with $f_P = 0$.

is larger than the mean motion. The semi-major axis increases from the beginning of the simulations for three of the four cases presented in Fig. 5.7. For the case corresponding to

the largest initial eccentricity value, however (see green curves in the figure), the planetary tides cause a significant effect on the orbital evolution process and lead to a subtle semi-major axis decay in the early stages of the orbital evolution process. However, after approximately 1 Gyr of evolution, the orbit expands as in the other three cases. After approximately 10 Gyr of evolution, the orbital period increases by a factor of 2 with respect to the initial value. The results indicate that the orbital expansion process continues to take place even after the 10 Gyr of evolution shown in the figure.

For the results regarding the initially slow-rotating star, we can see that the planet is engulfed by the star in all the cases presented. Indeed, the initial stellar rotation is slow enough to cause tidal decay of the planet. Thus, we expect the planet engulfment to take place even though the magnetic wind braking effect is not considered in the simulations. As it was verified for the other stars, when the semi-major axis decreases, the stellar rotation rate increases due to an enhancement in the tidal torque, which causes an angular momentum transference from the orbit to the stellar spin.

5.2.5 Evolution results for a late F IV (subgiant) star

The parameters of the late F IV star case are based on the data of CoRoT-21 and the study performed by Pätzold et al. (2012). For such star, the magnetic wind braking law cannot be neglected. However, it should have a less important effect on the rotation rate evolution due to the stellar type (i.e. a late F subgiant star).

The results for the initially fast rotator case are presented in Fig. 5.9. Differently from the initially fast-rotating case for the F6V star, we can see that the semi-major axis increase is only temporary. Indeed, orbital expansion takes place for approximately 0.8 Gyr. Afterwards, the magnetic wind braking effect slows down the stellar rotation and causes the orbital decay of the planet. An interesting aspect to be regarded is the final value of the stellar rotation period after planetary engulfment takes place. Since the late F IV star has significantly larger radius and mass values, the rotational angular momentum increase caused by the planet orbital decay is not sufficient to increase the rotation rate of the star as much as for the other stars.

The results for the initially slow rotator are presented in Fig. 5.10. The phenomenological description of the results is practically the same when compared to the results reported for the M, K and G stars. Since the stellar rotation rate is slow from the begin-

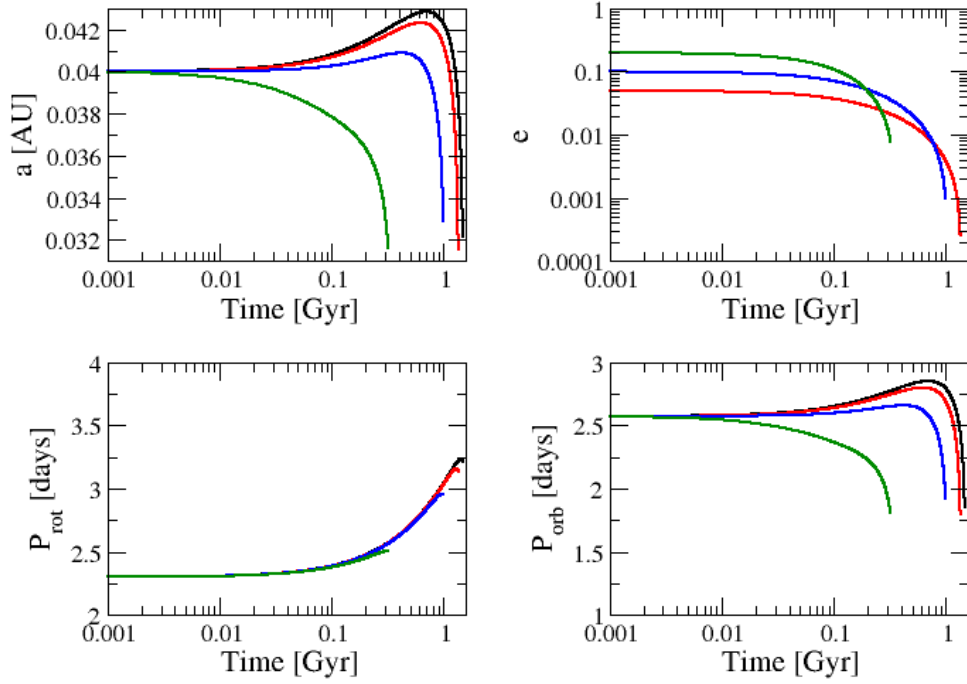


Figure 5.9: Results of the spin-orbit evolution for a close-in Jupiter-like planet around a late F IV star with an initial period of $P_{\text{rot}} = 2.3$ days.

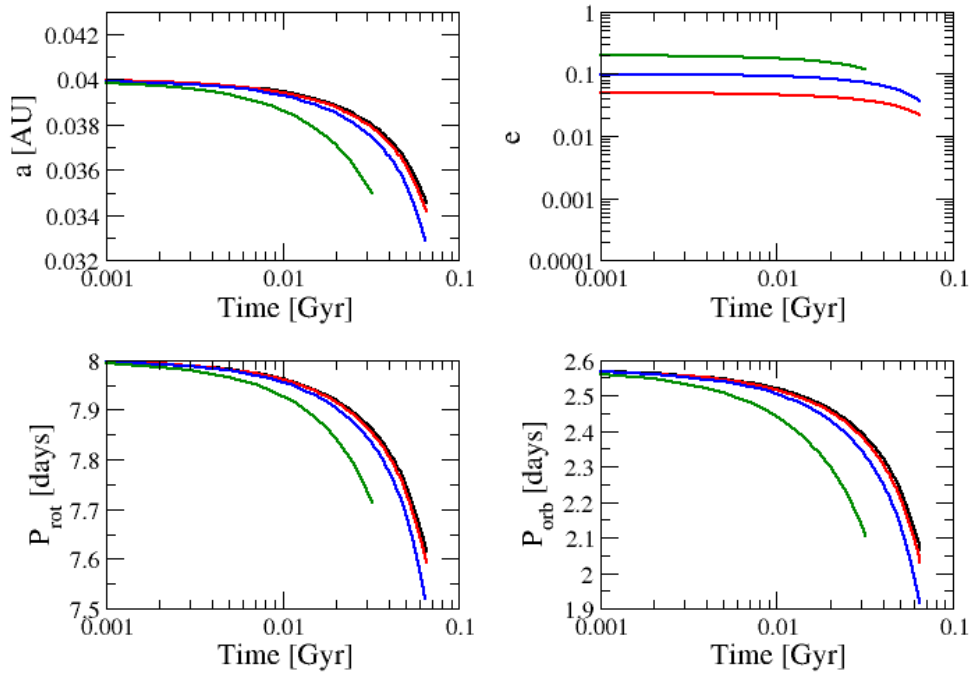


Figure 5.10: Results of the spin-orbit evolution for a close-in Jupiter-like planet around a late F IV star with an initial period of $P_{\text{rot}} = 8.0$ days.

ning of the simulation, we do not detect orbital expansion and the planet falls into the star monotonically (i.e., we always have $da/dt < 0$).

5.2.6 Comparison to Kepler exoplanetary systems

In this subsection, we analyse the evolution of the orbital and the stellar rotational period for the M, K, G and F stars, for the cases considered in the previous subsections. We compare the resulting evolution tracks on the $P_{\text{rot}} \times P_{\text{orb}}$ diagram with the data published by McQuillan et al. (2013) related to the exoplanets discovered in the Kepler mission.

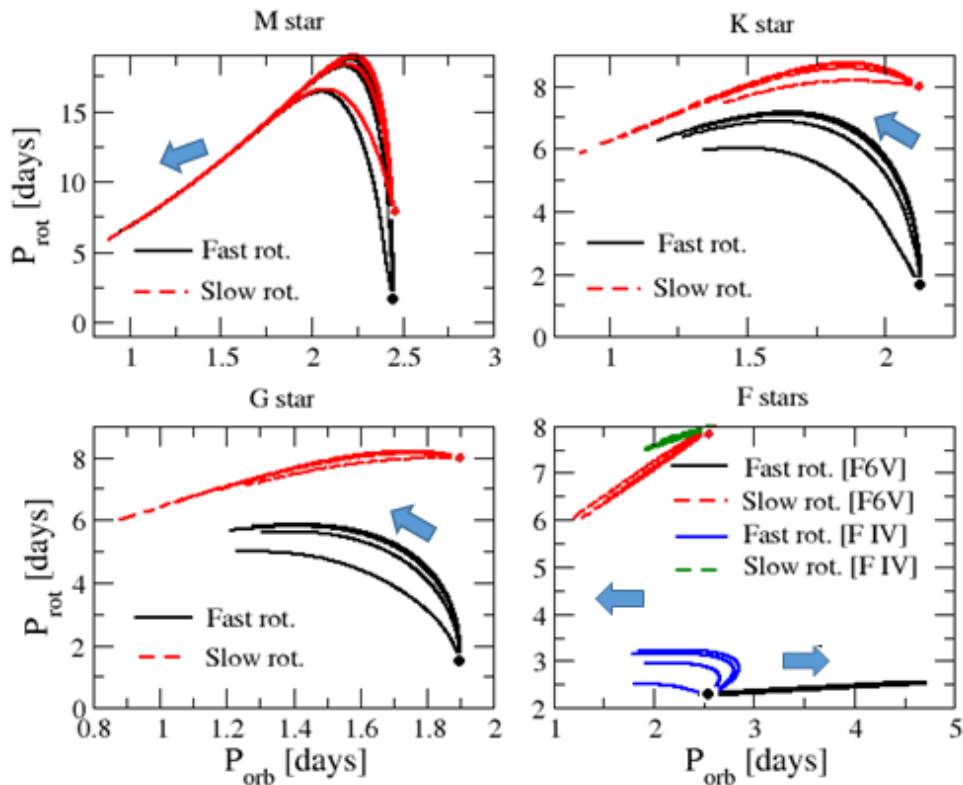


Figure 5.11: Evolution of the stellar rotation and orbital periods for the M (top left), K (top right), G (bottom left) and F (bottom right) stars (where both the F6 and late F IV stars were considered, with F6 star results in the black/red curves and the late F IV star results in the green/blue curves). The arrows indicate the direction of the time evolution along the period diagrams. Moreover, the dots show the initial values used in the simulations.

The periods evolution is presented in Fig. 5.11. Each plot corresponds to a different star (see more details in the caption of the figure). We can see that, for all the cases, the curves do not reach the region of the periods diagram corresponding to $P_{\text{orb}} \leq 1.5$ days and $P_{\text{rot}} \leq 5.0$ days. Such gap has already been verified among KOI, as shown in Fig. 5.12 (extracted from McQuillan et al. 2013). Teitler and Königl (2014) have discussed that such feature can be attributed to the tidal ingestion of close-in exoplanets. Thus, our results regarding such feature are in agreement with the observational data displayed in

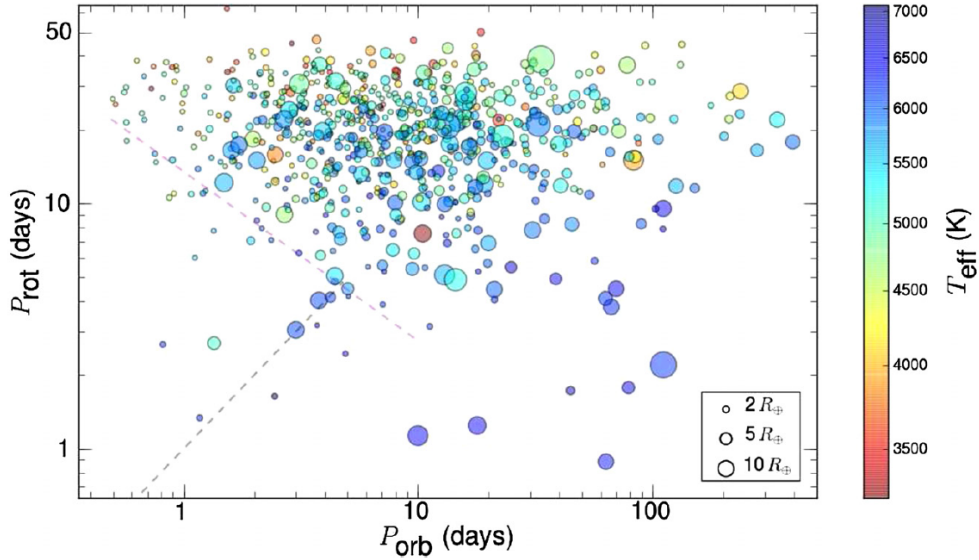


Figure 5.12: Scatter plot of the KOIs in the period diagram, taken from McQuillan et al. (2013). The size of the dots indicate the size of the radius of the planet, while the colours refer to the stellar effective temperature.

McQuillan et al. (2013).

In what concerns the relatively large population of exoplanets in the upper left region of the periods diagram (see Fig. 5.12), we can see that the major part of the exoplanets are either super-Earths or mini-Neptunes. This is consistent with the fact that the stellar tide is weaker for lower mass planetary companions. In such specific case, the planets can survive for some Gyr even though the stellar rotation period is of the order 30 – 40 days and the orbital period is of the order 0.5 – 2 days.

The last aspect which we would like to comment regarding the comparison of our theoretical results with the observational periods diagram is the presence of some massive planets in the region corresponding to $P_{\text{orb}} = 3 - 10$ days and $P_{\text{rot}} = 3 - 5$ days and stars with effective temperature of the order 6000 K (i.e., F stars). Such planets could indeed have been formed with smaller semi-major axis values and then migrated due to tidal interactions to the present configuration, provided that the initial stellar rotation was relatively fast (of the order 2.3 days of rotation period) and that magnetic wind braking interactions were absent. Some possible evolutionary tracks of the periods corresponding to these cases can be seen in Fig. 5.11, bottom right panel.

5.3 Survival timescale of hot Jupiters for M, K and G stars

In the previous section, we have presented several evolution scenarios for hot Jupiters around M, K, G and F stars. We have noted that, when taking into account both tidal interactions as well as the magnetic wind braking of the stellar rotation, the consequences for orbital evolution for the M, K and G stars are the same at the end of the simulations: the planet falls into the star. The only differences among the simulations we performed are minor details (such as the temporary orbital expansion process in the earlier stage of orbital evolution, which takes place for the case of the initially fast-rotating late F IV star with $f_P = 0.1$). Indeed, the relatively short timescales of survival of close-in massive exoplanets has been extensively discussed in other works (see e.g., discussions presented mainly in Penev et al. 2012, 2014 and references therein). The analysis of survival timescales of short-period exoplanets has been used as a criterion to evaluate the maximum tidal dissipation rates in stars in order to prevent planet engulfment, thus providing a calibration method for the tidal dissipation rate in host stars and their planets (see discussions in e.g., Hansen 2010, 2012)¹.

5.3.1 Dependence on the relaxation factor and eccentricity

In this section, we will investigate the dependence of the survival timescale (hereafter τ_{surv}) as a function of the relaxation factor. Since we have observed, in the previous section, that increasing the eccentricity causes a decrease in τ_{surv} , we will explore τ_{surv} - γ relationships for different eccentricity values. We consider stars with stellar parameters given in the first, second and third rows of Table 5.1. For the initial rotation rate of the stars, we considered the initially slow rotator with $P_{\text{rot}} = 8$ days. The planetary relaxation factor was fixed at $\gamma_p = 50 \text{ s}^{-1}$ (see Ferraz-Mello 2013, Table 1) and the stellar relaxation factor was varied between 10 s^{-1} and 50 s^{-1} .

The results of our simulations are shown in Fig. 5.13. The left panel shows the results for the M star, the middle panel shows the results for the K star and the right panel shows the results for the G star. We can see that the survival timescale follows a linear relationship on the relaxation factor value for both the circular and eccentric case. However, for the

¹ Indeed, the equations given by Hansen (2010) have been used by Ferraz-Mello (2013) to estimate the relaxation factor of Solar type stars as well as hot Jupiters (see Sects. 9.9 and 9.11 of Ferraz-Mello 2013).

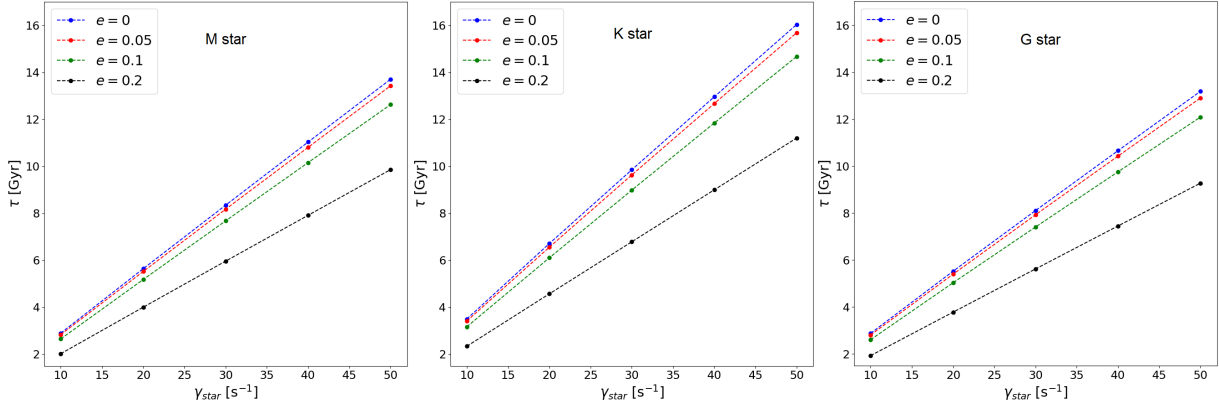


Figure 5.13: Survival timescales as a function of the stellar relaxation factor for M, K and G stars on the left, middle and right panels, respectively. Different colours of the dots represent different eccentricity values, as it is shown in the labels. For the M star, we considered $a = 0.03$ AU (corresponding to $P_{\text{orb}} = 2.44$ days), while for the K and G stars we considered $a = 0.04$ AU (corresponding to $P_{\text{orb}} = 3.25$ days for the K star and $P_{\text{orb}} = 2.91$ days for the G star).

eccentric case, the slope of the resulting linear fit of $\tau_{\text{surv}} = a\gamma_{\star} + b$ is smaller. As a working example, we provide in Table 5.2 the corresponding linear fit coefficients for the G star, for the four eccentricity values used in the simulations on the right panel of Fig. 5.13.

We can see that the difference between the values of the angular coefficients is small when comparing the circular and less eccentric case (see values of a in the first and second rows of Table 5.2). However, when we compare the values of the angular coefficients for the circular and most eccentric case (i.e., the first and fourth rows of Table 5.2), the difference between the coefficients is approximately 30% of the absolute value of the angular coefficient.

Indeed, the difference in the slope of the $\tau_{\text{surv}} - \gamma_{\star}$ curves offers an important interpretation of the results. Let us suppose that a given exoplanetary system has an age of 5 Gyr. Assuming that the evolution of the stellar mass and radius values can be neglected and that no planet-disk interactions took place during the past 5 Gyr, the main mechanism ruling orbital evolution is the tidal interaction between the star and the planet. Thus, taking into account that the planet survived the past 5 Gyr of the orbital evolution process without falling into the star, it ensues that γ_{\star} must be such that $\tau_{\text{surv}} > 5$ Gyr. If we do not have any information on the current eccentricity of the planet, we may assume that the initial eccentricity of the planet could have been either 0 or values such as 0.2 (or larger values). Using the values of a and b of Table 5.2, we then obtain that $\gamma_{\star} \geq 18 \text{ s}^{-1}$ for the

circular case and $\gamma_\star \geq 27 \text{ s}^{-1}$ for the eccentric case with $e = 0.2$. Thus, γ_\star varies 50% if we consider the uncertainty in the initial value of the eccentricity.

Table 5.2 - Angular and linear coefficients (a and b , respectively) of the function $\tau_{\text{surv}} = a\gamma_\star + b$ for the G star case, corresponding to the simulations shown in the bottom panel of Fig. 5.13.

Eccentricity	a	b
0	0.2573	0.3522
0.05	0.2519	0.3336
0.1	0.2366	0.2791
0.2	0.1834	0.1089

The difference in the minimum value found for γ_\star considering different eccentricity values is worth discussing. In Penev et al. (2018), for instance, the authors discuss the possible values of the dissipation factor (namely, Q) for several exoplanetary systems, using the criterion of planet survival timescales. In such work, the uncertainty in the determination of the values of Q arise from the propagation of the uncertainty in the observational parameters. However, the authors consider that the orbital eccentricity is zero from the beginning of the simulation. As we have seen with the simple example discussed in this section, the uncertainty in the estimation of γ (which is linked to Q through an empirical formula, see Ferraz-Mello 2013) arising from the consideration of non-circular orbits can be of the order 50% (or even larger values if we consider an eccentricity value larger than 0.2), that is, if we consider a smaller relaxation factor and a smaller eccentricity, we find a similar value for τ_{surv} than if we consider a larger initial eccentricity value and a larger value for the relaxation factor. Thus, such results encourage the consideration of different values for the initial eccentricity of the system when performing studies related to the calibration of the dissipation factor on exoplanets and their host stars.

5.3.2 Discussions regarding the estimations of Penev et al. (2018)

In the previous subsection, we were able to conclude that (i) τ_{surv} is proportional to the relaxation factor γ_\star and (ii) the role of the initial eccentricity value is to decrease

τ_{surv} . We proposed that the initial eccentricity value is thus an important parameter in what concerns the estimation of the dissipation factor of exoplanetary systems. In another words, we can have two simulations with different values for e_0 and γ_* which lead to the same value of τ_{surv} . Thus, the initial eccentricity value can be a parameter to explore the uncertainties in the value of γ_* for known exoplanetary systems.

In a recent work, Penev et al. (2018) have analyzed a sample of 188 known HJs with an orbital period < 3.5 days and a relatively low temperature host star ($T_{\text{eff}} < 6100$ K). In such work, the authors provided constraints on the value of the stellar dissipation rate for which the current stellar spin period and semi-major axis could be obtained. For such purposes, all the observational uncertainties were taken into account.

We used the (empirical) equation linking the Q factor to the relaxation factor provided in Ferraz-Mello et al. (2020), namely

$$\gamma_* = \nu_* k_2 Q'_*, \quad (5.2)$$

to obtain the corresponding estimations of the stellar relaxation factor value for several systems presented in Penev et al. (2018). We focused our analysis on exoplanetary systems for which Q could be constrained with both an upper and a lower uncertainty limiting value.

The results in Fig. 5.14 show that the relaxation factor corresponding to the Q value determined in Penev et al. (2018) varies widely among the considered exoplanetary systems. Indeed, a simple calculation of the mean value of the relaxation factor considering the points in Fig. 5.14 leads to $\langle \gamma \rangle_* = 134 \text{ s}^{-1}$. However, we can detect some outliers among the systems (i.e., stars with relaxation factor values much larger than the mean value). For instance, WASP-43, HATS-18 and HAT-P-36 have relaxation factor values that significantly deviate from the mean value. Thus, comparing the estimations of Penev et al. (2018) with our predictions that the eccentricity value can change the determined value of γ by 50% allows us to conclude that the errors in the observational parameters are indeed much more important than the consideration of an initially non-circular orbit. The dependence of Q (or γ) on the initial eccentricity value is only worth being discussed in the cases where (i) the stellar rotation rate is determined with an uncertainty of the order 2 – 3 days and (ii) the stellar physical parameters are determined with an uncertainty of the order 10% of the absolute value.

Finally, we point out two important aspects regarding the results for γ_* presented in

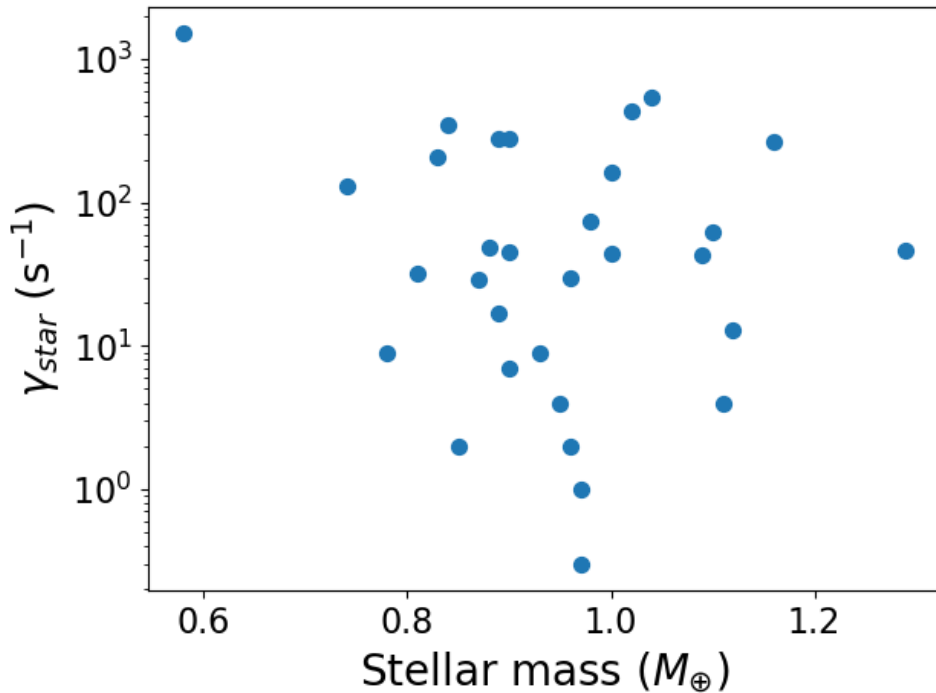


Figure 5.14: Scatter plot of the relaxation factor values corresponding to the Q value determined in Penev et al. (2018), as a function of the stellar mass, for the dataset provided in Penev et al. (2018). The sample contains the 35 exoplanetary systems for which an upper and a lower boundary value were determined for the quality factor.

this section. Firstly, the relaxation factor varies between approximately $1 - 10^2$ s $^{-1}$. There is only one outlier in Fig. 5.14, for which $\gamma_{\star} > 10^3$ s $^{-1}$. Secondly, the determination of γ_{\star} was performed assuming the equation linking Q and γ given in Ferraz-Mello et al. (2020). However, in the original work of Penev et al. (2018), the authors modeled tidal interactions supposing the CPL (Constant Phase Lag) hypothesis. Indeed, such a model is only applicable in the specific case where the mean motion and the stellar rotation do not vary very much (thus leading to a constant value of ν in Eq. 5.2). For long-term spin-orbit evolution studies, the tidal frequency varies significantly and thus, the Q factor varies. If we suppose, however, that Q is time independent (as it is the case of the CPL approach), it results from Eq. (5.2) that γ must vary to keep Q constant. However, γ is a constant and varies only if the physical parameters of the star change. Its value is independent of the tidal frequency. Thus, these results for the stellar relaxation factor should not be used in spin-orbit evolutionary studies of exoplanetary systems before a more detailed analysis using a more universal theory as the creep tide theory or Darwin’s CTL theory is

performed. In fact, for some exoplanetary systems, for instance, the WASP-4, it has been discussed that the stellar Q'_* is significantly different from the value estimated by Penev et al. (2018), given by $Q'_* = (4.5 - 8.5) \times 10^4$ (see e.g., Bouma et al. 2019, Baluev et al. 2020). The estimation of Baluev et al. (2020) was performed based on the hypothesis that recently measured TTVs for WASP-4 b are induced by stellar tidal interactions. In such case, we would have γ_* of the order 1 s^{-1} .

Tidal evolution of exoplanetary systems hosting potentially habitable exoplanets. The cases of LHS-1140 b-c and K2-18 b-c

The following article addresses an implementation of the creep tide theory to study the spin-orbit evolution of two secularly-evolving exoplanetary systems containing potentially habitable exoplanets (hereafter PHEs): the LHS-1140 b-c (Dittmann et al., 2017; Ment et al., 2019) and K2-18 b-c (Montet et al., 2015; Cloutier et al., 2019) systems. To take tidal interactions into account for the spin-orbit evolution, we mix the first version of the creep tide theory (Ferraz-Mello, 2015) with the version of Folonier et al. (2018) in the following way: when the rotation rate is not trapped in the synchronism, we employ the constant rotation rate solutions for the shape and orientation of the tidal bulge of the body, which lead to the spin-orbit evolution equations of Ferraz-Mello (2015). For the synchronous rotation rate case, we employ the analytical solutions for the shape and orientation of the tidal bulge presented in Folonier et al. (2018). Finally, to take into account the secular interactions due to the gravitational perturbations between the planets, we employ the model of Mardling and Lin (2002). We explore the consequences of tuning the relaxation factor of the planets on their orbital evolution. The results of this study allow us to propose a criterion to estimate the relaxation factor of the planets based on the outcomes of orbital evolution of the systems.

For the LHS-1140 b-c exoplanetary system, the results of the study presented in the paper allow us to conclude that the planets are probably in nearly-circular orbits, provided that the value of the relaxation factor of the inner planet is close to the value estimated for the solid Earth, which is $0.9 \times 10^{-7} \text{ s}^{-1} \leq \gamma_{\text{Earth}} \leq 3.6 \times 10^{-7} \text{ s}^{-1}$ (for more details,

see estimations of the relaxation factor for the solid Earth presented in Table 1 of Ferraz-Mello 2013 and discussions therein). Since the eccentricities of the planets are not well constrained from observations, we cannot rule out the possibility that the planets are in eccentric orbits. If future data analysis of radial velocity and transit data indicate high eccentricity values for the planets (such as eccentricities of the order 0.1 – 0.2), the planets relaxation factor values are more likely to be either (i) much smaller than the value estimated for the Earth or (ii) much larger than the value of the Earth, in which case the viscosity of the planets would be closer to the values estimated for gaseous planets such as Neptune and Jupiter.

For the K2-18 b-c exoplanetary system, the current lack of knowledge of the planetary radius and mass value of the inner planet led us to perform an analysis of the scenarios of orbital evolution considering two cases: a rocky Earth-like K2-18 c (hereafter case 1) and a gaseous K2-18 c (hereafter case 2). Combining the analysis of the results considering cases 1 and 2 as well as the estimation of the eccentricity of K2-18 b (namely, $e_b = 0.20 \pm 0.08$, see Sarkis et al. 2018), we conclude that the inner planet cannot have a relaxation factor value which is close to the value of the Earth. If this was the case, the timescale of eccentricity evolution of the inner planet would be very small, and the eccentricity coupling of the planets due to the secular gravitational interactions would cause the eccentricity of the outer planet to decrease to values much smaller than the estimations of Sarkis et al. (2018) considering a timescale of some Gyr for the orbital evolution of the system. Thus, to conciliate the current eccentricity estimation of K2-18 b with the relaxation factor value of the inner planet, we need to have two specific regimes of values for γ_c . Either γ_c is very small, of the order 10^{-10} s^{-1} (which is a value typical of very rocky bodies with larger viscosities than a super-Earth, like Mercury), or γ_c is very large, of the order $1 - 10 \text{ s}^{-1}$. In this case, the planet would be classified as a mini-Neptune. In summary, γ_c cannot be of the order $10^{-7} - 10^{-8} \text{ s}^{-1}$, which is a value typical of super-Earths.

Tidal evolution of exoplanetary systems hosting potentially habitable exoplanets. The cases of LHS-1140 b-c and K2-18 b-c

G. O. Gomes^{1,2}★ and S. Ferraz-Mello¹

¹*Instituto de Astronomia, Geofísica e Ciências Atmosféricas, IAG-USP, Rua do Matão 1226, 05508-900 São Paulo, Brazil*

²*Observatoire de Genève, Université de Genève, 51 Chemin des Maillettes, CH-1290 Sauverny, Switzerland*

Accepted 2020 April 19. Received 2020 April 19; in original form 2020 March 4

ABSTRACT

We present a model to study secularly and tidally evolving three-body systems composed by two low-mass planets orbiting a star, in the case where the bodies rotation axes are always perpendicular to the orbital plane. The tidal theory allows us to study the spin and orbit evolution of both stiff Earth-like planets and predominantly gaseous Neptune-like planets. The model is applied to study two recently discovered exoplanetary systems containing potentially habitable exoplanets (PHE): LHS-1140 b-c and K2-18 b-c. For the former system, we show that both LHS-1140 b and c must be in nearly circular orbits. For K2-18 b-c, the combined analysis of orbital evolution time-scales with the current eccentricity estimation of K2-18 b allows us to conclude that the inner planet (K2-18 c) must be a Neptune-like gaseous body. Only this would allow for the eccentricity of K2-18 b to be in the range of values estimated in recent works ($e = 0.20 \pm 0.08$), provided that the uniform viscosity coefficient of K2-18 b is greater than 2.4×10^{19} Pa s (which is a value characteristic of stiff bodies) and supposing that such system has an age of some Gyr.

Key words: celestial mechanics – planets and satellites: general.

1 INTRODUCTION

After the discovery of the first exoplanet orbiting a solar-type star in 1995 (Mayor & Queloz 1995), a new research branch in astronomy related to the detection and characterization of exoplanetary systems ensued. Several projects have been developed with the aim of discovering exoplanets. On the one hand, missions based on the transit photometry technique (e.g. *Kepler*, *TESS*, and *WASP*) allow for a determination of the radii of exoplanets by using space or ground telescopes. On the other hand, high-precision spectrographs (e.g. HARPS, HARPS-N, ESPRESSO, and HIRES) are used to estimate the masses of exoplanets by the method of Doppler spectroscopy (a.k.a radial velocity measurements). The combination of the data from Doppler spectroscopy measurements and transits thus allows for the estimation of exoplanets densities and bulk compositions. The diversity of masses and radii of the exoplanets discovered from these missions allows for the characterization of such bodies to vary between small Earth-like rocky planets or waterworlds to hot Jupiters and brown dwarfs (see e.g. Kuchner 2003; Léger et al. 2004, references therein). Taking into account such diversity of the exoplanets compositions, several models have been developed with the objective of modelling their interior structure (Seager et al. 2007; Adams, Seager & Elkins-Tanton 2008; Batygin & Stevenson 2013). Tidal interactions and their resulting consequences for orbital

evolution have been studied for both exoplanets (Barnes 2017; Barr et al. 2018) and their host stars (Bolmont et al. 2012) in order to determine the fate of potentially habitable exoplanets (henceforth PHE) w.r.t their position in the habitable zone (henceforth HZ) of their host stars.

Barnes (2017) has shown that the tidal locking is a major factor in the orbital evolution of PHE, and rotational synchronization may be a characteristic of the majority of these planets. The results presented by Barnes were based on simulations of the coupled spin-orbit tidal evolution of exoplanetary systems, where the Constant Time Lag (CTL) and Constant Phase Lag (CPL) Darwinian approaches were employed.

In parallel works, Bolmont et al. (2017) and Gallet et al. (2017) studied the effects of stellar tidal dissipation on the evolution of close-in massive planets. Their results show that the dynamical tide (i.e. the tidal interactions arising as a consequence of the excitation of inertia waves in the interior of the stars) may be the dominant effect on the orbital evolution of the exoplanetary systems in the pre-main sequence (PMS), whereas the equilibrium tide (i.e. the large-scale hydrodynamic adjustment of a body and the resulting flow as a consequence of the gravitational field of a companion) rules the orbital evolution when the star reaches the zero age main sequence (ZAMS) and evolves until the red giant branch (RGB) phase.

In most of the aforementioned works related to the study of tidal interactions and the subsequent orbital evolution of exoplanetary systems, Darwinian approaches have been employed to compute the effects of the equilibrium tides in both the exoplanets and their

* E-mail: gabrielogomes@usp.br

host stars. Such approaches require the knowledge of the tide lag, which is related to the quality factor (Q) ruling the energy dissipated by the bodies, and varies significantly among predominantly rocky Earth-like planets and gaseous bodies such as hot Jupiters and host stars (Dobbs-Dixon et al. 2004; Kellermann et al. 2018). Moreover, the quality factor is an ad hoc parameter that has not been rigorously linked to the internal structure and physical parameters of the bodies, as a consequence of the lack of a thorough knowledge of the dominant physical processes determining the magnitude of the dissipation factor responsible for the tidal evolution of planetary systems (Dobbs-Dixon et al. 2004).

Recently, a new theory to model tidal interactions among celestial bodies was developed by Ferraz-Mello (2013). This theory (hereafter referred to as the creep tide theory) considers the deformations of an extended body due to the perturbation caused by the existence of a point mass companion. In this framework, the non-instantaneous response of the extended body's figure to the disturbing potential caused by the point mass and the rotation of the primary is ruled by the relaxation factor γ , which is inversely proportional to the uniform viscosity coefficient η of the extended body. The resulting expressions for both the rotational and orbital evolution of the system depend on well-defined physical parameters. No ad hoc constants ensue relating the tidal lags to the frequencies. Moreover, the phenomenon of capture in spin-orbit resonances may be described without the additional hypothesis of a permanent equatorial asymmetry.

In 2018, a new version of the creep tide theory was developed by Folonier et al. In this new version, the resulting equilibrium figure of the extended body is assumed to be an ellipsoid with unknown flattenings and orientation. The time evolution of the extended body's figure is obtained by the simultaneous integration of three first-order ordinary differential equations. The expression for the potential resulting from the deformations of the extended body is used to obtain the equations that rule the orbital evolution of the system and the rotational evolution of the extended body (Folonier et al. 2018), by employing the basic principles of Newtonian mechanics. The old version of the creep tide theory (Ferraz-Mello 2013) predicted small-amplitude forced oscillations of the rotation in the case of stiff bodies in synchronous motions. The new version of the theory (Folonier et al. 2018) takes them into account in a self-consistent way.

In this work, we describe a model to study the orbital and rotational evolution of three-body secularly evolving exoplanetary systems composed by a star and two low-mass planetary companions, such as super-Earths and mini-Neptunes. The model is only valid for the coplanar case, where all the bodies rotation axes are perpendicular to the orbital plane at each instant. Both tidal and secular planetary interactions are considered in the model. Tidal interactions are taken into account by employing the creep tide theory (Ferraz-Mello 2013; Folonier et al. 2018), while the secular interactions between the planets are computed by using the models of Mardling & Lin (2002) and Mardling (2007). The model is applied to two exoplanetary systems, namely K2-18 b-c and LHS-1140 b-c, where the choice of these systems for study is based on the possible existence of a PHE in each system (namely, K2-18 b and LHS-1140 b). In both cases, the mean motion ratio of the planets indicates that no mean motion resonances influence the dynamics of the system. For the specific case of the K2-18 b-c exoplanetary system, the lack of an estimation of the radius of K2-18 c indicates that both the cases of a rocky super-Earth and a gaseous mini-Neptune compositions must be considered to study the tidal evolution of this system.

The models describing tidal and secular interactions are presented in Section 2, where only the main aspects of the theories, which are required to obtain the equations ruling the spin-orbit evolution of the system, are outlined. In Section 3, we briefly introduce the discoveries related to the LHS-1140 b-c system and apply the theory to study the evolution of the system. The application to the K2-18 b-c system is performed in Section 4. The discussions and conclusion of the work are presented in Section 5.

2 MODEL DESCRIPTION

In this section, we present the tidal and secular evolution models used to obtain the equations ruling the time evolution of the exoplanetary systems. The models employed in this work were already presented in other papers. Thus, we only present the main points of their theoretical formulation. For a more detailed description, the reader is referred to Folonier et al. (2018) for the tidal interactions model and Mardling (2007) for the secular interactions model.

2.1 Tidal interactions

We consider an extended body of mass m (primary) and a point mass M (companion) whose instantaneous distance to the primary is $r(t)$. We comment that, in actual applications of the model, both the star and the planets may play the role of the primary.

The primary is assumed to rotate with an angular velocity Ω pointing in the z -direction, perpendicular to the orbital plane. The creep tide theory assumes a first-order linear differential equation for the instantaneous surface figure ζ of the primary. This equation is an approximate solution of the Navier–Stokes equation in spherical coordinates, supposing a low-Reynolds-number flow. The equation reads (Ferraz-Mello 2013, 2019)

$$\dot{\zeta} = \gamma(\rho - \zeta), \quad (1)$$

where γ is the relaxation factor given by

$$\gamma = \frac{Rgd}{2\eta}, \quad (2)$$

with R , g , d , and η being the mean radius, surface gravity, mean density, and uniform viscosity coefficient of the primary and ρ is the surface figure of the primary corresponding to the inviscid case (a.k.a static tide). Supposing that the resulting surface figure can be approximated by a triaxial ellipsoid rotated of an angle δ w.r.t the companion, we obtain a system of differential equations ruling the figure evolution of the primary, given by (Folonier et al. 2018)

$$\dot{\delta} = \Omega - \dot{\varphi} - \frac{\gamma\epsilon_\rho}{2\mathcal{E}_\rho} \sin 2\delta, \quad (3)$$

$$\dot{\mathcal{E}}_\rho = \gamma (\epsilon_\rho \cos 2\delta - \mathcal{E}_\rho), \quad (4)$$

$$\dot{\mathcal{E}}_z = \gamma (\epsilon_z - \mathcal{E}_z), \quad (5)$$

where \mathcal{E}_ρ and \mathcal{E}_z are the ellipsoid instantaneous equatorial and polar flattening coefficients, respectively, φ is the true anomaly of the companion and ϵ_ρ , ϵ_z are the flattenings in the inviscid case. They are given by

$$\epsilon_\rho = \frac{15}{4} \frac{M}{m} \frac{R^3}{r^3} \equiv \bar{\epsilon}_\rho \left(\frac{a}{r}\right)^3, \quad (6)$$

$$\epsilon_z = \frac{\epsilon_\rho}{2} + \bar{\epsilon}_z = \frac{\epsilon_\rho}{2} + \frac{5\Omega^2 R^3}{4Gm}, \quad (7)$$

where G is the gravitational constant. It is worth emphasizing that the assumption that the resulting equilibrium figure can be represented by a triaxial ellipsoid is an approximation. Such approximation is reasonable in the applications of this work since the planets are relatively far from their host star. However, such approximation may not be valid in the case of close-in planets subjected to large tidal distortions (see e.g. the discussions presented in Hellard et al. 2019).

The expression for the potential acting on the companion considering the resulting triaxial shape of the primary rotated of an angle $\varphi_B = \varphi + \delta$ w.r.t the axis x can be approximated, to first order in the flattenings, by

$$MU = -\frac{GMm}{r} - \frac{3GCM}{4r^3} \left[\mathcal{E}_\rho \cos(2\varphi_B - 2\varphi) + \frac{2}{3}\mathcal{E}_z \right], \quad (8)$$

where C is the moment of inertia of the primary.

Since we have the expression for the potential, we can calculate the components of the force acting on the companion (\vec{F}). Moreover, from the force expression, the torque can be obtained. The reaction to the torque acting on the companion is the torque ruling the rotational evolution of the primary, while the expressions for the derivative of the work done by the disturbing tidal potential ($\dot{W} = \vec{F} \cdot \vec{V}$, with \vec{V} being the velocity of the companion) and the angular momentum variation ($\dot{\mathcal{L}}$) of the orbit give the equations ruling the semimajor axis and eccentricity evolution. The calculations are straightforward and we obtain

$$\dot{\Omega} = -\frac{3GM}{2r^3} \mathcal{E}_\rho \sin 2\delta, \quad (9)$$

$$\dot{a} = \frac{2a^2}{GMm} \dot{W}, \quad (10)$$

$$\dot{e} = \frac{1-e^2}{e} \left(\frac{\dot{a}}{2a} - \frac{\dot{\mathcal{L}}}{\mathcal{L}} \right). \quad (11)$$

Equations (9)–(11) must be solved simultaneously with equations (3)–(5) to give the complete tidal evolution of the system. This method is henceforth referred to as full approach. We have six first-order ordinary differential equations to be solved. The number of differential equations to be solved can be reduced if we consider the constant rotation rate approximation. In this case, Ω is assumed to be a constant when solving for equations (3)–(5). Afterwards, the equation for $\dot{\Omega}$ is obtained from the torque expression. This approach is henceforth referred to as constant rotation rate approximation. In this case, the formulation is strictly equivalent to the previous version of the creep tide theory (Ferraz-Mello 2013, 2015) and virtually equivalent to the approach of Correia et al. (2014), which is based on a Maxwell viscoelastic rheology.

2.1.1 Constant rotation rate approximation

We now briefly mention some results of the constant rotation rate approximation.

Considering that the short-period variations of the rotation rate are negligible in equation (3) (which is a reasonable assumption for a body far from the synchronous rotation regime), we can obtain a series expression for the differential equations ruling the orbital evolution of the system and the rotational evolution of the primary (Gomes et al. 2019). The calculations are straightforward and the results are the same as the ones presented in Ferraz-Mello (2015). We have

$$\langle \dot{a} \rangle = \frac{R^2 n \bar{\epsilon}_\rho}{5a} \sum_{k \in \mathbb{Z}} \left[3(2-k) \frac{\gamma(\nu + kn) E_{2,k}^2}{\gamma^2 + (\nu + kn)^2} - \frac{\gamma k^2 n E_{0,k}^2}{\gamma^2 + k^2 n^2} \right], \quad (12)$$

$$\langle \dot{e} \rangle = -\frac{3GMR^2 \bar{\epsilon}_\rho}{10na^5 e} \sum_{k \in \mathbb{Z}} \left[P_k^{(1)} \frac{\gamma(\nu + kn) E_{2,k}^2}{\gamma^2 + (\nu + kn)^2} + \frac{P_k^{(2)}}{3} \frac{\gamma k^2 n E_{0,k}^2}{\gamma^2 + k^2 n^2} \right], \quad (13)$$

$$\langle \dot{\Omega} \rangle = -\frac{3GM \bar{\epsilon}_\rho}{2a^3} \sum_{k \in \mathbb{Z}} \frac{\gamma(\nu + kn) E_{2,k}^2}{\gamma^2 + (\nu + kn)^2}, \quad (14)$$

with $\nu = 2\Omega - 2n$ being the semidiurnal frequency. Moreover, we have

$$P_k^{(1)} = \left[2\sqrt{1-e^2} - (2-k)(1-e^2) \right], \quad (15)$$

$$P_k^{(2)} = 1 - e^2, \quad (16)$$

and $E_{j,k}$ are Cayley coefficients, given by (Ferraz-Mello 2013, 2015)

$$E_{2,k}(e) = \frac{1}{2\pi \sqrt{1-e^2}} \int_0^{2\pi} \frac{a}{r} \cos[2\varphi + (k-2)\ell] d\varphi, \quad (17)$$

where ℓ is the mean anomaly of the companion.

The above formulation adopting a constant rotation rate significantly reduces the time required to numerically integrate the equations of the orbital and rotational evolution of the system. The discrepancies between the constant rotation rate approximation and the full approach arise when the rotation is near the synchronous regime, for stiff bodies. An analytical approximation to correctly describe the figure and rotational evolution equations of the extended body in the synchronous rotation regime has already been developed by Folonier et al. (2018), by taking into account the non-negligible short-period variations of the rotation rate. The results are briefly revisited in the next subsection.

2.1.2 The synchronous regime

When the rotation of the extended body is damped to the synchronous (or pseudo-synchronous) attractor, the time evolution of the rotation and the ellipsoid's shape can be described by a sum of periodic components with frequencies kn , where $k \geq 1$ and n is the orbital mean-motion (Folonier et al. 2018). The analytical expressions for Ω , \mathcal{E}_ρ , \mathcal{E}_z , and δ allow for the determination of compact equations ruling the evolution of both the semimajor axis and the eccentricity. The resulting expressions are (to order e^2)

$$\langle \dot{a} \rangle = -\frac{21C\bar{\epsilon}_\rho e^2}{ma} \frac{n^2 \gamma}{n^2 + \gamma^2}, \quad (18)$$

$$\langle \dot{e} \rangle = -\frac{21C\bar{\epsilon}_\rho e(1-e^2)}{2ma^2} \frac{n^2 \gamma}{n^2 + \gamma^2}. \quad (19)$$

2.2 Secular interactions

Additionally to the tidal interactions, the secular interactions between the planets must be taken into account in the case of a star with two planetary companions. For a coplanar system, the secular interactions cause a variation of the planets eccentricity as well as their longitudes of periastron ϖ . The model of Mardling & Lin (2002) gives a system of four differential equations ruling the planets secular evolution. The equations are

$$\dot{e}_1 = -\frac{15}{16} n_1 e_2 \frac{m_2}{m_0} \left(\frac{a_1}{a_2} \right)^4 \frac{\sin \Delta \varpi}{(1-e_2^2)^{5/2}}, \quad (20)$$

$$\dot{e}_2 = \frac{15}{16} n_2 e_1 \frac{m_1}{m_0} \left(\frac{a_1}{a_2} \right)^3 \frac{\sin \Delta \varpi}{(1-e_1^2)^2}, \quad (21)$$

Table 1. Parameters for the LHS-1140 system after Ment et al. (2019). The eccentricity estimations have a 90 per cent confidence.

LHS-1140	Parameter value
Stellar mass (M_{\odot})	0.179 ± 0.014
Stellar radius (R_{\odot})	0.2139 ± 0.0041
Luminosity (L_{\odot})	0.00441 ± 0.00013
Effective temperature (K)	3216 ± 39
Rotation period (d)	131 ± 5
Age (Gyr)	>5
LHS-1140 c	
Planet mass (M_{\oplus})	1.81 ± 0.39
Planet radius (R_{\oplus})	1.282 ± 0.024
Mean density (g cm^{-3})	4.7 ± 1.1
Semimajor axis (au)	0.02675 ± 0.00070
Orbital period (d)	3.777931 ± 0.000003
Orbital eccentricity	<0.31
LHS-1140 b	
Planet mass (M_{\oplus})	6.98 ± 0.89
Planet radius (R_{\oplus})	1.727 ± 0.032
Mean density (g cm^{-3})	7.5 ± 1.0
Semimajor axis (au)	0.0936 ± 0.0024
Orbital period (d)	24.736959 ± 0.000080
Orbital eccentricity	<0.06

$$\dot{\varpi}_1 = \frac{3}{4} \frac{n_1 m_2}{m_0} \left(\frac{a_1}{a_2} \right)^3 (1 - e_2^2)^{3/2} \left[1 - \frac{5}{4} \left(\frac{a_1 e_2}{a_2 e_1} \right) \frac{\cos \Delta \varpi}{1 - e_2^2} \right], \quad (22)$$

$$\dot{\varpi}_2 = \frac{3}{4} \frac{n_2 m_1}{m_0} \left(\frac{a_1}{a_2} \right)^2 (1 - e_2^2)^{-2} \times \left[1 - \frac{5}{4} \left(\frac{a_1 e_1}{a_2 e_2} \right) \frac{1 + 4e_2^2}{1 - e_2^2} \cos \Delta \varpi \right], \quad (23)$$

where $\Delta \varpi = \varpi_1 - \varpi_2$, m_0 refers to the mass of the star and the parameters with subscript $i = 1$ (2) correspond to the inner (outer) planetary companion.

In practice, the equations for the secular evolution of the system are combined with the equations for the tidal evolution, thus giving a more complete description of the evolution of the system.

3 LHS-1140 B-C. A SYSTEM WITH TWO ROCKY SUPER-EARTHS

LHS-1140 **b-c** are hosted by a mid-M dwarf. The current values for the estimated mean densities of the planets are $\rho_b = 7.5 \pm 1.0 \text{ g cm}^{-3}$ (Dittmann et al. 2017) and $\rho_c = 4.7 \pm 1.1 \text{ g cm}^{-3}$ (Ment et al. 2019). The values of ρ_b and ρ_c suggest that both LHS-1140 b and LHS-1140 c may be rocky Earth-like planets. The hypothesis of a rocky structure was suggested for LHS-1140 b by Dittmann et al. (2017), while the hypothesis of a rocky LHS-1140 c with a magnesium and silicate core was discussed by Ment et al. (2019). Table 1 shows the values of some physical and orbital parameters taken from Ment et al. (2019), which were used in this work to study the spin-orbit evolution of the system.

3.1 Spin-orbit resonances

It is well-known that rocky bodies may be captured in spin-orbit resonances when the rotation evolves from initially fast rotating

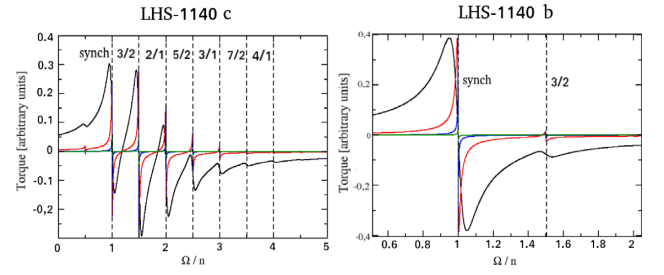


Figure 1. Normalized secular torque as a function of the rotation rate normalized by the mean-motion value. The eccentricity values were fixed at the upper boundary values of Table 1. The black, red, blue, and green curves correspond to $\gamma_i/n_i = 10^{-1}$, 10^{-2} , 10^{-3} , and 10^{-4} , respectively. The black dashed lines indicate the exact values of the spin-orbit resonance commensurabilities.

states (Makarov & Efroimsky 2013; Correia et al. 2014; Ferraz-Mello 2015). Tidal interactions slow down the body’s rotation until an equilibrium configuration of the rotation is reached, where $\langle \dot{\Omega} \rangle = 0$, i.e. the secular variation of the rotation is zero (the same mathematical condition holds for the secular torque, since it is proportional to Ω).

We now explore the possible spin-orbit resonances for LHS-1140 c and b by supposing that their current eccentricities are near the upper boundary values estimated by Ment et al. (2019), namely $e_b = 0.06$ and $e_c = 0.31$ (cf. Table 1).

Fig. 1 shows the normalized torque as a function of the rotation rate, normalized by the mean-motion of the planets. We see that multiple equilibrium configurations of the rotation (corresponding to the points where the curves reach the x-axis) ensue when the relaxation factor is smaller (compare the different curves on each panel). The stable (unstable) equilibrium configurations of the rotation are the descending (ascending) intersections of the normalized torque function with the horizontal axis. For LHS-1140 c, considering $\gamma/n = 0.1$ (corresponding to $\gamma_c = 1.93 \times 10^{-6} \text{ s}^{-1}$), we see that there are three stable resonant spin-orbit configurations, with $\Omega/n = 1$, $\Omega/n = 3/2$, and $2/1$ (cf. black curve on the left-hand panel of Fig. 1). The number of stable spin-orbit resonances increases as γ/n decreases. For LHS-1140 b, the number of stable spin-orbit resonances is smaller due to the smaller eccentricity of the planet, and even for $\gamma/n = 10^{-4}$ (corresponding to $\gamma_b = 2.95 \times 10^{-10} \text{ s}^{-1}$), only the $3/2$ and the synchronous spin-orbit resonances are stable. It is worth mentioning that, in Fig. 1, the time evolution of the rotation rate is represented by the decrease (increase) of the rotation rate in the case of the initially fast-rotating prograde (retrograde) case.

The results of Fig. 1 show that, if the eccentricities of LHS-1140 b and c are close to the upper boundary values estimated by Ment et al. (2019), the rotation of the planets is most likely not synchronous if we suppose that the planets had a past fast rotation rate with $\Omega \gg n$.

3.2 Spin-orbit evolution

We now study the tidal evolution of the planets orbits to assess the time-scales of evolution and the effect of the coupled tidal and secular interactions between the planets. Since the current rotational configuration of the exoplanets is not known, we consider both the initially fast-rotating and synchronous cases to show a more complete description of the possible spin-orbit evolution scenarios of the planets.

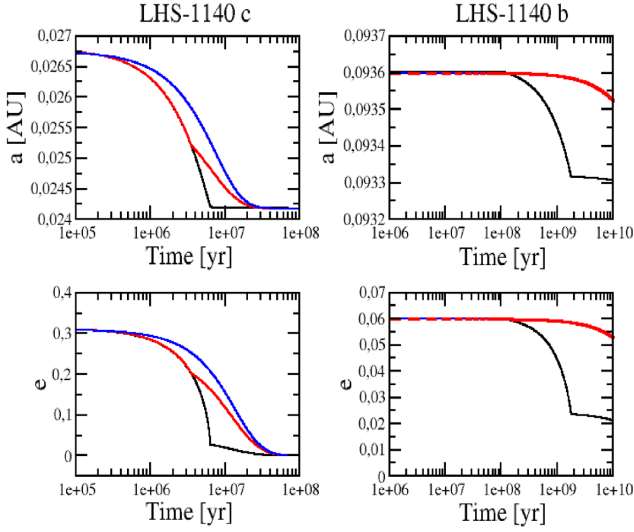


Figure 2. Semimajor axis and eccentricity evolutions of both LHS-1140 c and b, for $\gamma_c = 10^{-7} \text{ s}^{-1}$ and $\gamma_b = 10^{-8} \text{ s}^{-1}$. In these panels, we have (i) the initially fast prograde rotation case (black), (ii) the initially fast retrograde rotation case (red), and (iii) the initially synchronous case (blue). For LHS-1140 b, the initially synchronous case gives the same results as the initially fast-rotating retrograde case.

Several numerical integrations of the differential equations ruling the secular and tidal evolution of the system were performed. For the sake of making clear the contributions of the secular and tidal interactions on the time evolution of the system, we compared the results of the secular model to simulations where only the tidal interactions were considered. In all the calculations performed in this section, we neglect the effects of the stellar tides (i.e. the tides raised in the star by the planets), since some numerical experiments have shown that the stellar tide effects are negligible compared to the planetary tide effects, due to the planetary companions low masses (such results have also been obtained in other works, see e.g. Rodríguez et al. 2011).

Fig. 2 shows a scenario of the tidal evolution of LHS-1140 b and c, considering no secular interactions between the planets. We used $\gamma_b = 10^{-8} \text{ s}^{-1}$ and $\gamma_c = 10^{-7} \text{ s}^{-1}$ (which are values close to the characteristic values used for rocky planets, see Ferraz-Mello 2013, Table 1), where a larger relaxation factor value was attributed to LHS-1140 c given its smaller mean density value when compared to LHS-1140 b. Three initial values of the rotation rate were considered for LHS-1140 c, given by: (i) the initially fast-rotating prograde case (black curve); (ii) the initially fast-rotating retrograde case (red curve); and (iii) the initially synchronous case (blue curve). For LHS-1140 b (right panels), we have: (i) the initially fast-rotating prograde case (black curve); and (ii) the initially fast-rotating retrograde case (red curve). In this case, the initially synchronous case gives the same results as the initially fast-rotating retrograde case, since no other spin-orbit resonances are possible other than synchronism, due to the smaller initial eccentricity value for this planet (see Fig. 1). By analysing the results of Fig. 2, we see that the eccentricity damping occurs more rapidly in the fast rotating cases (black curves), when compared to the initially synchronous configuration. The capture in the synchronous regime can be detected by analysing the eccentricity decay curve. Indeed, in all panels of Fig. 2, there is a characteristic elbow in all the curves corresponding to the initially fast rotating cases. This elbow corresponds to the point where the planets rotation

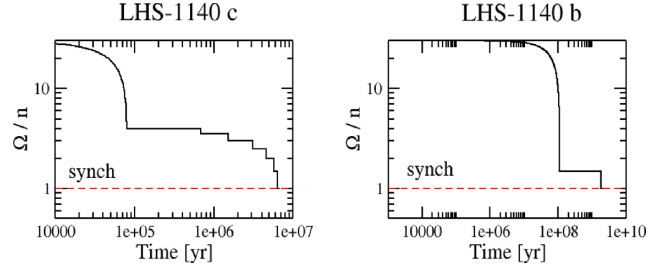


Figure 3. Rotational evolution of LHS-1140 c and b, corresponding to the initially fast-rotating prograde cases of Fig. 2. The initial rotation was taken such that $\Omega/n = 30$. The red dashed lines correspond to the synchronous rotation value $\Omega = n$.

reaches synchronism. Such visible signature of the capture in the synchronous rotation regime was already discussed by other authors (Rodríguez et al. 2012). The spin evolution of the planets in the initially fast-rotating prograde case of Fig. 2 can be seen in Fig. 3. As it is expected, the time of capture in the synchronous regime (cf. Fig. 3) corresponds to the time where the elbow is seen in the panels of Fig. 2.

We also emphasize the staircase behaviour of the rotation rate as a function of time in Fig. 3. This behaviour is a consequence of the fact that the graph of the torques versus the rotation rate shows a succession of kinks that act as barriers for the evolution of the rotation. For instance, consider the case shown by the black curve in Fig. 1 (left). One body whose rotation velocity is initially high (i.e. $\Omega \gg n$) will evolve leftwards (the torque is negative) until it reaches the 2/1 spin-orbit resonance, where the torque sign changes and the rotation can no longer evolve. The body remains trapped in that resonance. However, when the eccentricity decreases, the height of the peak at that kink also decreases. As the tidal evolution of the eccentricity is continuously decreasing, the height of the peak may become negative and the barrier of positive torques disappear. The rotation will again evolve leftwards up to reach the next resonance (in the considered example, the 3/2 spin-orbit resonance). This behaviour will repeat itself up to the point where the rotation is trapped into the synchronous rotation rate state. Such kinks of the torques are also responsible for speeding up the process of rotation rate decay when the rotation approaches the neighbourhood of spin-orbit resonances (the torques are higher when Ω approaches spin-orbit resonances). Such evolutionary behaviour is characteristic of stiff bodies (where $\gamma \ll n$).

Several other numerical integrations to study the tidal evolution of the planets, considering no secular interactions between them, were performed, and we varied the planets relaxation factor values. We verified that the time-scale for which orbital circularization takes place scales with γ^{-1} for the characteristic range of values of the relaxation factor of stiff bodies, namely $\gamma \ll n$.

Fig. 4 shows two scenarios of the orbital evolution of LHS-1140 c and b considering both tidal and secular interactions between the planets. We have $\gamma_c = 10^{-7} \text{ s}^{-1}$ and $\gamma_b = 10^{-8} \text{ s}^{-1}$ on the black curves, and $\gamma_c = 10^{-8} \text{ s}^{-1}$ and $\gamma_b = 10^{-9} \text{ s}^{-1}$ on the red curves. The characteristic decay of the eccentricities due to the tidal interactions is present. The secular interactions are responsible for the oscillatory behaviour of the planetary eccentricities. Additionally, the existence of the secular interactions cause an entanglement of the planetary eccentricities, and the characteristic time-scale of orbital circularization of the inner planet (LHS-1140 c) rules the eccentricity decay of the outer planet (LHS-1140 b). This effect can

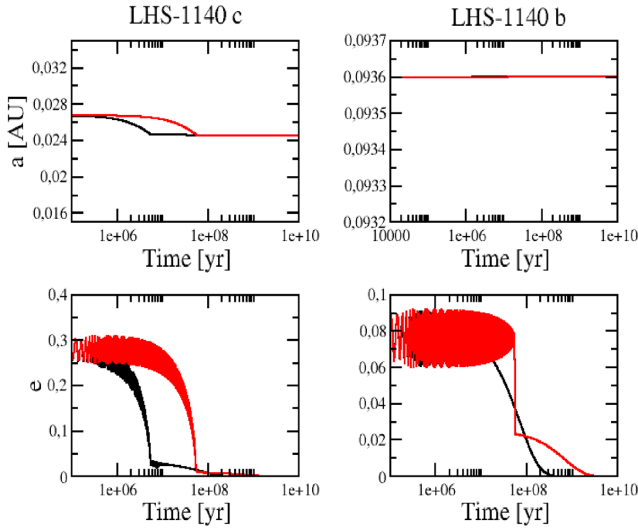


Figure 4. Orbital evolution of both LHS-1140 c and b, considering secular and tidal interactions. The black curves show an evolution scenario with $\gamma_c = 10^{-7} \text{ s}^{-1}$ and $\gamma_b = 10^{-8} \text{ s}^{-1}$, while the red curves show a scenario when $\gamma_c = 10^{-8} \text{ s}^{-1}$ and $\gamma_b = 10^{-9} \text{ s}^{-1}$.

be seen by comparing the time-scales of orbital circularization of LHS-1140 b in Figs 2 and 4.

One last aspect regarding the orbital evolution of the planets in the case of Fig. 4 is the lack of planetary migration for the outer planet. This effect is due to the decrease in the time-scale of orbital circularization of the outer planet as a consequence of the coupling of the planetary eccentricities. The decay of the rotation rate to stable spin-orbit resonant states and the orbital circularization processes are no longer events that happen sequentially (which was the case in the purely tidally evolving scenario). In the secularly evolving case, these events take place on approximately the same time-scale for the outer planet, and the most significant effect of the planetary migration (which happens only when the planet has already reached synchronism or non-synchronous spin-orbit resonances) does not take place.

The relaxation factor of the planets was varied between 10^{-6} and 10^{-9} s^{-1} , by maintaining the same ratio between the relaxation factor values of $\gamma_b/\gamma_c = 0.1$. We verified that the time-scale for orbital circularization of the planets is inversely proportional to γ_c when we consider both tidal and secular interactions. The existence of secular interactions between the planets causes an entanglement in the planetary eccentricities, which decreases the time-scale of orbital circularization of the outer planet when compared to the case where no secular interactions are considered between the planets. We also verified that the time-scale of orbital circularization is approximately 1 order of magnitude larger in the initially synchronous and fast-rotating retrograde cases, when compared to the initially fast-rotating prograde case.

We analysed the spin and orbit evolution of the system by considering that the two planets have a small value of the relaxation factor (which is consistent with the discussions presented in Dittmann et al. 2017 and Ment et al. 2019 regarding the planets compositions and internal structure models). The results of the numerical experiments have shown that the eccentricity decay of both planets is ruled by the eccentricity decay of the inner planet. The secular interactions between the planets cause a coupling between the planetary eccentricities, thus forcing the eccentricity decay of the outer planet at a time much smaller than the time-scale

Table 2. Parameters for the K2-18 system after Cloutier et al. (2019), except for K2-18 b eccentricity value, which was taken from Sarkis et al. (2018), and the periods of the planets b and c, which were taken from Montet et al. (2015) and Cloutier et al. (2017), respectively.

K2-18	Parameter value
Stellar mass (M_\odot)	0.495 ± 0.004
Stellar radius (R_\odot)	0.469 ± 0.010
Effective temperature (K)	3503 ± 60
Rotation period (d)	39.63 ± 0.50
Age (Gyr)	–
K2-18 c	Parameter value
Planet mass ($M_\oplus \times \sin i$)	5.62 ± 0.84
Planet radius (R_\oplus)	–
Mean density (g cm^{-3})	–
Semimajor axis (au)	0.0670 ± 0.0002
Orbital period (d)	8.962 ± 0.008
Orbital eccentricity	<0.2
K2-18 b	Parameter value
Planet mass (M_\oplus)	8.63 ± 1.35
Planet radius (R_\oplus)	2.711 ± 0.065
Mean density (g cm^{-3})	2.4 ± 0.4
Semimajor axis (au)	0.1591 ± 0.0004
Orbital period (d)	32.94488 ± 0.00281
Orbital eccentricity (*)	0.20 ± 0.08

of eccentricity decay due to the outer planet tidal interactions alone. However, the rotation rate and the semimajor axis evolution are not affected by secular interactions. Thus, the rotation of the outer planet may reach synchronism much later than the inner planet. In this case, if the synchronization of the outer planet is reached after orbital circularization has already taken place, the semimajor axis evolution of the outer planet may be neglected.

4 K2-18 B-C. A SYSTEM WITH A LOW-DENSITY SUPER-EARTH AND A SMALL INNER PLANET

K2-18 b was firstly detected in 2015 (Montet et al. 2015). In 2017, Cloutier et al. provided a constraint for the planet’s density through combined data obtained from the HARPS and CARMENES instruments. In the latter work, the authors estimated a mean density of $\rho_b = 3.3 \pm 1.2 \text{ g cm}^{-3}$ for this planet. Moreover, the existence of another planetary companion (namely, K2-18 c) in this system was firstly discussed. The existence of K2-18 c was confirmed in 2019, by Cloutier et al. In this same work, the physical and orbital parameters of K2-18 b were updated. The parameters used in this work are given in Table 2. All data were taken from Cloutier et al. (2019), except from K2-18 b eccentricity value, which was taken from Sarkis et al. (2018), and the orbital periods values of K2-18 b and c, which were taken from (Montet et al. 2015) and Cloutier et al. (2017), respectively.

The mean density of K2-18 b is currently estimated to be $\rho_b = 2.4 \pm 0.4 \text{ g cm}^{-3}$ (Cloutier et al. 2019). Comparing such value with the estimated mean densities of the Earth (ρ_{ear}) and Neptune (ρ_{nep}), we see that ρ_b is closer to ρ_{nep} , thus suggesting that a higher value of the relaxation factor (typical of gaseous bodies) would be the most reasonable assumption for such planet. However, taking into account the classification of K2-18 b as a PHE, we might expect an Earth-like composition for such planet, in which case we would

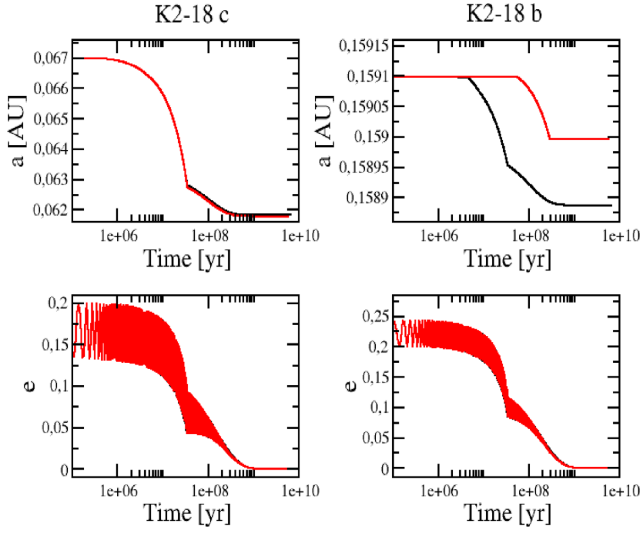


Figure 5. Semimajor axis and eccentricity evolution of K2-18 **b-c** in the case of a rocky K2-18 **c** with a relaxation factor of $\gamma_c = 10^{-7} \text{ s}^{-1}$. Two cases with different values for γ_b are shown, and we have $\gamma_b = 10^{-7} \text{ s}^{-1}$ in the black curve and $\gamma_b = 10^{-8} \text{ s}^{-1}$ in the red curve.

have a small value for the relaxation factor with γ_b in the interval 10^{-7} – 10^{-9} s^{-1} .

For K2-18 **c**, an estimation of the planet mean radius is not currently available. Thus, we cannot estimate precisely the range of values of the relaxation factor of this planet. Since it was verified, in the previous section, that the eccentricity decay of secularly evolving two-planets systems is ruled by the decay of the inner planet eccentricity, we analyse the orbital evolution considering both a Neptune-like gaseous structure and an Earth-like rocky structure for K2-18 **c** in order to obtain a more complete scenario of the time-scales of orbital circularization for such system.

4.1 Case 1. A rocky K2-18 **c**

In the case of a rocky K2-18 **c** with an Earth-like structure, we would have $R_c = 1.77 R_\oplus$ (which gives a mean density equal to the Earth’s mean density value), and a range of values of $\gamma_c = 10^{-7}$ – 10^{-9} s^{-1} for the relaxation factor. Considering such range of values of γ_c , the rotation may be captured in non-synchronous spin-orbit resonances, provided the initial rotation rate of the body is such that $\Omega \gg n$. We considered several numerical integrations of the secular model for the evolution of the system, where the relaxation factor of K2-18 **b** was varied from $\gamma_b = 10^{-7}$ to $\gamma_b = 10^{-8} \text{ s}^{-1}$. In all the cases, an initially fast-rotating state for both the planets was assumed with $\Omega_0 = 30n$, and the eccentricities were set to $e_0 = 0.2$ (Sarkis et al. 2018; Cloutier et al. 2019).

Fig. 5 shows the results of two numerical integrations of the tidal secular model. On the black curves, we set $\gamma_b = 10^{-7} \text{ s}^{-1}$ and on the red curves we set $\gamma_b = 10^{-8} \text{ s}^{-1}$. In both cases, we used $\gamma_c = 10^{-7} \text{ s}^{-1}$. Both the rotation of K2-18 **b** and **c** are trapped in non-synchronous spin-orbit resonances since the initial values of the eccentricities of both planets are of the order $e = 0.2$. As the eccentricity decay takes place, non-synchronous spin-orbit resonances no longer exist and both planets reach synchronism. The point where the rotation rate of the planets reaches synchronism corresponds to the point where the characteristic elbow is seen in all the panels of Fig. 5 (such behaviour was already discussed in the previous section).

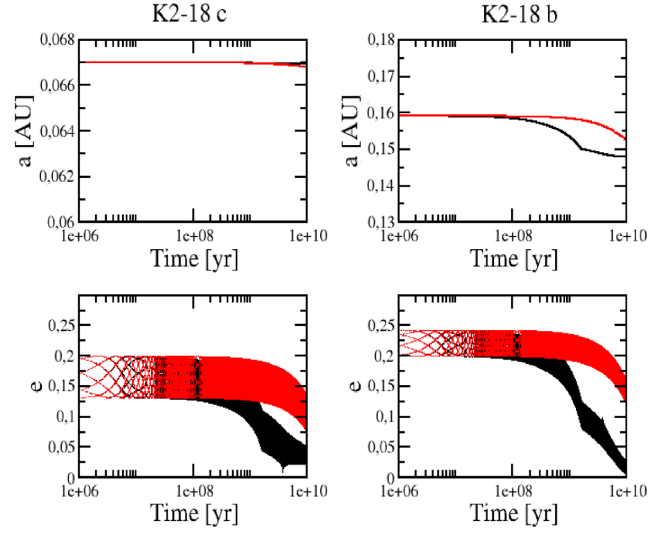


Figure 6. Semimajor axis and eccentricity evolution of K2-18 **b-c** in the case of a gaseous Neptune-like K2-18 **c** with a relaxation factor of $\gamma_c = 1 \text{ s}^{-1}$. Two cases with different values for γ_b are shown, and we have $\gamma_b = 10^{-7} \text{ s}^{-1}$ in the black curve and $\gamma_b = 10^{-8} \text{ s}^{-1}$ in the red curve.

The time-scale of orbital circularization of the system is independent of the relaxation factor of K2-18 **b**. In both cases shown in Fig. 5, the semimajor axis variation of the outer planet is relatively small.

4.2 Case 2. A gaseous K2-18 **c**

In the case of a predominantly gaseous structure for K2-18 **c**, the relaxation factor may be in the range 1 – 100 s^{-1} . We chose the mean radius value of K2-18 **c** giving approximately the same mean density value of Neptune, corresponding to $R_c = 2.68 R_\oplus$.

Fig. 6 shows a scenario of the orbital evolution of K2-18 **b-c** considering $\gamma_b = 10^{-7}$ (black curve) and $\gamma_b = 10^{-8} \text{ s}^{-1}$ (red curve). In both cases we used $\gamma_c = 1 \text{ s}^{-1}$. In this case, we see that the orbital circularization time-scale of the planets is no longer ruled by the inner planet eccentricity decay, but by the eccentricity decay of the outer planet. Such characteristic is a consequence of the fact that the eccentricity decay of the outer planet due to tidal interactions occurs more rapidly due to its relaxation factor value, despite the fact that its distance to the star is much bigger than the distance between the inner planet and the star. Since the eccentricities of the planets are coupled as a consequence of the secular interactions, the eccentricity decay of the outer planet forces the eccentricity decay of the inner planet.

Another interesting characteristic of the results shown in Fig. 6 is that a moderately high eccentricity value for the planets can be maintained for a time interval of some Gyr, provided that $\gamma_b = 10^{-8} \text{ s}^{-1}$. Such scenario would not be possible if we considered a small value for the relaxation factor of K2-18 **c** (see Fig. 5 and the discussion of Case 1). Thus, the comparison of the eccentricity decay time-scales of Cases 1 and 2 taking into account the eccentricity estimation given by Sarkis et al. (2018) for K2-18 **b** (namely $e_b = 0.20 \pm 0.08$) allows us to conclude that the inner planet (K2-18 **c**) of the system may be predominantly gaseous, with a big value for the relaxation factor. Otherwise, orbital circularization would already have taken place on a time-scale of approximately 0.1 Gyr (cf. Fig. 5).

4.3 Discussion

The lack of information on the radius of the inner planet forced us to study the orbital evolution of the system considering both a predominantly rocky (Case 1) and a predominantly gaseous (Case 2) structure for the inner planet. In both cases, we supposed a small value for the relaxation factor of K2-18 b due to the possibility of this planet being a PHE. In Case 1, we verified that the eccentricity damping of both planets is dominated by the inner planet's eccentricity decay (as it was the case of the LHS-1140 b-c system). The results show that orbital circularization is reached after approximately 0.1 Gyr, supposing that the initial eccentricities of the planets are $e_0 = 0.2$ and $\gamma_c = 10^{-7} \text{ s}^{-1}$. Moreover, the time-scale of orbital circularization is independent of the value of γ_b . Analysing the eccentricity constraint for K2-18 b given by Sarkis et al. (2018) and the time-scales of orbital circularization considering a rocky K2-18 c, we see that it is highly unlikely for K2-18 b to have an eccentricity of the order 0.1 if the inner planet (K2-18 c) has a rocky composition. Such results show that the inner planet of the system is more likely a gaseous mini-Neptune with a large value of the relaxation factor (of the order $1\text{--}100 \text{ s}^{-1}$), which is the scenario shown in Case 2. In such case, we verified that an eccentricity of $e_b = 0.2$ can be maintained for a time-scale of some Gyr if $\gamma_b \leq 10^{-8} \text{ s}^{-1}$.

We also performed other simulations considering an initially small eccentricity value for K2-18 c ($e_c \approx 0.05$) and a moderately high eccentricity for K2-18 b ($e_b \approx 0.2$) to investigate the possibility of having a stiff Earth-like nearly circular K2-18 c and a currently eccentric K2-18 b. However, the results have shown that the moderately high value of the eccentricity of K2-18 b would excite the eccentricity of K2-18 c, thus leading to the same scenario shown in Case 1.

5 CONCLUSION

We have used the creep tide theory to present a model describing the spin and orbit evolution of exoplanetary systems with two planetary companions whose internal structure composition may be described by two distinct regimes of the relaxation factor: (i) for predominantly gaseous planets, the relaxation factor was supposed to lie in the range of $1\text{--}100 \text{ s}^{-1}$. (ii) For predominantly rocky planets, we supposed that the relaxation factor was varied between 10^{-7} and 10^{-9} s^{-1} . Additionally to the planetary tidal interactions, we simultaneously computed the effects of secular interactions between the planets, in order to have a more realistic description of the mechanisms ruling the orbital evolution of the system. Stellar tide effects were neglected due to the small planetary masses (which lie in the interval of $1\text{--}10 M_\oplus$).

The secular model was applied to the LHS-1140 b-c and K2-18 b-c exoplanetary systems. For the LHS-1140 b-c exoplanetary system, the results have shown that, if both exoplanets are rocky planets (which is consistent with the discussions presented by Dittmann et al. 2017), the time-scales of rotational synchronization and eccentricity decay due to tidal interactions are much smaller than the estimated age of the system. Thus, we conclude that the planets are probably in nearly circular orbits and with their rotation periods synchronized with their orbital periods. We emphasize that the orbital circularization of the planets would already have taken place even if we suppose higher values for the initial eccentricities used in the simulations, provided that the inner planet is considered as a rocky planet. Nevertheless, since no precise estimations of the current eccentricities exist, we cannot exclude the possibility of the

planets being in moderately eccentric orbits. In that case, the planets would rather be characterized as Neptune-like gaseous planets. Thus, better constraints on the planets uniform viscosity coefficient (and consequently, the planets response to tidal stress) may be obtained when more precise estimations of the planets eccentricities exist. For the K2-18 b-c exoplanetary system, we compared the time-scales of orbital and rotational evolution of the planets to the eccentricity estimations of the planets. The combination of these data has led us to conclude that the inner planet cannot be a rocky super-Earth if we consider the eccentricity estimations for K2-18 b after Sarkis et al. (2018), namely $e_b = 0.20 \pm 0.08$. The outer planet may be a rocky super-Earth with a relaxation factor of the order $\gamma_b \leq 10^{-8} \text{ s}^{-1}$, in which case the orbital circularization would take place on a time-scale of some Gyr. In all the cases analysed in this work, we have verified that the secular interactions couple the planets eccentricities, and the planet with the faster eccentricity decay rules the eccentricity decay of both planets. We emphasize that the initial values of the eccentricities of the planets were chosen to be the current estimated values. However, the results would hold for any other arbitrarily chosen initial eccentricity values.

Additionally to the analyses presented in this work for K2-18 b-c and LHS-1140 b-c, we also calculated the time-scales of orbital and rotational evolution of some single-planet systems where the planet is currently classified as a PHE. The analyses were performed for Kepler-61 b, Kepler-440 b, Kepler-442 b, and Kepler-443 b (the orbital and physical parameters of these systems were taken from Ballard et al. 2013 and Torres et al. 2015). In all these cases, the lack of the mass estimation of the planets forced us to consider both the cases of gaseous and rocky bodies to study the tidal evolution of the planets. We observed that, due to the large values of the orbital periods of the planets (with $P_{\text{orb}} > 100 \text{ d}$ for Kepler-440, 442 and 443 b and $P_{\text{orb}} \approx 59.8 \text{ d}$ for Kepler-61 b), the time-scales of orbital evolution are much larger than 1 Gyr, independently of the value of the relaxation factor of the planets. Thus, no constraints on the relaxation factor of the planets can be obtained by analysing the eccentricity decay of these planets.

ADDITIONAL INFORMATION

Competing Interests: The authors declare no competing interests.

ACKNOWLEDGEMENTS

This investigation is funded by the National Research Council, CNPq, Grant 302742/2015-8 and by FAPESP, Grants 2016/20189-9, 2017/25224-0, and 2019/21201-0. This investigation is part of the thematic project FAPESP 2016/13750-6.

REFERENCES

- Adams E. R., Seager S., Elkins-Tanton L., 2008, *ApJ*, 673, 1160
- Ballard S. et al., 2013, *ApJ*, 773, 98
- Barnes R., 2017, *Celest. Mech. Dyn. Astron.*, 129, 509
- Barr A. C., Dobos V., László L., 2018, *A&A*, 613, A37
- Batygin K., Stevenson D. J., 2013, *ApJ*, 769, L9
- Bolmont E., Raymond S. N., Leconte J., Matt S. P., 2012, *A&A*, 544, A124
- Bolmont E., Gallet F., Mathis S., Charbonnel C., Amard L., Alibert Y., 2017, *A&A*, 604, A113
- Cloutier R. et al., 2017, *A&A*, 608, A35
- Cloutier R. et al., 2019, *A&A*, 621, A49
- Correia A. C. M., Boué G., Laskar J., Rodríguez A., 2014, *A&A*, 571, A50
- Dittmann J. A. et al., 2017, *Nature*, 544, 333

- Dobbs-Dixon I., Lin D. N. C., Mardling A., Rosemary A., 2004, *ApJ*, 610, 464
- Ferraz-Mello S., 2013, *Celest. Mech. Dyn. Astron.*, 116, 109
- Ferraz-Mello S., 2015, *Celest. Mech. Dyn. Astron.*, 122, 359
- Ferraz-Mello S., 2019, *Satellite Dynamics and Space Missions*. Springer INdAM Series, Vol. 34, Springer, Cham
- Folonier H. A., Ferraz-Mello S., Andrade-Ines E., 2018, *Celest. Mech. Dyn. Astron.*, 130, 78
- Gallet F., Bolmont E., Mathis S., Charbonnel C., Amard L., 2017, *A&A*, 604, A112
- Gomes G. O., Folonier H. A., Ferraz-Mello S., 2019, *Celest. Mech. Dyn. Astron.*, 131, 56
- Hellard H., Csizmadia S., Padovan S., Rauer H., Cabrera J., Sohl F., Spohn T., Breuer D., 2019, *ApJ*, 878, 119
- Kellermann C., Becker A., Redmer R., 2018, *A&A*, 615, A39
- Kuchner M. J., 2003, *ApJ*, 596, L105
- Léger A. et al., 2004, *Icarus*, 169, 499
- Makarov V. V., Efroimsky M., 2013, *ApJ*, 764, 27
- Mardling R. A., 2007, *MNRAS*, 382, 1768
- Mardling R. A., Lin D. N. C., 2002, *ApJ*, 573, 829
- Mayor M., Queloz D., 1995, *Nature*, 378, 355
- Ment K. et al., 2019, *AJ*, 157, 32
- Montet B. T. et al., 2015, *ApJ*, 809, 25
- Rodríguez A., Ferraz-Mello S., Michtchenko T. A., Beaugé C., Miloni O., 2011, *MNRAS*, 415, 2349
- Rodríguez A., Callegari N., Michtchenko T. A., Hussmann H., 2012, *MNRAS*, 427, 2239
- Sarkis P. et al., 2018, *AJ*, 155, 6
- Seager S., Kuchner M., Hier-Majumder C. A., Militzer B., 2007, *ApJ*, 669, 1279
- Torres G. et al., 2015, *ApJ*, 800, 99

This paper has been typeset from a $\text{\TeX}/\text{\LaTeX}$ file prepared by the author.

The Posidonius N-body code and implementation of the creep tide equations

7.1 Introduction

Since the recent boom in the discovery of exoplanetary systems and the diversity on their orbital configurations, the development of N-body integrators aiming specifically at calculating the evolution of planetary systems has been a growing field of study¹. In such field of study, the development of efficient N-body integrators has allowed for the development of new techniques for optimizing the process of numerical integration methods by maximizing the precision of numerical integrations and maintaining the low cost of computational calculations (we remind that long term evolution calculations used to take a prohibitive time to be performed). In the specific case of N-body codes developed to study the dynamics of close-in systems, tidal interactions are an essential additionally to point-mass N-body interactions and, thus, must be implemented in a self-consistent way that can be integrated with the standard Newtonian equations of gravitational interactions. Recent efforts, such as the development of the Mercury-T code (see Bolmont et al. 2015), have aimed at adapting existing numerical codes (e.g., Mercury, see Chambers 1999) to take tidal interactions into account. In the case of Mercury-T, for instance, tidal interactions have been added in the code following the Constant Time Lag (CTL) approach of Mignard (1979). We also cite other recently-developed N-body integrators such as the REBOUND code (Rein and Liu, 2012), which provides a user-friendly python wrapper to execute simulations without the need to program directly in the C language (which is the source

¹ It is worth mentioning that N-body codes had substantial development before exoplanets were discovered, mainly to study the dynamics of star clusters.

programming language of REBOUND), although the inclusion of other effects might require some programming in C language.

The development of N-body codes has also led to a review and improvement of classical methods of numerical integrations, such as the IAS15 integrator (Rein and Spiegel, 2015) (which is an improvement of the Radau15 integration code provided in Everhart 1985) and the WHFast integrator (Rein and Tamayo, 2015) (which is an improvement of the classical Wisdom-Holman symplectic integrator method presented in Wisdom and Holman 1991).

Among the existing N-body open-source codes currently available, the Posidonius code (see Blanco-Cuaresma and Bolmont 2017a) follows a different approach by considering a recently-developed programming language: Rust. A preliminary study of some of the advantages of Rust over Fortran and C++ have already been discussed in Blanco-Cuaresma and Bolmont (2017b). In this chapter, we will present the Posidonius code. We briefly review some of the advantages of the Rust programming language for scientific programming. Afterwards, we discuss the numerical integration methods implemented in Posidonius as well as some additional details regarding the currently available effects which can be taken into account other than gravitational point-mass interactions. Then, we discuss the implementation of the creep tide theory equations in the code. Finally, we perform two applications to validate the code by considering some dynamical evolution scenarios of the K2-265 b and CoRoT-7 b-c exoplanetary systems. We also discuss some aspects related to the efficiency of the integration methods and the difference in the computation time considering each numerical integration method.

7.2 *The Posidonius code*

7.2.1 *The Rust programming language*

The recently created Rust programming language was released by Mozilla Research, motivated by the development of a new web browser engine. Rust uses patterns coming from functional programming languages and it is designed not only for performance and concurrency, but also for safety. Rust introduces concepts like ownership, borrowing and variable lifetime. Such features allow programmers to avoid problems such as accessing invalid memory regions. They also enforce thread-safety and facilitate the automatic control of the lifetime of objects during compilation time. Thus, there is no need for garbage col-

lector like in Java (see more details in Blanco-Cuaresma and Bolmont 2017b and references therein).

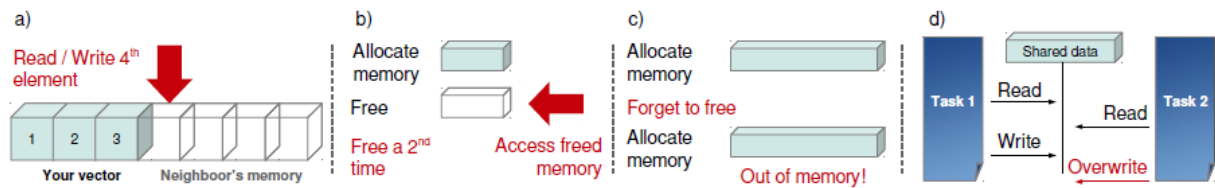


Figure 7.1: Typical memory and concurrency problems of C and Fortran. Figure taken from Blanco-Cuaresma and Bolmont (2017b).

In Rust, variables are non-mutable by default (unless the mutable keyword is used). Thus, they are bound to their content, owing it. When we assign one variable to another (see panel a in Fig. 7.1), we are not copying the content but transferring the ownership, so that the previous variable does not have any content. Such a transfer also occurs for functions (see panel b in Fig. 7.1), and it is important to note that Rust will free the bound resource when the variable binding goes out of scope. Thus, we do not need to manually deallocate the memory. The compiler will validate for us that we are not accessing a memory region that has already been freed (errors are caught at compilation time, before execution time).

Additionally, apart from transferring ownership, we can borrow the content of a variable (see panel c in Fig. 7.1). In this case, two variables have the same content but none of them can be modified, thus protecting us from thread-safety issues. Alternatively, we can borrow in a more traditional way, like in panel d in Fig. 7.1, where the function borrows the content of a variable, operates with it (in this case, it could modify its content) and returns it to the original owner (not destroying it as shown in panel b). Some examples of the borrowing and ownership features are shown in Fig. 7.2.

Although the advantages and features of Rust mentioned above are generally employed in most of the codes developed in Rust, it is possible to violate such features by using unsafe blocks (e.g., when dealing with external libraries written in Fortran, C or C++). If present, unsafe blocks allow us to clearly identify parts of the code which should be carefully audited, keeping them isolated and not making the whole program unsafe by default.

A detailed benchmark comparing implementations of some numerical integrator methods

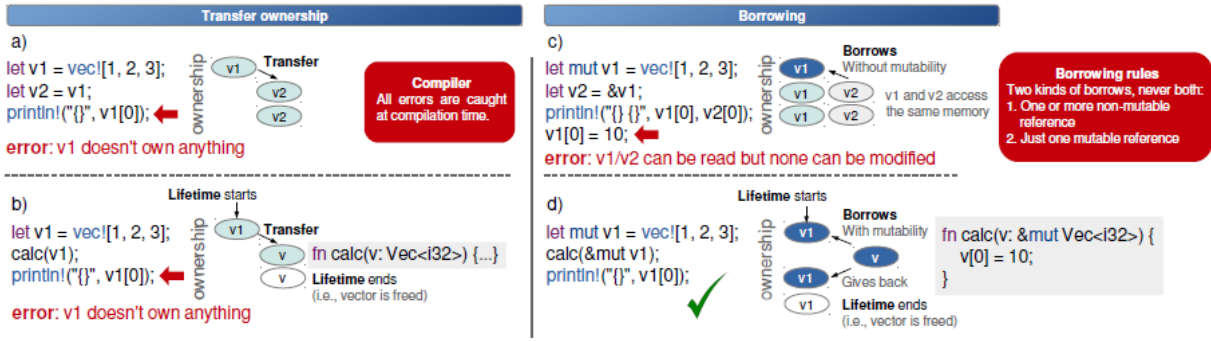


Figure 7.2: Examples of the properties of borrowing and ownership present in Rust.

in C, Fortran, Go and Rust is presented in Blanco-Cuaresma and Bolmont (2017a). The conclusions of such work show that Rust is approximately 10 times faster and the corresponding codes in Go and C. The computation time of Rust is only comparable to Fortran. However, we emphasize the additional safety features of Rust which prevent memory allocation and access issues.

7.2.2 Numerical integration methods

In this section, we present the main concepts of the two integrator methods currently available for use in Posidonius: WHFast and IAS15.²

7.2.2.1 The WHFast integrator (Rein and Tamayo, 2015)

WHFast is a fast and accurate implementation of a Wisdom-Holman symplectic integrator for long-term orbit integrations of planetary systems. To present the functioning and algorithm of the integrator, we begin by defining the Hamiltonian \mathcal{H} of the gravitational N-body system as the sum of kinetic and potential terms in Cartesian coordinates, which reads³

$$\mathcal{H} = \sum_{i=0}^{N-1} \frac{p_i^2}{2m_i} - \sum_{i=0}^{N-1} \sum_{j=i+1}^{N-1} \frac{Gm_i m_j}{|\vec{r}_i - \vec{r}_j|}. \quad (7.1)$$

² Posidonius also provides a leapfrog integration method package, although we do not recommend its use since it is less precise than both WHFast and IAS15.

³ In all the equations presented in this chapter for the N-body interactions, we consider that the system is composed by N bodies with $N - 1$ of them being planets.

To further separate the above Hamiltonian, we could transform to heliocentric coordinates involving the centre of mass and the $\vec{r}_i - \vec{r}_0$. However, cross-terms appear when we perform such a transformation. Jacobi worked out a coordinate system in which the kinetic terms are particularly clean, and the kinetic energy remains a sum of squares. In terms of the Jacobi moments and masses (namely, p'_i and m'_i), Eq. (7.1) becomes

$$\mathcal{H} = \sum_{i=0}^{N-1} \frac{p_i'^2}{2m'_i} - \sum_{i=0}^{N-1} \sum_{j=i+1}^{N-1} \frac{Gm_i m_j}{|\vec{r}_i - \vec{r}_j|}. \quad (7.2)$$

To use the Wisdom-Holman mapping technique, we further split the Hamiltonian by adding and subtracting the term

$$\mathcal{H}_{\text{add}} = \sum_{i=1}^{N-1} \frac{GM_i m'_i}{|\vec{r}_i'|}, \quad (7.3)$$

where

$$M_i = \sum_{j=0}^i m_j. \quad (7.4)$$

Finally, the new form for the Hamiltonian reads

$$\mathcal{H} = \underbrace{\frac{p_0'^2}{2m'_0}}_{\mathcal{H}_0} + \underbrace{\sum_{i=1}^{N-1} \frac{p_i'^2}{2m'_i} - \sum_{i=1}^{N-1} \frac{GM_i m'_i}{|\vec{r}_i'|}}_{\mathcal{H}_{\text{Kepler}}} + \underbrace{\sum_{i=1}^{N-1} \frac{GM_i m'_i}{|\vec{r}_i'|} - \sum_{i=0}^{N-1} \sum_{j=i+1}^{N-1} \frac{Gm_i m_j}{|\vec{r}_i - \vec{r}_j|}}_{\mathcal{H}_{\text{Interaction}}}. \quad (7.5)$$

Now that we separated the full Hamiltonian into individual Hamiltonians, to all of which we know the solution, a symplectic integrator can be constructed for the total Hamiltonian using an operator split method (see e.g., Saha and Tremaine 1992). Following the notation of Rein and Tamayo (2015), we describe the evolution of particles under a Hamiltonian \mathcal{H} for a time dt using the operator notation $\widehat{\mathcal{H}}(dt)$. The notation $\widehat{\mathcal{H}}_2(dt) \circ \widehat{\mathcal{H}}_1(dt)$ means applying operator $\widehat{\mathcal{H}}_1(dt)$ first, then applying operator $\widehat{\mathcal{H}}_2(dt)$. The Wisdom-Holman mapping is defined by a Drift-Kick-Drift operator splitting scheme, the algorithm of which can be described as below:

- (Drift) Evolve the system under $\widehat{\mathcal{H}}_{\text{Kepler}}(dt/2) \circ \widehat{\mathcal{H}}_0(dt/2)$.
- (Kick) Evolve the system under $\widehat{\mathcal{H}}_{\text{Interaction}}(dt)$.
- (Drift) Evolve the system under $\widehat{\mathcal{H}}_{\text{Kepler}}(dt/2) \circ \widehat{\mathcal{H}}_0(dt/2)$.

More detailed aspects of the Wisdom-Holman mapping such as the use of symplectic correctors and methods of solution of the Kepler two-body problem (including the variational equations) can be found in Rein and Tamayo (2015), Sections 2.4 and 2.6 and Mikkola and Innanen (1999).

In terms of the computational procedure of the Wisdom-Holman mapping, we would like to comment that the evolution of $\mathcal{H}_{\text{Kepler}}$ and \mathcal{H}_0 are most easily accomplished in Jacobi coordinates. The interaction Hamiltonian $\mathcal{H}_{\text{Interaction}}$, however, contains terms that depend on both the Cartesian and Jacobi coordinates. The simplest way to calculate these terms is to convert to Cartesian coordinates, evaluate the position vectors, convert the accelerations back to Jacobi accelerations and calculate the remaining terms.

The procedures described up to this point regarding the Wisdom-Holman mapping are the standard procedures originally described in Wisdom and Holman (1991). The improvements performed by Rein and Tamayo (2015) are mainly linked to minor details, many of which are related to finite floating-point precision on modern computers. We will briefly cite the points modified by the authors (without giving detailed explanations of the algorithms involved in such improvements) below:

- Jacobi coordinate transformations: This improvement refers to the method of conversion between Jacobi and Cartesian coordinates.
- Newton's method implementation: Such an improvement is related to the addition of a mathematical operation in the middle of the Newton's method implementation, which is used to solve Kepler's equation
- Initial guess for Kepler's equation: This improvement regards an algorithm for choosing the initial guess when solving Kepler's equation by analysing the timescale over which the orbital radius varies for a given timestep. The variable to be solved using Newton's method is then non-dimensionalized and solved perturbatively assuming small variations from the unit value. For large eccentricities and timesteps, the initial guess is modified to improve computational efficiency.
- C-function calculations: The Kepler solver routine is modified with an optimized algorithm to calculate the c-functions, which are used in the process of finding a solution to Kepler's equation iteratively (see Rein and Tamayo 2015, Section 3.5)

- Implementation of Gauss f- and g-functions: For timesteps smaller than half an orbital period, the f- and g-functions are redefined so that small quantities are summed before they are added to the larger initial values of \vec{r} and \vec{v} , which leads to higher numerical precision.
- Number of coordinate conversions: the conversion of coordinates is performed just twice. The first time for the positions from Jacobi coordinates to the inertial frame, and the second time for the accelerations from the inertial frame to Jacobi accelerations. This optimization trick is only possible under four assumptions: (1) the particle position and velocities are not changed in-between timesteps, (2) outputs are not required at every timestep, (3) variational equations are not integrated and (4) no additional velocity-dependent forces are present.

Finally, we comment that the use of WHFast for the case of velocity-dependent conservative forces and dissipative forces needs additional extensions in which a framework using non-commutative operators are used. In such case, symplectic correctors can be seen as weak splitting correctors (for more details, see Tamayo et al. 2020) and the dissipative forces can be added to otherwise symplectic N-body integrations.

7.2.2.2 The IAS15 integrator (Rein and Spiegel, 2015)

IAS15 is a 15th-order integrator to simulate gravitational dynamics. It is based on a Gauss-Radau quadrature and can handle both conservative and non-conservative forces. The algorithm is an improvement of the 15th-order modified Runge-Kutta integrator presented in Everhart (1985), where several flaws were fixed so that the accuracy stays at machine precision for billions of dynamical times.

The functioning of the IAS15 integrator can be described as follows: we would like to solve a fundamental differential equation of the type

$$y'' = F[y', y, t]. \quad (7.6)$$

Thus, the force equation can have arbitrary velocity-dependent (and therefore non-conservative) terms.

Let us now expand the force (namely, Eq. 7.6) in terms of a polynomial expression which depends explicitly on time through

$$y''[t] \approx y_0'' + a_0 t + a_1 t^2 + \dots + a_6 t^7. \quad (7.7)$$

The constant term is simply the force evaluated at the beginning of the timestep. Introducing the step size dt as well as $h = t/dt$ and $b_k = a_k dt^{k+1}$, the expansion can be rewritten as

$$y''[h] = y_0'' + b_0 h + b_1 h^2 + \dots + b_6 h^7. \quad (7.8)$$

If we rewrite Eq.(7.8) in a convenient way with

$$y''[h] = y_0'' + g_1 h + g_2 h(h - h_1) + g_3 h(h - h_1)(h - h_2) + \dots + g_8 h(h - h_1) \dots (h - h_7), \quad (7.9)$$

we can easily see that the g_k depend only on the force evaluations at substeps h_n with $n \leq k$. In another words, we can update the coefficients g_k when we evaluate the h_n ⁴.

Since we have the expression for the acceleration, both the velocity and the position values can be obtained by direct integration of Eq. (7.8). The trick of the IAS15 integrator is to choose the spacing of the substeps to be Gauss-Radau spacings (rather than, for example, equidistant spacings). For the construction of a 15th-order scheme, we need eight function evaluations.

Finally, to completely evolve the positions and velocities, we need to estimate the b_k coefficients. To do this, we need estimates of the forces during the timestep, which we take at the substeps h_n (the same substep times that we later use to approximate the integrals). The force estimates give us the g_k values which are then converted to the b_k coefficients. Such an implicit system is solved through a predictor-corrector scheme as described below.

First, we come up with a rough estimate for the positions and velocities by making all $b_k = 0$ (predictor phase). Then, we use the forces to calculate better estimates for the positions and velocities (corrector). This procedure is repeated until the desired precision is obtained (for the convergence criterion, see Rein and Spiegel 2015, Section 2.2). In practice, only a few (approximately 2) iterations of the predictor-corrector loop are needed to achieve machine precision.

⁴ It is worth mentioning that the expression for $y''[h]$ in terms of the b_k did not present such a practical dependence for the b_k on h_n .

Up to this point, we described the method involved in the classical Radau15 integrator of Everhart (1985). In Rein and Spiegel (2015), the authors proposed an improvement on the step-size control algorithm. Indeed, the original Radau15 code considered a dimensional parameter to control the precision of the integration scheme. Thus, a simple change in code units can make the Radau15 code fail. Rein and Spiegel (2015) proposed the use of a dimensionless parameter $\epsilon_b < 1$ to control the precision of the algorithm. The procedure to calculate the varying timestep by using ϵ_b can be described as follows: we begin the integration with a timestep provided by the user (namely, the first value of dt_{trial}). In subsequent timesteps, we use the timestep set in the previous step. After integrating through the timestep (i.e., after the predictor-corrector loop achieved convergence for a given timestep), we calculate the following quantity:

$$b_6 = \frac{\max|b_{6,i}|}{\max|y_i''|}. \quad (7.10)$$

The required value of dt (which we call dt_{required}) can be calculated through

$$dt_{\text{required}} = dt_{\text{trial}} \left(\frac{\epsilon_b}{b_6} \right)^{1/7}. \quad (7.11)$$

If $dt_{\text{trial}} > dt_{\text{required}}$, the step is rejected and repeated with a smaller timestep. If the step is accepted, then the timestep for the next step is chosen to be dt_{required} .

One last aspect which we would like to comment is the method of determining ϵ_b . Indeed, the quality of an integration scheme is assessed by analyzing the error estimates. The criterion chosen by Rein and Spiegel (2015) is that the error of the integration scheme E_{scheme} reaches machine precision (10^{-16}). In terms of dt , the control parameter is given by

$$\epsilon_b = \left(\frac{dt}{T} \right)^7 \frac{(2\pi)^7}{7!}, \quad (7.12)$$

where T is the characteristic time-scale. For a nearly circular orbit, for instance, T corresponds to the orbital period.

In terms of the relative integration error E_{rel} , the expression for ϵ_b becomes (see Rein and Spiegel 2015, Section 3.6 for more detailed calculations)

$$\epsilon_b = \left(\frac{E_{\text{rel}} \times 10^{13}}{3.3} \right)^{7/16}. \quad (7.13)$$

We then arrive at $\epsilon_b = 0.028$ for machine-precision values of the integration error.

7.3 Implementation of the creep tide equations

The Posidonius code was designed in a way that facilitates the inclusion of additional effects to the forces other than the gravitational attraction among the bodies. Thus, the inclusion of additional terms in the acceleration can be done by simply computing the cartesian components of the accelerations and then summing them to the overall acceleration expression. In the case of the creep tide, the radial and orthoradial components of the force (namely, F_r and F_o) are given by

$$F_r = \left[-\frac{9}{10} \frac{GM_p M_\star R_p^2}{r^4} \mathcal{E}_\rho \cos 2\delta - \frac{3}{5} \frac{GM_p M_\star R_p^2}{r^4} \mathcal{E}_z \right] \mathbf{r}, \quad (7.14)$$

$$F_o = \left[\frac{3}{5} \frac{GM_p M_\star R_p^2}{r^4} \mathcal{E}_\rho \sin 2\delta \right] (\mathbf{z} \times \mathbf{r}). \quad (7.15)$$

The radial and orthoradial force expressions are then decomposed in their (x, y, z) parts and used as additional perturbations in the overall acceleration expressions.

Finally, the rotation rate of the bodies are evolved by adding the expression for $\dot{\Omega}$, namely

$$\dot{\Omega}_p = -\frac{3GM_\star}{2r^3} \mathcal{E}_\rho \sin 2\delta, \quad (7.16)$$

where, for the stellar rotation rate variation, it suffices to change the subscript of the mass for the corresponding planet to obtain the stellar rotation rate evolution equation.

To implement the creep tide equations in Posidonius, we decided to adopt the constant rotation rate approximation of the theory. In such case, we consider that the rotation rate of the extended body is constant to solve for the shape equations, and afterwards the rotation rate is evolved based on the resulting torque expression. In such a case, the equations ruling the time evolution of the shape of the extended body are explicit analytical expressions. More explicitly, we have

$$\mathcal{E}_\rho \cos 2\delta = \bar{\epsilon}_\rho \sum_{k \in \mathbb{Z}} \mathcal{C}_k [\gamma \cos \phi_k - (2\Omega - kn) \sin \phi_k], \quad (7.17)$$

$$\mathcal{E}_\rho \sin 2\delta = \bar{\epsilon}_\rho \sum_{k \in \mathbb{Z}} \mathcal{C}_k [\gamma \sin \phi_k + (2\Omega - kn) \cos \phi_k], \quad (7.18)$$

$$\mathcal{E}_z = \bar{\epsilon}_z + \frac{\bar{\epsilon}_\rho}{2} \left[\sum_{k \in \mathbb{Z}} \mathcal{Z}_k (kn\gamma \sin k\ell + \gamma^2 \cos k\ell) \right], \quad (7.19)$$

where the auxiliary parameters used in Eqs. (7.17) - (7.19) are given by

$$\phi_k = k\ell - 2\varphi, \quad (7.20)$$

$$\mathcal{C}_k = \frac{\gamma E_{2,2-k}}{\gamma^2 + (2\Omega - kn)^2}, \quad (7.21)$$

$$\mathcal{Z}_k = \frac{E_{0,k}}{k^2 n^2 + \gamma^2}, \quad (7.22)$$

$$\bar{\epsilon}_z = \frac{5\Omega^2 R_p^3}{4GM_p}, \quad (7.23)$$

$$\bar{\epsilon}_\rho = \frac{15 M_\star}{4 M_p} \left(\frac{R_p}{a} \right)^3, \quad (7.24)$$

$$\gamma = \frac{R_p g d}{2\eta}. \quad (7.25)$$

We decided to adopt a seventh-order polynomial approximation to calculate the Cayley coefficients in Posidonius. Such method was chosen instead of the complete integral representation since the seventh-order polynomial expressions are valid for eccentricity values up to $e = 0.4$. Additionally, calculating numerically the integral

$$E_{q,k}(e) = \frac{1}{2\pi\sqrt{1-e^2}} \int_0^{2\pi} \frac{a}{r} \cos[q\varphi + (k-q)\ell] d\varphi, \quad (7.26)$$

for every timestep would significantly increase the number of computations to be performed and decrease the performance of the code.

Some additional information regarding the creep tide implementation architecture in Posidonius are provided in the Appendix A, together with some instructions on how to prepare initial conditions files and executables for running the Posidonius code. A stable version of the Posidonius code including both the CTL as well as the creep tide equations can be found in <https://github.com/gabogomes/posidonius>.

7.4 Application: The K2-265 b planet

To test the performance and results of the Posidonius code, we considered initially an application to study the spin-orbit evolution of a single-planet system, which allows a direct comparison to the results coming from secular evolution numerical integrations (where the latter were performed using the Equations of Chapter 4). In Table 7.1, we

present the orbital and physical parameters of the system. We mention that the chosen values for the relaxation factor of the planet in all the cases we performed is not consistent with estimations of the viscosity value of gaseous or rocky planets. The values chosen for γ for the simulations we performed are fictitious and are used only for code testing purposes.

Additionally to the four simulation setups presented in Table 7.1, we also considered two simulations using a secular evolution code, in which we compute the time evolution of the rotation rate, the semi-major axis and the eccentricity following the equations presented in Chapter 4. The integrator used in the secular evolution code is the Radau15 integrator (see Everhart 1985).

Table 7.1 - Data for the stellar and planetary parameters used in our simulations. The values for the physical and orbital parameters of both the star and the planet were taken from Lam et al. (2018).

$M_\star (M_\odot)$	$R_\star (R_\odot)$	$M_p (M_\oplus)$	$R_p (R_\oplus)$	$\gamma_p [s^{-1}]$	$a [AU]$	Ω_0/n	Integrator
0.915	0.977	6.54	1.71	$8.6 \times 10^{-6} (\gamma < n)$	0.03376	5	WHFast
0.915	0.977	6.54	1.71	$8.6 \times 10^{-4} (\gamma > n)$	0.03376	5	WHFast
0.915	0.977	6.54	1.71	$8.6 \times 10^{-6} (\gamma < n)$	0.03376	5	IAS15
0.915	0.977	6.54	1.71	$8.6 \times 10^{-4} (\gamma > n)$	0.03376	5	IAS15

The results of our numerical experiments for the spin-orbit evolution of K2-265 b are given in Fig. 7.3. The black, red and blue curves correspond to the results coming from the IAS15, WHFast and secular evolution code integrations, respectively. We can see that the results among the different integrators and different codes are in very good agreement.

For the case with $\gamma < n$ (i.e., the top panels), the rotation rate reaches the 2/1 spin-orbit resonance and is captured in it. Afterwards, the eccentricity decay takes place until the eccentricity is sufficiently small so that the 2/1 resonance is no longer an equilibrium configuration of the rotation. The planet rotation then evolves to the 3/2 spin-orbit resonance. The same process described for the 2/1 resonance takes place until the 3/2 resonance is no longer an equilibrium configuration, resulting in a synchronous rotation for the planet.

For the case with $\gamma > n$, we can see that the rotation rate evolves directly to the super-synchronous stationary solution. It is also worth mentioning that the super-synchronous

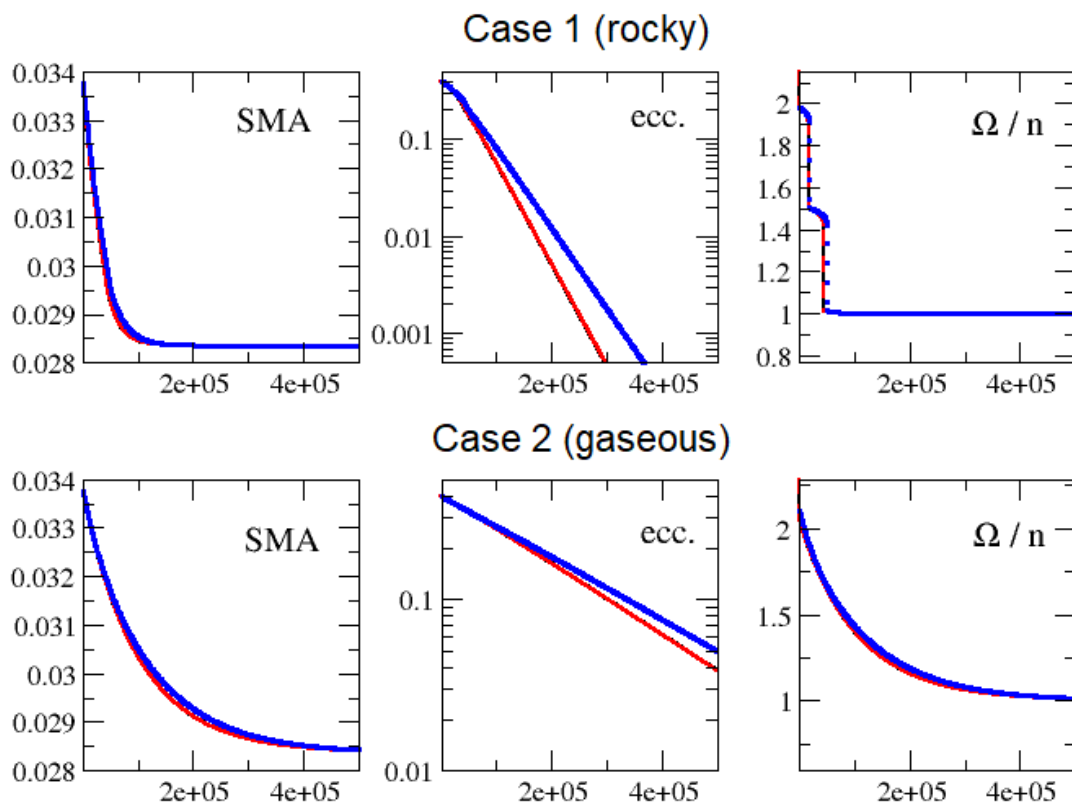


Figure 7.3: Semi-major, eccentricity and rotation evolution of K2-265 b on the left, middle and right panels, respectively. The upper panels refer to the rocky body case (i.e., the case for which $\gamma = 8.6 \times 10^{-6} \text{ s}^{-1}$), while the bottom panels refer to the gaseous case (i.e., the case for which $\gamma = 8.6 \times 10^{-4} \text{ s}^{-1}$). The black (resp. red) curve corresponds to the Posidonius simulation results using the IAS15 (resp. WHFast) integration method. The blue curves are the results coming from the secular evolution code.

stationary solution evolves to the synchronous stationary solution as the eccentricity decreases. The value of Ω/n decreases with time as a consequence of the fact the the eccentricity decays, thus shifting the equilibrium value of the rotation rate to smaller values of Ω/n .

7.5 Application: The CoRoT-7 b-c system

The CoRoT-7 b-c system is one of the most studied systems among the currently known exoplanetary systems. Indeed, CoRoT-7 b is known for being the first super-Earth with a measured radius. The pioneer works studying mass and radius values for the planets of such system were the papers of Queloz et al. (2009); Leger et al. (2009); Hatzes et al.

(2010); Ferraz-Mello et al. (2010, 2011)⁵. Other works (see e.g., Pont et al. 2011 and references therein) have also provided estimations of the eccentricity values of the planets based on the radial velocity data. The orbital and rotational dynamics of the planets were studied in other works (see e.g., Jackson et al. 2010; Rodríguez et al. 2011; Callegari and Rodríguez 2013; Rodríguez et al. 2016). The currently estimated physical and orbital parameters of the system are given in Table 7.2.

As it can be seen in Table 7.2, the estimated eccentricity of the planets is relatively high given their orbital period values. One of the possible explanations for such values is the existence of excitations of the eccentricities due to planet-planet gravitational interactions. However, another possibility which has recently been explored by Rodríguez et al. (2016) is the so-called eccentricity pumping mechanism. According to such mechanism, the planetary eccentricity could have been excited as a consequence of the excitation of the planetary J_2 coefficient⁶.

Table 7.2 - Stellar and planetary parameters for the CoRoT-7 b-c system, extracted directly from the tables provided in exoplanet.eu.

Body	Mass	Radius	a [AU]	e	P_{orb} days
Star	0.93	0.87	--	--	--
Planet b	4.74	1.52	0.0172	0.12	0.85
Planet c	13.559	--	0.046	0.12	3.698

To test the performance and results of the Posidonius code and the creep equations in the case of this multiplanetary system, we perform numerical experiments to study the possibility of obtaining the same scenarios as in Rodríguez et al. (2016) for the eccentricity pumping of CoRoT-7 b-c. We consider both a case for which the relaxation factor of the planets is large (i.e., such that $\gamma \gg n$), as it is the case of gaseous planets such as mini-

⁵ It is worth mentioning that, due to the stellar activity of the CoRoT-7 host star, several data analysis techniques and works have aimed specifically at studying the relationship between the stellar activity and the planets periodic signals, see e.g., Lanza et al. (2010); Boisse et al. (2011).

⁶ It is worth mentioning that, although the application of the eccentricity pumping mechanism was performed to CoRoT-7 b-c in Rodríguez et al. (2016), the eccentricity pumping mechanism was firstly proposed by Correia et al. (2012).

Neptunes, and a case for which the relaxation factor of the planets is small (of the order 10^{-7} s^{-1}), which is the case of small Earth-like planets. It is worth commenting that the values chosen for the relaxation factor and viscosity used in this section are not exactly the same as the ones used in Rodríguez et al. (2016) since the time required to perform the numerical integrations is sufficiently large (of the order 10-15 days). We thus decided to use intermediate values, in which case the evolution scenarios can be studied with a shorter time of numerical integration. The values for the viscosities of the planets used in the simulations are, thus, experimental and should not be used for a realistic analysis of the dynamics of the system. It is also worth emphasizing that the typical timescale of evolution of the system is scaled roughly by the same factor used in the choice of the relaxation factor values.

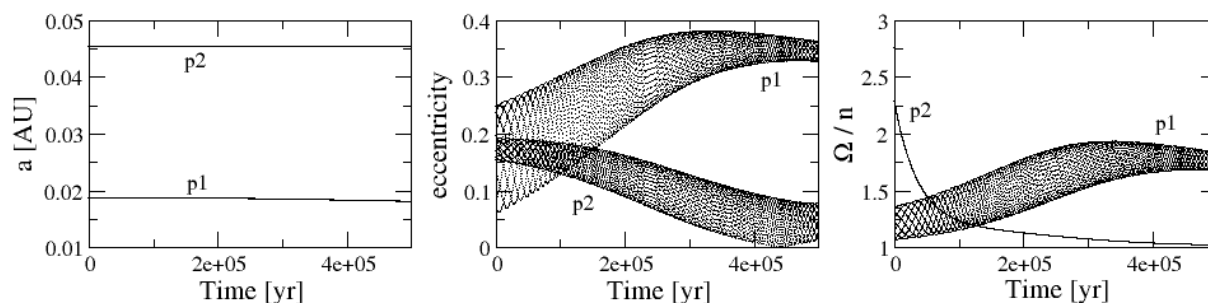


Figure 7.4: Semi-major axis, eccentricity and rotation rate evolution of CoRoT-7 b-c considering $\eta = 10^{12} \text{ Pa s}$ (corresponding to $\gamma = 0.7 \text{ s}^{-1}$ for the inner planet), in the left, middle and right panels, respectively. The labels in the panels (p1 and p2) indicate to which planet the curve refers (p1 refers to CoRoT-7 b while p2 refers to CoRoT-7 c).

Fig. 7.4 shows the results of a simulation performed using Posidonius, for CoRoT-7 b-c. We chose viscosity values for the planets of $\eta = 10^{12} \text{ Pa s}$. We can see that the semi-major axis evolution is not significant. On the other hand, the eccentricity significantly evolves even though only 500 kyr are shown in the figure. The eccentricity of the inner planet increases after approximately 100 kyr of evolution, while the eccentricity of the outer planet decreases. This feature is a consequence of the angular momentum conservation of the system. For the rotation rate evolution results (right panel), we can see that both planets evolve to the super-synchronous state, with the inner planet value for the equilibrium rotation being significantly larger than the corresponding value for the outer planet. This is a consequence of the larger eccentricity value for the inner planet, which shifts the equilibrium value of Ω/n for the inner planet.

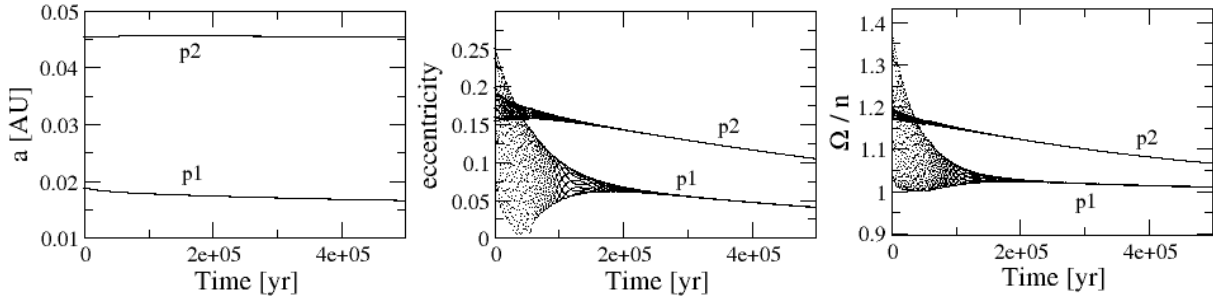


Figure 7.5: Semi-major axis, eccentricity and rotation rate evolution of CoRoT-7 b-c considering $\eta = 10^{14}$ Pa s (corresponding to $\gamma = 7 \times 10^{-3} \text{ s}^{-1}$ for the inner planet), in the left, middle and right panels, respectively. The labels in the panels (p1 and p2) indicate to which planet the curve refers (p1 refers to CoRoT-7 b while p2 refers to CoRoT-7 c).

In Fig. 7.5, we show a simulation performed with exactly the same initial conditions as in Fig. 7.4, but for $\eta = 10^{14}$ Pa s. In this case, tidal interactions are stronger and the eccentricity decay effect due to the tides overcome the effects of the eccentricity pumping effect. As a consequence, the eccentricity values of both planets decreases rapidly to values of the order 0.1 or smaller after around 500 kyr of orbital evolution. As in the previous case, the rotation rate of the planets follow the evolution of the eccentricity, i.e., as the eccentricity decreases, the equilibrium rotation rate decreases as well.

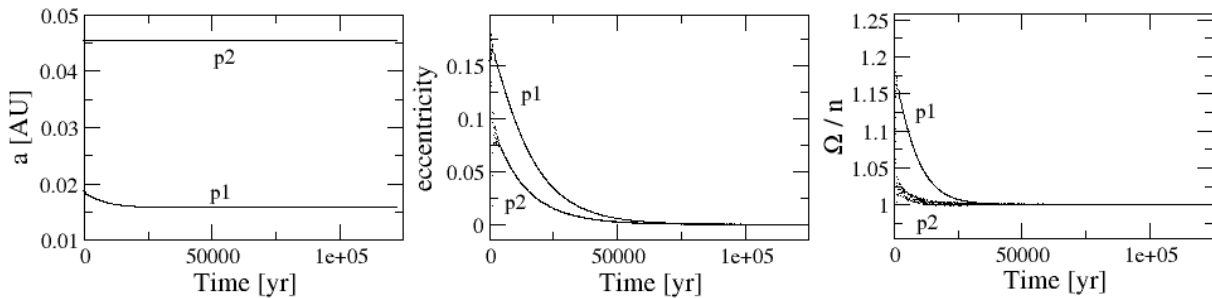


Figure 7.6: Semi-major axis, eccentricity and rotation rate evolution of CoRoT-7 b-c considering $\eta = 10^{16}$ Pa s (corresponding to $\gamma = 7 \times 10^{-5} \text{ s}^{-1}$ for the inner planet), in the left, middle and right panels, respectively. The labels in the panels (p1 and p2) indicate to which planet the curve refers (p1 refers to CoRoT-7 b while p2 refers to CoRoT-7 c).

Finally, we present a case for the spin-orbit evolution of CoRoT-7 b-c considering a viscosity value which corresponds to $\gamma \approx n$. The results are shown in Fig. 7.6. We can see that even though only approximately 170 kyr of evolution are shown, such time baseline is already sufficient to capture the eccentricity decay to a value around 10^{-3} (not visible in the figure). The rotation of the planets evolves to synchronism, and the planets remain

on nearly-circular orbits, with tidal interactions damping any kind of eccentricity pumping caused by planet-planet gravitational interactions or J_2 excitations.

7.6 Final considerations

In this chapter, we have presented the Posidonius code and described some of the main tools regarding the numerical integration process. We also described the method which we used to implement the creep tide equations in the code. For the sake of clarity, more computational aspects of Posidonius are also given separately in Appendix A. We have performed two applications to verify the functioning and consistency of Posidonius: 1) An application to the K2-265 b exoplanetary system, in which case we compared both the two integrators of Posidonius (namely IAS15 and WHFast) with the results coming from a secular evolution code developed by us (in which case we evolve the semi-major, eccentricity and rotation rate following the equations presented in Chapter 4), and 2) An application to the CoRoT-7 b-c exoplanetary system, in which case we briefly revisited the phenomenon of eccentricity pumping caused by J_2 excitations of the inner planet. In the first case, the results of Posidonius and the secular evolution code are in very good agreement. For the second application, we verified qualitatively the same aspects as the ones presented and discussed in Rodríguez et al. (2016)⁷. We have also verified that, when tidal dissipation is too strong, the eccentricity mechanism is absent and no eccentricity increase is present. Since we know that the current value of the planets eccentricities is moderate (with $e = 0.12$ for both planets), we can make the hypothesis that either the planets have very large values of the relaxation factor or their relaxation factor is very small. In these two cases, eccentricity pumping occurs and the eccentricity of the planets could be maintained at relatively high values until the present.

⁷ We emphasize that the values of the Maxwell time (which can be translated to the creep tide relaxation factor parameter by making $\tau = 1/\gamma$) used by Rodríguez et al. (2016) are different from the corresponding values of the relaxation factor used in our simulations, and thus we focused on a qualitative interpretation of the results rather than a more thorough quantitative comparison of the results.

Influence of equilibrium tides on transit-timing variations of close-in super-Earths

The following article addresses an implementation of the creep tide theory in the `Po-sidonius` code. It considers the application of the code to study transit timing variations (TTVs) induced by tidal interactions. A specific application is considered to K2-265 b (see Lam et al. 2018), which is a super-Earth orbiting a G8V star with an orbital period of 2.37 days. The maximum estimated value of the eccentricity of the planet is 0.163. We analyse the influence of the number of transit events on the amplitudes of the TTVs, as well as the influence of other parameters such as the stellar mass and the semi-major axis value. The influence of the planetary rotation rate and the eccentricity value are also discussed.

The results for the application we performed allowed us to verify that the most important contribution to TTVs coming from planetary tidal interactions is the orbital decay effect. We also verified that, in agreement with other previous works on the subject (see e.g., Ragozzine and Wolf 2009), the amplitude of the tidally-induced TTVs scales with the number of transits squared. Thus, a long time baseline is critical for confirming that the TTVs are in fact induced by tidal interactions. We also investigated the effects of the stellar oblateness and the general relativity on the TTVs, and concluded that in the specific case of K2-265 b, such effects lead to much smaller contributions than the ones coming from tidal interactions to the TTVs. In cases where the effects of the general relativity can cause contributions of the same order of the tidal interactions, we can use occultation timing variations (OTVs) to disentangle between the effects of the general relativity and the tidal interactions on the changing orbit of the system. In terms of numerical values

for the physical and orbital parameters of exoplanetary systems for which the detection of tidally-induced TTVs would be optimistic, we concluded that, for planets with a semi-major axis smaller than 0.02 AU, an amplitude of the tidally induced TTVs on the order of 20 – 80 s may be reached even for small observation timescales (on the order of 2 – 3 yr), provided that the stellar mass is between 0.5 and 1.0 Solar masses.

Influence of equilibrium tides on transit-timing variations of close-in super-Earths

I. Application to single-planet systems and the case of K2-265 b

G. O. Gomes^{1,2}, E. Bolmont¹, and S. Blanco-Cuaresma³

¹ Observatoire de Genève, Université de Genève, Chemin Pegasi 51, 1290 Sauverny, Switzerland

² Instituto de Astronomia, Geofísica e Ciências Atmosféricas, IAG-USP, Rua do Matão 1226, 05508-900 São Paulo, Brazil
e-mail: gabrielogomes@usp.br

³ Harvard-Smithsonian Center for Astrophysics, 60 Garden Street, Cambridge, MA 02138, USA

Received 22 December 2020 / Accepted 28 April 2021

ABSTRACT

With the current growth in the discovery of close-in low-mass exoplanets, recent works have been published with the aim to discuss the influences of planetary interior structure parameters on both the shape of transit light curves as well as variations in the timing of transit events of these planets. One of the main aspects explored in these works is the possibility that the precession of the argument of periapsis caused by planetary tidal interactions may lead to unique effects on the transit light curves of the exoplanets, such as the so-called transit-timing variations (TTVs).

In this work, we investigate the influence of planetary tidal interactions on the transit-timing variations of short-period low-mass rocky exoplanets. For this purpose, we employed the recently developed creep tide theory to compute tidally induced TTVs. We implemented the creep tide in the recently-developed Posidonius *N*-body code, thus allowing for a high-precision evolution of the coupled spin-orbit dynamics of planetary systems. As a working example for the analyses of tidally induced TTVs, we applied our version of the code to the K2-265 b planet. We analyzed the dependence of tidally induced TTVs with the planetary rotation rate, uniform viscosity coefficient, and eccentricity. Our results show that the tidally induced TTVs are more significant in the case where the planet is trapped in nonsynchronous spin-orbit resonances, in particular the 3/2 and 2/1 spin-orbit resonant states. An analysis of the TTVs induced separately by apsidal precession and tidally induced orbital decay has allowed for the conclusion that the latter effect is much more efficient at causing high-amplitude TTVs than the former effect by 2–3 orders of magnitude. We compare our findings for the tidally induced TTVs obtained with Posidonius with analytical formulations for the transit timings used in previous works, and we verified that the results for the TTVs coming from Posidonius are in excellent agreement with the analytical formulations. These results show that the new version of Posidonius containing the creep tide theory implementation can be used to study more complex cases in the future. For instance, the code can be used to study multiplanetary systems, in which case planet-planet gravitational perturbations must be taken into account in addition to tidal interactions to obtain the TTVs.

Key words. planet-star interactions – planets and satellites: interiors – planets and satellites: terrestrial planets

1. Introduction

The measurement of transit-timing variations (TTVs) has been shown to be an invaluable tool in the field of exoplanetary detection and characterization (Agol et al. 2005). In multiplanet systems, for instance, the gravitational interaction between planets leads to deviations from strictly Keplerian orbits. These deviations in turn lead to a shift in the timing of planetary transit events. The TTV effects are usually investigated by directly running *N*-body dynamical simulations. The advantage of such an approach lies in the fact that the results are valid for arbitrary eccentricities and inclinations of the planets. Several studies have employed the technique of TTV analyses to improve the mass measurement of disturbing (and, in some cases, nontransiting) planetary companions, as well as their orbital parameters (Nesvorný & Morbidelli 2008; Lithwick et al. 2012; Nesvorný & Vokrouhlický 2016; Agol et al. 2021).

Although planet–planet interactions are among the main effects leading to high-amplitude TTVs, any interaction causing

a drift of a planet from its unperturbed Keplerian orbit can induce TTVs. For very close-in planets, for instance, general relativity-induced apsidal precession and tidally induced orbital decay (see e.g., discussions in Ragozzine & Wolf 2009) may be strong enough to cause significant variations in the orbital elements of the planets and lead to observable TTVs. The detection of such TTVs caused by these disturbing forces depends on the magnitude of the induced TTVs compared to the precision of the instruments measuring transit events.

In the field of study of tidal interactions and subsequent spin-orbit evolution, the parameter which is responsible for dictating the response to tidal stress is the complex Love number, which is the ratio of the additional gravitational potential induced by the internal mass redistribution of the planet due to tidal deformation to the external tidal potential created by the perturber (Love 1911). Thus, provided that the tidally induced TTVs are big enough to be detected, matching the observed TTVs with the values estimated by numerical simulations of the tidal evolution of the system would allow us to estimate the complex Love

number of the bodies, thus providing us with invaluable information regarding the interior structure of the planets and their rotational state, for example.

In a recent work, [Patra et al. \(2017\)](#) analyze transit and occultation data of WASP-12 b (see e.g., [Hebb et al. 2009](#); [Haswell 2018](#) and references therein) and show that the planet could be undergoing an orbital decay process corresponding to a mean period decay of $\dot{P} = -29 \pm 3 \text{ ms yr}^{-1}$, which would be compatible with a stellar quality factor on the order of 2×10^5 . However, the authors point out that apsidal precession induced by planetary tidal deformation could provide the same effects on the transit curves when compared to the orbital decay process induced by stellar tides, in which case the Love number of the planet would be on the order of $k_p = 0.44 \pm 0.10$. The confusion between the two effects could only be solved if occultation data were analyzed in addition to transit data, in which case the contribution from apsidal precession gives an opposite sign to the occultation timing variation curves when compared to orbital decay. In a more recent work, [Yee et al. \(2020\)](#) analyze new transit and occultation measurements for the same system and verify that a model for the transit timings considering orbital decay is more likely to explain the TTV curve of the planet when compared to a model considering apsidal precession.

Although the recent discussions raised by [Ragozzine & Wolf \(2009\)](#), [Patra et al. \(2017\)](#), and [Yee et al. \(2020\)](#), for example, have paved the way for future investigations regarding the tidally induced TTVs, few studies have been dedicated to an exploration of these effects for low-mass close-in rocky exoplanets. The reason for the lack of studies for such class of exoplanets is linked to the fact that only a few of them had been discovered before the results of photometric surveys coming from missions such as *Kepler* ([Youdin 2011](#); [Fressin et al. 2013](#)) and TESS ([Sullivan et al. 2015](#)). However, with the recent boom in the discovery and characterization of close-in rocky super-Earths and the improvement in the precision of the transit timing measurements, an investigation of the potential effects of planetary tidal interactions on TTVs is necessary. This may be a powerful approach at assessing the planets' interior structure (see e.g., [Bolmont et al. 2020b](#)) as well as other parameters, such as their current rotational state, where the rotational state of the planet does indeed depend on its interior structure parameters, such as its viscosity and density.

In the field of study of tidal interactions on rocky super-Earths, several works have aimed to provide a description of the equilibrium tide and its subsequent orbital evolution scenarios by employing advanced rheological models to describe the response of these exoplanets to tidal stress (see e.g., [Efroimsky 2012](#); [Ferraz-Mello 2013](#); [Tobie et al. 2019](#); [Walterová & Běhounková 2020](#) and references therein). However, to the best of our knowledge, none of these advanced rheological models have been consistently implemented in high-precision and open-source N -body codes¹, which would allow for a multiplanet simulation of tidally induced TTVs to a good degree of accuracy. In a recent work, [Bolmont et al. \(2020b\)](#) investigate the magnitude of tidally induced TTVs for the TRAPPIST-1 multiplanet system by employing the implementation of a classical approach of tidal interactions based on the constant time lag (CTL) formulation ([Mignard 1979](#)). However, this specific approach does

not allow for a full exploration of the TTVs considering all the nuances of equilibrium tide interactions in rocky bodies, such as the temporary entrapment in spin-orbit resonances for moderately high values of eccentricities and planetary viscosity (see e.g., [Makarov & Efroimsky 2013](#) and references therein). Such aspects, which are consistently reproduced using more complex rheological models, may indeed play an important role in the orbital evolution of the planets and, consequently, lead to significant changes in the tidally induced TTVs when compared to scenarios obtained by employing classical theories of equilibrium tides, such as the CTL approach.

Taking the discussions presented in [Delisle et al. \(2017\)](#) and [Bolmont et al. \(2020b\)](#) into account as well as the lack of an investigation of the topic of tidally induced TTVs using a more sophisticated tidal interaction model for the planet, we revisit, in this work, such topic in the frame of the creep tide theory ([Ferraz-Mello 2013](#); [Folonier et al. 2018](#)). For this purpose, we implemented the tidal interactions model in the recently-developed N -body code called Posidonius² ([Blanco-Cuaresma & Bolmont 2017](#); [Bolmont et al. 2020b](#)).

The creep tide theory describes the response of bodies to tidal stress by supposing a Newtonian creep equation for the extended body's shape evolution. This equation is the result of a linear approximation of the Navier-Stokes equation for a low-Reynolds-number flow (i.e., for cases where viscous forces are much more significant than inertial forces, see [Ferraz-Mello 2013](#)). We consider the formulation of the theory for homogeneous bodies whose rotation axes are perpendicular to the orbital plane (i.e., the zero-obliquity case). The equations ruling the spin and orbit evolution of the planets are shown to be easy to implement in the Posidonius code, and the response of bodies to tidal stress depends on only one parameter, which is the uniform viscosity coefficient of the body.

As a real example of a tidally induced TTV analysis, we study the K2-265 b super-Earth ([Lam et al. 2018](#)). We explore the influence of tidally induced TTVs as a function of several parameters, such as the planet's viscosity, eccentricity, and rotational state. We also present a broad analysis of the amplitudes of tidally induced TTVs as a function of other parameters, such as the planet's mass and radius values and its semi-major axis. Such a broad analysis allows us to identify the main parameters leading to bigger influences on the TTV values. Finally, we also provide some examples of recently-discovered systems for which tidally induced TTVs would have the highest amplitudes for a given number of transit events. Such systems are the candidates for which tidally induced TTVs can be more easily detected by the instruments measuring transit events, such as the TESS telescope.

This work is organized as follows: in Sect. 2, we present the main results of the creep tide theory which were used for the implementation in the Posidonius code and briefly give some details regarding the numerical setup used in the calculations of the TTVs. In Sect. 3, we investigate the magnitudes of tidally induced TTVs for the K2-265 b planet considering the influences of tuning the parameters presenting the most significant uncertainties in their determined values (i.e., the eccentricity, rotational state, and viscosity of the planet). We also compare the results for the TTVs obtained by using Posidonius with the

¹ We emphasize that a self-consistent formulation for the coupled spin-orbit and shape evolution considering a Maxwell rheology for the planet was presented in [Correia et al. \(2014\)](#), which was extended to study (i) three-body exoplanetary systems by [Rodríguez et al. \(2016\)](#) and [Delisle et al. \(2017\)](#) and (ii) N -body systems by [Correia & Delisle \(2019\)](#).

² The new version of the code including the implementation of the creep tide theory is available for download in <https://github.com/gabogomes/posidonius/tree/posidonius-creep>, and the original Posidonius website is <https://www.blancocuaresma.com/s/posidonius>

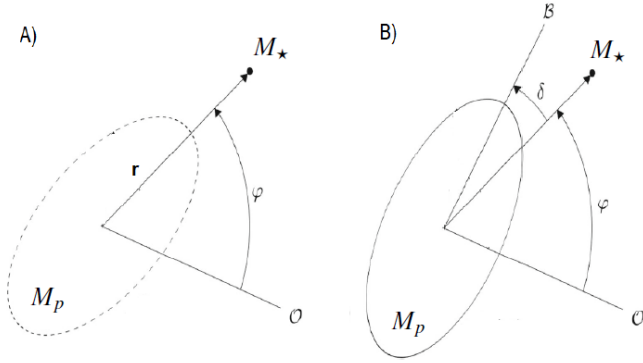


Fig. 1. Scheme of the geometrical setup considered in the framework of the creep tide theory, partially reproduced from Folonier et al. (2018). On the *left*, we have the pure static case in which the primary always points toward the companion, which is at a distance r from the primary. On the *right*, we have the case in which the response of the primary is delayed due to the primary's nonzero viscosity value. In both panels, O is the reference direction used to measure the true anomaly (φ).

ones obtained by employing some analytical approximations to generate transit timing curves. In Sect. 4, we perform a broad exploration of tidally induced TTVs as a function of both orbital and physical parameters of the star and the planet. In Sect. 5 we present the discussions of the work, and Sect. 6 summarizes our conclusions.

2. Numerical setup

In this section, we provide the essential equations of the creep tide theory which were used in the implementation in the Posidonius code. We also present some additional information regarding the numerical integrator which provides the better precision for the calculations of transit timing events.

2.1. The creep tide theory

The creep tide theory considers the deformations of an extended body (hereafter the primary) due to the disturbing gravitational potential due to a point-mass companion. The time evolution of the primary's figure is described by three parameters: the equatorial deformation of the body (\mathcal{E}_ρ), polar oblateness (\mathcal{E}_z), and the angle giving the orientation of the tidal bulge (δ), as it is described in the scheme in Fig. 1. These three parameters are evolved by employing a Newtonian creep equation, which is an approximate solution of the Navier-Stokes equation in the case of a low-Reynolds-number flow (see Ferraz-Mello 2013; Folonier et al. 2018 for more details).

Employing the expression for the potential of the resulting triaxial figure of the primary, we computed the forces and the torque acting on the companion. While the radial and ortho-radial components of the force (namely \mathbf{F}_r and \mathbf{F}_o) were used to compute the orbital evolution of the system, the reaction to the torque acting on the companion was used to compute the rotational evolution of the primary. The calculations are straightforward and they entail (Folonier et al. 2018)

$$\mathbf{F}_r = \left[-\frac{9}{10} \frac{GM_p M_\star R_p^2}{r^4} \mathcal{E}_\rho \cos 2\delta - \frac{3}{5} \frac{GM_p M_\star R_p^2}{r^4} \mathcal{E}_z \right] \mathbf{r}, \quad (1)$$

$$\mathbf{F}_o = \left[\frac{3}{5} \frac{GM_p M_\star R_p^2}{r^4} \mathcal{E}_\rho \sin 2\delta \right] (\mathbf{z} \times \mathbf{r}), \quad (2)$$

Table 1. Meaning of the parameters presented in Eqs. (7)–(12).

Symbol	Meaning
ℓ	Mean anomaly
φ	True anomaly
n	Orbital mean-motion
γ	Planetary relaxation factor
η	Planetary uniform viscosity
d	Planetary mean density
g	Planetary surface gravity
$E_{q,k}$	Cayley coefficient

$$\dot{\Omega} = -\frac{3GM_\star}{2r^3} \mathcal{E}_\rho \sin 2\delta. \quad (3)$$

The unit vectors \mathbf{r} and $\mathbf{z} \times \mathbf{r}$ point toward the radial and ortho-radial directions, respectively, with \mathbf{z} being a unit vector pointing to the same direction of the orbital angular momentum vector. The parameters G , M_p , R_p , and M_\star are the gravitational constant, mass and radius of the planet, and mass of the star, respectively.

To compute the time evolution of \mathcal{E}_ρ , \mathcal{E}_z , and δ , we employed the analytical solutions for these parameters in the frame of the constant rotation rate approximation (Gomes et al. 2019), which read

$$\mathcal{E}_\rho \cos 2\delta = \bar{\epsilon}_\rho \sum_{k \in \mathbb{Z}} C_k [\gamma \cos \phi_k - (2\Omega - kn) \sin \phi_k], \quad (4)$$

$$\mathcal{E}_\rho \sin 2\delta = \bar{\epsilon}_\rho \sum_{k \in \mathbb{Z}} C_k [\gamma \sin \phi_k + (2\Omega - kn) \cos \phi_k], \quad (5)$$

$$\mathcal{E}_z = \bar{\epsilon}_z + \frac{\bar{\epsilon}_\rho}{2} \left[\sum_{k \in \mathbb{Z}} \mathcal{Z}_k (k^2 n^2 \sin k\ell + \gamma^2 \cos k\ell) \right], \quad (6)$$

where

$$\phi_k = k\ell - 2\varphi, \quad (7)$$

$$C_k = \frac{\gamma E_{2,2-k}}{\gamma^2 + (2\Omega - kn)^2}, \quad (8)$$

$$\mathcal{Z}_k = \frac{E_{0,k}}{k^2 n^2 + \gamma^2}, \quad (9)$$

$$\bar{\epsilon}_z = \frac{5\Omega^2 R_p^3}{4GM_p}, \quad (10)$$

$$\bar{\epsilon}_\rho = \frac{15}{4} \frac{M_\star}{M_p} \left(\frac{R_p}{a} \right)^3, \quad (11)$$

$$\gamma = \frac{R_p g d}{2\eta}. \quad (12)$$

A list containing the meaning of each symbol in Eqs. (7)–(12) is presented in Table 1. The Cayley coefficients appearing in Eqs. (8) and (9) (namely $E_{2,2-k}$ and $E_{0,k}$) are eccentricity-dependent³. Their values can be computed numerically, by means of the integral

$$E_{q,k}(e) = \frac{1}{2\pi \sqrt{1-e^2}} \int_0^{2\pi} \frac{a}{r} \cos[q\varphi + (k-q)\ell] d\varphi. \quad (13)$$

³ We note that the expansion in eccentricity coefficients presented in this work converges only for eccentricities up to ≈ 0.40 . For a formulation of the creep tide theory allowing arbitrary eccentricity values, see Folonier et al. (2018).

Although the evaluation of high-order Cayley coefficients is relatively straightforward by employing Eq. (13), we used polynomial expressions for these coefficients to order e^7 (see Ferraz-Mello 2015, Appendix B.4, Tables 1 and 2) in all the applications performed in this work since such an approximation has already been shown to be sufficient to calculate the tidal evolution for eccentricity values up to approximately 0.4 (see Ferraz-Mello 2013, Appendix).

We emphasize that the constant rotation rate approximation presented in this section can be used in our study since the librations of the rotation rate which ensue in spin-orbit resonant states do not significantly change the orbital evolution of the system or, consequently, the TTVs. However, they may make important contributions to the overall energy dissipated in the body (see discussions in Folonier et al. 2018). Additionally, we point out that the constant rotation rate solution is not a secular solution of the creep tide equations, and short-period oscillations of the shape coefficients are present. The shape evolution of the primary implicitly depends on the mean and true anomalies, see Eqs. (4)–(6).

2.2. Implementation in Posidonius

To explore the tidally induced TTVs with a high-degree of numerical precision, we implemented the creep tide theory following the scheme presented in Sect. 2.1 (see Eqs. (1)–(3)) in the recently developed Posidonius code (Blanco-Cuaresma & Bolmont 2017). We compared the performance and numerical precision of two integrators: WHFast (Rein & Tamayo 2015), which is a symplectic integrator considering a fixed time-step scheme for the numerical integration of the equations of motion, and IAS15 (Rein & Spiegel 2015), which considers an adaptive time-step control scheme based on Gauss-Radau spacings for the numerical integration of the equations of motion. We performed some numerical experiments and verified that, although WHFast is approximately 20 times faster than the IAS15 integrator, the latter provides a bigger numerical precision for very short timescales of evolution, which is essential for evaluating the TTVs properly. Thus, we considered the IAS15 in all simulations regarding the TTV calculations, where we set $\max(\Delta t) = 0.0005$ days, with $\max(\Delta t)$ being the maximum value of the allowed time-step of the numerical integration scheme. Such a value of $\max(\Delta t)$ provides a precision of approximately 10^{-4} s for the TTVs, where such a precision value was estimated by analyzing the TTVs of a single-planet case with no disturbing forces other than the point-mass gravitational interaction between the star and the planet. More information regarding the numerical validation and performance of the code can be found in the appendix.

2.3. Calculation of TTVs

To calculate the TTVs of each transit event, we employed the same procedure described in Bolmont et al. (2020b). The procedure is briefly described below for the sake of clarity.

We first performed a numerical simulation employing the Posidonius code, including the effects of the tidal interactions. Then, we used the data coming from the time right before and right after the point in which the planet crosses a reference direction (in our case, we chose the X axis to be the reference direction) and linearly interpolated the orbit to find the exact time for which $X = 0$. Then, we performed a least-square linear fit using the LinearRegression algorithm from the `linear_model` package of `scikit-learn` (see Pedregosa et al.

2011). This process allows us to write the transit mid-time associated with each transit event as $T = an_T + b$, where T and n_T are the transit mid-times and transit number, respectively, and the coefficients a and b are the best-fit orbital period and transit mid-time of the first transit event, respectively. Afterwards, we computed the differences between the transit times coming from the linear fit (i.e., the calculated transit times, C_i) and the transit times resulting from the numerical simulations employing Posidonius (i.e., the observed transit times, O_i). The difference between these two quantities (namely, $O_i - C_i$) are the TTVs.

We note that the above procedure to obtain the tidally induced TTVs is slightly different from the one employed by Bolmont et al. (2020b). In our procedure, we did not calculate the TTV difference between the pure N-body case and the case considering the tidal interactions. The absence of that part of the procedure is due to the fact that, since we are dealing with a single-planet system, the expected TTV for the pure N -body case is zero (i.e., there are no TTVs for a nonperturbed Keplerian orbit).

3. Application to K2-265 b

In this section, we analyze the tidally induced TTV for K2-265 b. We analyze the effect of tuning some parameters of the planet presenting the most significant uncertainties (namely, its viscosity, eccentricity, and rotation rate) on the amplitudes of the TTVs. We also forecast tidally induced TTVs considering bigger numbers of transit data than the currently available number of reported transit events.

3.1. Currently available data for the system

The K2-265 b super-Earth was discovered by Lam et al. (2018). The authors used photometry data from the K2 mission and high-precision radial velocity measurements from the High Accuracy Radial velocity Planet Searcher (HARPS, Mayor et al. 2003), and they estimated the planet radius and mass with an uncertainty of 6 and 13%, respectively. The planet orbits a G8V bright star with an apparent magnitude of $V = 11.1$. The estimated radius and mass of the planet are $R = 1.71 \pm 0.11 R_{\oplus}$ and $6.54 \pm 0.84 M_{\oplus}$, which corresponds to a mean density of $7.1 \pm 1.8 \text{ g cm}^{-3}$. Such a mean density value is typical of rocky Earth-like planets.

Regarding the orbital parameters of the planet, Lam et al. (2018) obtained $a = 0.03376 \pm 0.00021$ AU and $e = 0.084 \pm 0.079$. An estimation of the age of the system (henceforth referred to as τ) was also made available by Lam et al. (2018) by combining observational data and stellar evolution tracks coming from the Dartmouth stellar evolution code. The resulting estimated age for the system is $\tau = 9.7 \pm 3.0$ Gyr. The complete set of parameters which were used to perform our numerical experiments is shown in Table 2.

3.2. Estimation of the uniform viscosity value

To study the tidally induced TTV for K2-265 b, we first had to constrain the range of values for the uniform viscosity coefficient which are consistent with both the putative rocky composition of the planet as well as the current eccentricity estimations available. For that purpose, we used a secular code to calculate tidal evolution scenarios (see Appendix) to derive a mathematical relation linking the uniform viscosity coefficient to the timescale of orbital circularization of the planet, namely τ_{circ} . Differently from other works where τ_{circ} is defined as the inverse of the

Table 2. Physical and orbital parameters for K2-265 b and its host star after Lam et al. (2018).

Parameter	Value
Planet mass (M_{\oplus})	6.54 ± 0.84
Planet radius (R_{\oplus})	1.71 ± 0.11
Planet mean density (g cm^{-3})	7.1 ± 1.8
Semimajor axis (AU)	0.03376 ± 0.00021
Orbital period (days)	2.369172 ± 0.000089
Eccentricity	0.084 ± 0.079
Stellar mass (M_{\star})	0.915 ± 0.017
Stellar rotation period (days)	32 ± 10
Age (Gyr)	9.7 ± 3.0

Notes. The values represent the median of the posterior and 68.3% credible interval. For more details on the methods of determination of each parameter, see Lam et al. (2018).

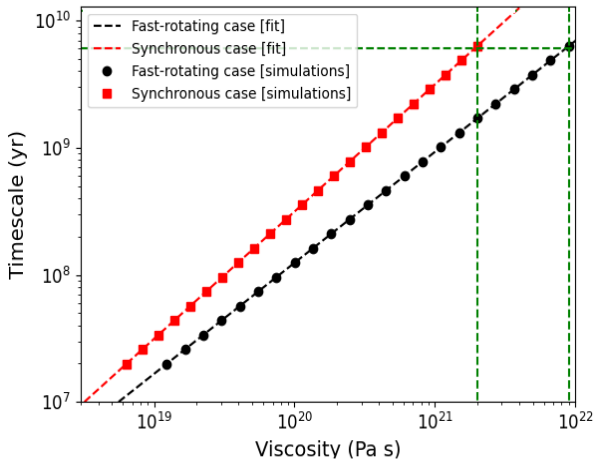


Fig. 2. Timescales of orbital circularization for K2-265 b. The red squares (resp. black dots) are the data obtained from the numerical integrations employing the secular code for the initially synchronous (resp. fast-rotating) planet case. The red (resp. black) dashed curves are the corresponding least-square fittings of the results coming from the secular code experiments. The green dashed vertical line on the left (resp. right) is the lower value of the viscosity for which we can reproduce the planet’s current range of eccentricity values for the initially synchronous (resp. fast-rotating) planet case, with $\tau = \tau_{\text{circ}} = 6.7$ Gyr.

coefficient multiplying the expression for de/dt (see e.g., Ballard et al. 2014 and references therein), we define τ_{circ} as the time it would take for a planet with an initial eccentricity of $e_0 = 0.4$ to reach a current eccentricity which is smaller than 10^{-3} . We emphasize that the choice of the value of $e_0 = 0.4$ is arbitrary and that we have tested other scenarios considering different values of e_0 and verified that such a parameter does not play an important role in the results for τ_{circ} , since the orbital circularization process becomes slower for the small-eccentricity regime.

Figure 2 shows the timescale-viscosity relations resulting from our tidal evolution numerical experiments. The black (resp. red) curve shows the results for the initially fast-rotating (resp. synchronous) planet scenario. The corresponding mathematical relations between η and τ_{circ} are

$$\eta_{\text{FR}} = (5.3 \times 10^{10}) \tau_{\text{circ}}^{1.15}, \quad (14)$$

$$\eta_{\text{S}} = (3.2 \times 10^{11}) \tau_{\text{circ}}, \quad (15)$$

where η_{FR} (resp. η_{S}) is the viscosity for the initially fast-rotating (resp. synchronous) planet case (see black and red curves in Fig. 2).

From the results shown in Fig. 2, we estimate that a viscosity on the order of 10^{22} Pa s or higher is needed for the current eccentricity of the planet to be within the limits estimated by Lam et al. (2018) (i.e., for $0.005 \leq e \leq 0.15$), supposing that the system’s age is on the order of 6–12 Gyr (see green dashed lines in Fig. 2). This viscosity value is in agreement with the recent estimations of Bolmont et al. (2020a) for homogeneous rocky Earth-like planets.

By propagating the eccentricity and age uncertainties to the viscosity estimation presented here, we conclude that the minimum value of the planet’s uniform viscosity is $\eta_{\text{min}} \approx 2 \times 10^{21}$ Pa s, where η_{min} is the viscosity value for which the planet would have a current eccentricity of 0.005 considering an age of 6.7 Gyr. Although an estimation of the maximum viscosity value of the planet is not possible since any scenario with $\eta > 10^{22}$ Pa s could lead to a current eccentricity between 0.005 and 0.15, we note that recent estimations of the viscosity in planetary interiors do not exceed approximately 10^{24} Pa s, and such a threshold value is only attained for very high-pressure regimes in the interior of low-mass planets (see Tobie et al. 2019, Table 2).

Finally, we would like to mention that the differences in the exponents of τ_{circ} (see Eqs. (14) and (15)) is a consequence of the fact that the tidal response of the body depends on the forcing frequency of the tidal interaction, the latter being defined as $\chi_{lmpq} = |(l - 2p + q)n - m\Omega|$ (see e.g., Efroimsky 2012; Tobie et al. 2019). Since in the initially synchronous scenario the forcing frequency is, approximately, constant throughout the entire orbital evolution process, we expect a linear relationship between the timescale and the viscosity. However, in the initially fast-rotating case, the rotational evolution of the planet leads to the excitation of different terms of the tidal forcing frequencies which have different amplitudes, thus leading to a nonlinear relationship between the timescale of orbital circularization and the viscosity of the planet.

3.3. The TTVs

In this section, we investigate the TTVs for K2-265 b, where we analyze the influence of tidal interactions as well as other potentially significant effects such as general relativity (henceforth referred to as GR) and stellar rotation. To that end, we employed the Posidonius code, where the creep tide was implemented following the equations presented in the previous section. For the sake of clarity, we separate the analyses into several subsections to discuss the influence of tuning different parameters individually. With the exception of the subsection aimed at discussing the influence of tuning the uniform viscosity coefficient, we considered $\eta = 10^{22}$ Pa s in all other simulations. Such a value is consistent with both our orbital circularization timescales and recent estimations of the viscosity in planetary interiors (e.g., silicate mantles with pressure values of $P > 25$ GPa and the shear to bulk moduli ratio of μ/K between 0.63 and 0.90 P/K, see Tobie et al. 2019; Bolmont et al. 2020a).

3.3.1. Interplay between apsidal precession and orbital decay

The first aspect to be discussed regarding the TTVs is the relative contribution of orbital decay and apsidal precession. First, we recall the expressions for the transit timings supposing two cases: (i) a circular orbit undergoing orbital decay at rate da/dt and (ii)

an eccentric orbit undergoing apsidal precession at rate $d\omega/dt$. The expression for the transit timing in the first case reads as follows (see e.g., [Ragozzine & Wolf 2009](#))

$$t_{\text{tra}}(N) = t_0 + NP + \frac{N^2}{2} \left[\frac{6\pi^2 a^2}{G(M+m)} \right] \left(\frac{da}{dt} \right), \quad (16)$$

where P is the mean orbital period of the planet.

For the second case, we have, to third-order expansion in the eccentricity (see [Giménez & Bastero 1995](#); [Ragozzine & Wolf 2009](#) for higher-order expansions),

$$t_{\text{tra}}(N) = t_0 + NP_S + \frac{P_a}{\pi} \left[e(\cos \omega_N - \cos \omega_0) + \frac{3}{8} e^2 (\sin 2\omega_N - \sin 2\omega_0) + \frac{1}{6} e^3 (\cos 3\omega_N - \cos 3\omega_0) \right], \quad (17)$$

where

$$\omega_N = \omega_0 + \frac{d\omega}{dN} N, \quad (18)$$

with t_0 and ω_0 being the time and argument of the periapsis value of the first reported transit, respectively, and N corresponding to the transit number. Furthermore, the parameters P_S and P_a correspond to the sidereal and anomalistic periods, respectively (see e.g., [Patra et al. 2017](#) for more details).

As it can be seen from Eqs. (16) and (17), the contributions coming from apsidal precession and orbital decay to the TTVs have the same dependence on the transit number, that is, both contributions give an N^2 dependence on the TTV curves (to first order in $\cos \omega_N$). To disentangle between the effects of apsidal precession and orbital decay on the TTVs, we compared the TTVs obtained by employing two procedures: (i) the data coming from the numerical experiments using the Posidonius code and (ii) synthetic transit curves, which were generated by employing Eqs. (16) and (17). For the synthetic transit curves using Eqs. (16) and (17), we used the values of $\dot{\omega}$ and \dot{a} ensuing from the Posidonius numerical experiment. In the case of a K2-265 b with $e=0.15$ and $\Omega=n$, for instance, we have $\dot{\omega}=0.046 \text{ deg yr}^{-1}$ and $\dot{a}=-1.91 \times 10^{-11} \text{ AU yr}^{-1}$. We would like to mention that in order to investigate the contribution of the apsidal precession to the TTVs, we included the effects of general relativity and stellar rotation in addition to tidal interaction. We verified that the most significant contribution to $\dot{\omega}$ comes from general relativity, which accounts for approximately 93% of the total value of $\dot{\omega}$. Stellar rotation accounts for approximately 6% of the value of $\dot{\omega}$ (considering the smallest possible rotation period for the star according to [Lam et al. 2018](#) and a stellar k_2 of 0.1) and planetary tides account for approximately 1%. Stellar tides play the least important role, contributing less than 1% to $\dot{\omega}$.

Figure 3 shows the results coming from two experiments: one simulation carried out considering only tidal interactions (panel on the left) and one simulation considering general relativity, rotation, and tidal interactions (panel on the right). The contribution of tidally induced orbital decay to the TTVs were filtered out of the orange curve in the right panel of Fig. 3 by directly removing the TTVs generated using Eq. (16). The total integration time was 2 yr, corresponding to approximately 307 transit events for K2-265 b. For the case on the left, we verified that the synthetic curve generated using Eq. (16), which corresponds to the blue curve, gives a TTV amplitude on the order

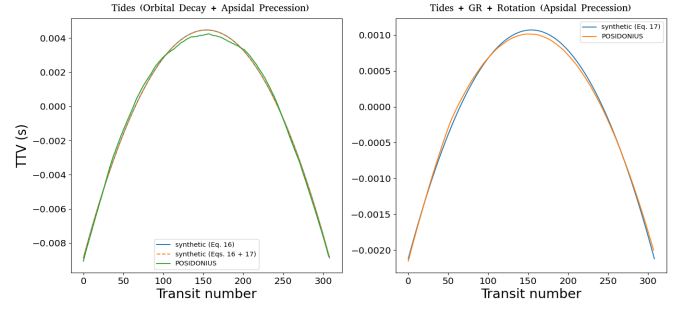


Fig. 3. TTVs for K2-265 b, considering $\eta = 10^{22}$ Pa s, $e = 0.15$, and a synchronous rotation rate for the planet. The results on the *left* were obtained considering only tidal interactions, while the results on the *right* were obtained by considering tides, rotation, and general relativity (the contribution coming from tidal decay to the TTVs on the orange curve were filtered out by directly subtracting the TTVs generated by employing Eq. (16)). The blue curves in the panels are synthetic TTV curves. The green curve in the *left panel* and the orange curve in the *right panel* correspond to the results coming from the Posidonius code.

of 0.012 s; whereas, the synthetic curve generated using only Eq. (17), that is to say considering only the contribution of tidally induced apsidal precession to the TTVs, gives a TTV amplitude of approximately 0.0001 s. The negligible role of tidally induced apsidal precession to the TTVs can be verified by comparing the blue solid curve and the orange dashed curve in the left panel. It can be seen that the addition of tidally induced apsidal precession effects on the TTVs does not significantly change the TTV curve, and the orange and blue curves in the left panel are almost identical. However, general relativity plays a non-negligible role in the TTV, with GR-induced apsidal precession being able to produce a TTV amplitude of approximately 20% of the amplitude obtained by considering the tidally induced orbital decay; we recommend for the readers to compare the green curve in the left panel and the orange curve in the right panel in Fig. 3.

Although general relativity has been shown to be non-negligible in the context of the TTVs, its relevance was analyzed for the case of a synchronous planet with $\eta = 10^{22}$ Pa s and $e = 0.15$. It is highly unlikely for a rocky planet with such viscosity and eccentricity values to be in a synchronous rotation rate scenario. Since tidally induced orbital decay is bigger for nonsynchronous spin-orbit resonant states, we expect that GR becomes negligible when considering other spin-orbit resonances for the planet. We now analyze how these spin-orbit resonances affect the TTVs.

3.3.2. The role of eccentricity and planets' rotation

As it has been discussed in several recent works regarding tidal interactions in rocky bodies, planets with a relatively high viscosity may undergo entrapment in spin-orbit resonances provided that the eccentricity of the planet is bigger than a threshold value and its past rotation was such that $\Omega \gg n$ (e.g., see [Correia et al. 2014](#); [Ferraz-Mello 2015](#) and references therein). Considering the case of the K2-265 b exoplanet with a uniform viscosity of $\eta = 10^{22}$ Pa s, several spin-orbit resonant states are stable if we consider the possible eccentricity values for the planet (namely, $0.005 \leq e \leq 0.15$).

Due to the existence of several stable resonant scenarios, we calculated tidally induced TTVs for the planet for four values of eccentricity, which are within the limit values established by [Lam et al. \(2018\)](#). We also calculated the corresponding spin-orbit stable configurations for each value of eccentricity,

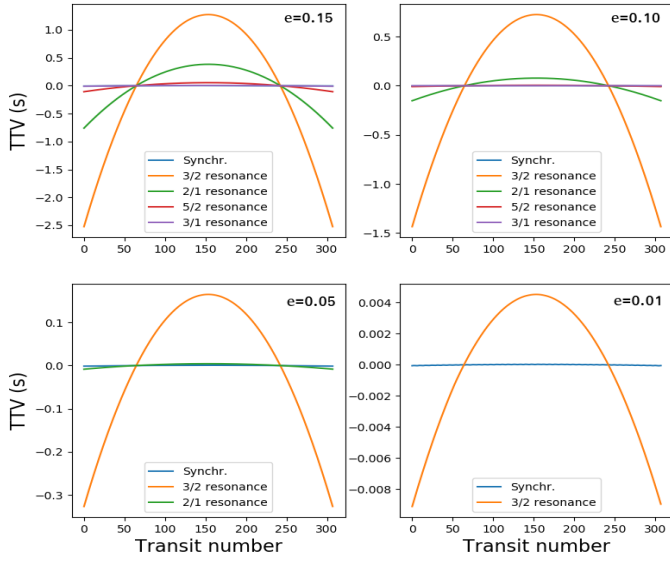


Fig. 4. Tidally induced TTV for a timespan of 2 yr (corresponding to 308 transit events), considering several spin-orbit resonances and four values of eccentricity, as indicated in the top right corner of each panel.

where we mention that increasing the eccentricity value leads to the onset of possible higher-order stable spin-orbit resonant states (for details regarding the determination of stable spin-orbit resonances, see e.g., [Correia et al. 2014](#); [Ferraz-Mello 2015](#); [Gomes et al. 2019](#) and references therein). The results of our analysis are shown in Fig. 4. In the figure, we can deduce both the influence of the eccentricity as well as the rotation rate of the planet on the amplitude of the TTVs (henceforth referred to as $\text{amp}(\text{TTV})$), with

$$\text{amp}(\text{TTV}) = \max(\text{TTV}) - \min(\text{TTV}). \quad (19)$$

By comparing the orange curves in each panel of Fig. 4, it can be seen that the eccentricity value strongly affects the tidally induced TTVs. We verified that $\text{amp}(\text{TTV})$ scales with e^α , where $\alpha = 1, 2$ and 4 for the synchronous, $3/2$ and $2/1$ spin-orbit resonances, respectively. Moreover, α increases monotonically with Ω/n , the latter usually being referred to as the order of the spin-orbit resonance. At this point, it is worth mentioning that the resulting linear dependence of the amplitude of the TTVs with the eccentricity in the synchronous rotating planet case is consistent with the predictions of [Ragozzine & Wolf \(2009\)](#). We did not perform a study regarding the eccentricity dependence of the amplitudes of the TTVs for higher-order spin-orbit resonances (such as the $5/2$ and $3/1$ resonances) since such spin-orbit resonances are only maintained at either high eccentricity values with $e > 0.15$, which are incompatible with the eccentricity estimations of K2-265 b, or very big viscosity values, which are inconsistent with our estimations of Sect. 3.2. Another aspect which can be seen from Fig. 4 by comparing, for instance, the curves in the top left panel is that tidally induced TTVs are negligible for the synchronous rotation and high-order spin-orbit resonant states (e.g., the $5/2$ and $3/1$ resonances) when compared to the $3/2$ and $2/1$ resonances (see orange and green curves in each panel).

3.3.3. Impact of the uniform viscosity coefficient

Although the combination of eccentricity and age estimations of the system has allowed for a good estimation of the planet's

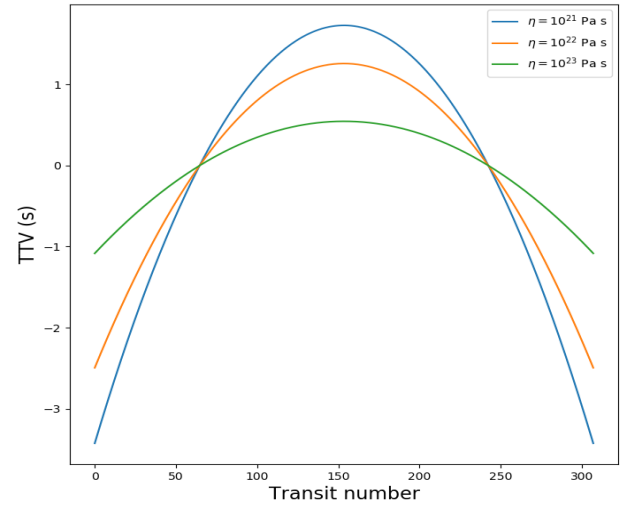


Fig. 5. Effect of the viscosity value on the tidally induced TTV for K2-265 b with $e = 0.15$, $\Omega/n = 1.5$, and a total transit number of 2 yr. We considered variations of η between the minimum value coming from eccentricity evolution timescale estimations and the maximum value coming from the reference values of [Tobie et al. \(2019\)](#), which were obtained by solving the internal structure equations for the mantle of planets composed by high-pressure silicates.

viscosity, we must analyze the influence of tuning the viscosity value of the planet on the tidally induced TTVs since the viscosity of the planet was estimated with a given uncertainty. For that purpose, we consider viscosity values within the uncertainties discussed in the Sect. 3.2.

Figure 5 shows the TTVs curves for three numerical experiments where we tuned the viscosity value of the planet. We can see that the viscosity is the parameter playing the least important role when compared to the influence of the eccentricity and rotation rate on the amplitudes of the tidally induced TTVs. In Fig. 5, it can be seen that by increasing the viscosity by a factor of 100, the amplitude of the tidally induced TTVs decreases by a factor of approximately 3. The influence of the viscosity value on the TTV amplitude is even weaker for higher-order spin-orbit resonances, as it was verified by some numerical experiments for the $2/1$ and $5/2$ spin-orbit resonances.

3.4. Conditions for potentially observable TTVs

Since we have analyzed the dependency of the tidally induced TTVs with the parameters of the K2-265 system carrying the biggest uncertainties, we can now establish for which conditions we would have the biggest amplitude of tidally induced TTVs (i.e., the scenarios leading to the most easily detectable tidally induced TTVs with the smallest amount of transit data). Figure 6 shows the results concerning such an analysis for the specific case of the $3/2$ spin-orbit resonant state, which is the resonant state presenting the biggest TTVs. The curves in the graph give the eccentricity and transit number values leading to the corresponding amplitudes of the TTVs (see labels in the upper right corner of the figure). The dashed brown line corresponds to the maximum value of the eccentricity of K2-265 b estimated by [Lam et al. \(2018\)](#).

From the results shown in Fig. 6, we can conclude that approximately 6 yr (corresponding to approximately 1000 transit events) of transit data would be necessary for a TTV amplitude on the order of 30 s to be obtained, considering that the planet's eccentricity value is the maximum possible value corresponding

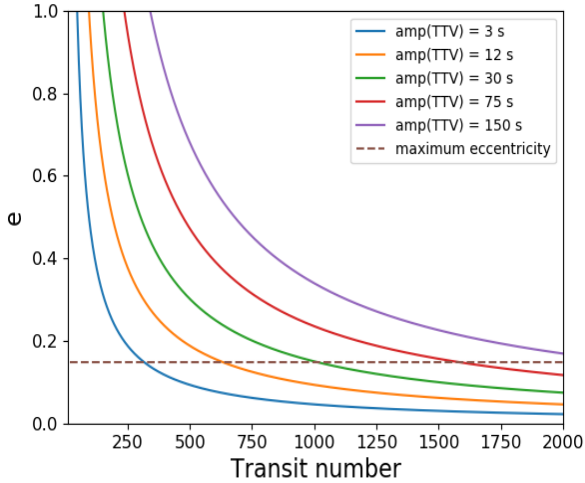


Fig. 6. Relation between eccentricity and transit number giving the amplitudes of TTVs indicated in the labels. In all cases, we considered the 3/2 spin-orbit resonance, which gives the highest amplitudes of the TTVs when compared to all the other rotational configurations. The maximum transit number shown in the figure (i.e., 2000 transits) corresponds to approximately 13 yr of transit events. More discussions are presented in the main text.

to the estimations of Lam et al. (2018). However, if a precision of approximately 10 s for transit measurements is achieved, which is the case for the TRAPPIST-1 system (see discussions in Bolmont et al. 2020b; Agol et al. 2021), we predict that approximately 3.5 yr of transit data would suffice to identify tidally induced TTVs. The follow-up of transit photometry data in the future would then be an essential tool to experimentally identify such effects.

It is worth mentioning that we performed some numerical experiments to evaluate TTVs induced by the stellar tide as well as the stellar flattening resulting from the stellar rotation, where the stellar rotation period of 32.2 days was used in our simulations, following Lam et al. (2018). It was verified that these effects are much smaller than tidally induced TTVs by the planet even in the case of a homogeneous star (i.e., with a fluid Love number of $k_t = 3/2$). An analysis of the influence of the general relativity on the induced TTVs was also performed. We also verified that these effects are negligible when compared to the planetary tidally induced TTVs.

Although the results presented in this section show that the follow-up of transit data for the K2-265 b could potentially lead to observable TTVs in the near future, we now perform a broad exploration of the tidally induced TTVs as a function of the system's orbital and physical parameters to have a more comprehensive view of the most important parameters influencing the TTVs.

4. Broad exploration of the parameters space

In the previous section, we have analyzed tidally induced TTVs for the K2-265 system and concluded that, with the current amount of available data, it is not yet possible to detect tidally induced TTVs. In this section, we explore the influence of other parameters on the values of the tidally induced TTVs with the goal to determine for which exoplanetary systems we would be able to detect such effects with a smaller amount of transit data.

Figure 7 shows the results regarding the exploration of the tidally induced TTVs as a function of four parameters (semi-major axis, planet mass, planet radius, and stellar mass; see

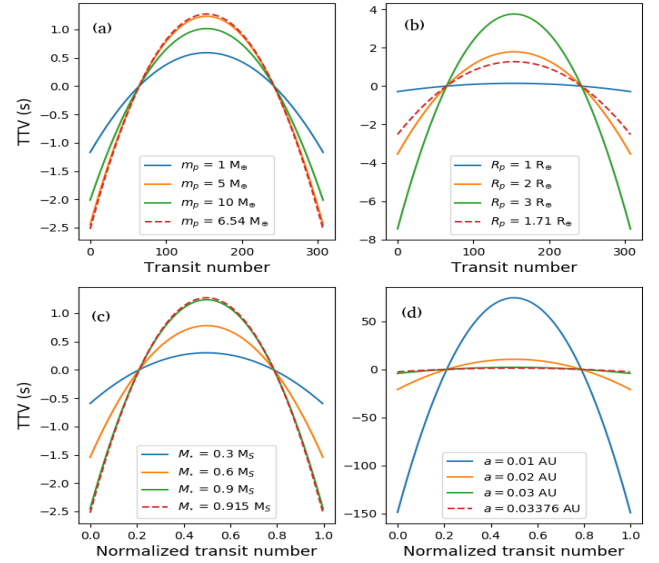


Fig. 7. Broad exploration of the TTV as a function of four parameters: (a) planetary mass, (b) planetary radius, (c) stellar mass, and (d) semi-major axis values. We considered a total timespan of 2 yr in all the simulations. In each panel of the figure, we tuned each parameter individually and considered the nominal values of the K2-265 b system for the remaining ones (see Table 2). Moreover, in all cases shown here, we considered a 3/2 spin-orbit resonant state for the planet as well as an eccentricity of 0.15 in order to maximize the effects of the TTVs.

labels and caption of Fig. 7). In all panels, the dashed red line corresponds to the case of the K2-265 b planet using the parameters of Table 2. For the bottom panels, we used the normalized transit number to perform the plots since changing the stellar mass and semi-major axis leads to considerable differences in the orbital period, which in turn causes alterations in the total transit number, even though the total time of evolution remains the same (namely, 2 yr). We can clearly see that the most important parameters influencing the amplitudes of the TTVs are the stellar mass and the semi-major axis (see panels c and d in the figure). The planetary radius value also strongly affects the amplitude of the TTVs. However, since super-Earths are believed to have radii between 1 and 1.8 Earth radii, according to recent discussions (see e.g., Fulton et al. 2017), the experiments performed in panel b for $R_p = 2 R_\oplus$ and $R_p = 3 R_\oplus$ (see orange and green curves) are merely exploratory.

The factor playing the least important role in the TTVs is the planetary mass. Tuning this type of parameter by a factor of 10 leads to a difference in the TTVs of a factor of 3. Moreover, we emphasize that changing the planetary mass leads to a direct change in the relaxation factor value since the planetary mass directly affects the planet mean density value (see Eq. (12)) and its mean equatorial prolateness. Thus, the influence of tuning the planetary mass on the tidally induced TTVs is much more complex than the influences of the other three factors which were considered in this section, and a proportionality relation between the amplitude of the TTVs and the tuning of the planetary mass may not be possible (see orange and green curves in panel a of Fig. 7).

5. Discussions

In this section, we discuss several aspects of the results obtained in Sects. 3 and 4. For the sake of clarity, the discussions are separated into subsections.

5.1. TTVs for K2-265 b

Regarding our numerical experiments of the TTVs for K2-265 b, we verified that the most important factors ruling the amplitudes of the TTVs are the eccentricity and spin-orbit resonance. Regarding the spin-orbit resonance influence on TTVs, we verified that although synchronous rotation leads to small-amplitude TTVs, planets in low-order spin-orbit resonances (especially the 3/2 and 2/1 resonances) may present relatively high amplitudes of tidally induced TTVs, where the main component causing the tidally induced TTVs for nonsynchronous rotation cases is the orbital decay of the planet. Other effects such as tidally induced apsidal precession and GR-induced apsidal precession were verified to produce TTVs two to three orders of magnitude smaller than the TTVs caused by tidally induced orbital decay. The uniform viscosity coefficient was shown to cause a relatively small variation in the amplitudes of TTVs when compared to the effects of tuning the rotation and eccentricity values.

In what concerns the predictions for future TTVs considering more transit data, we have shown that tidally induced TTVs may be able to cause deviations of transit timings on the order of 30–70 s, considering a 10-yr timespan. These results indicate that tides can be an important source of additional TTVs which are to be included when modeling transit data using a longer baseline in the case of close-in planetary systems.

5.2. Potential confusion with other effects generating TTVs

As it has already been discussed in Sect. 3, the TTVs induced by tidal interactions are much more significant when the planet is trapped in a nonsynchronous spin-orbit resonance, where the main component being responsible for the TTVs is the orbital decay of the planet. However, when the planet is trapped in a synchronous rotation, the TTV induced by orbital decay is less significant, and the TTV induced by the apsidal precession has a non-negligible role in the total TTV. The most significant effect causing apsidal precession-induced TTVs is the GR, with $\dot{\omega}^{(GR)}$ being at least one order of magnitude bigger than any other effects causing apsidal precession.

Although GR has been shown to play a non-negligible role in the TTVs only in the case of synchronous rotation, it is possible that GR and tides provide the same effects on TTVs if the mass and radius of the planet under study lead to relatively small tidally induced TTVs. In such specific cases, the interplay between GR and tides and their influences on the light curves of exoplanets can be studied by analyzing occultation curves as well as transit curves. As it has been discussed by Patra et al. (2017) and Yee et al. (2020), for example, the shape of the timing variation curves of transits and occultations differ when considering the contributions of apsidal precession and orbital decay. Figure 8 shows an example of occultation timing variation (OTV) curves, corresponding to a homogeneous K2-265 b on a synchronous rotation rate regime with $e = 0.15$ and $\eta = 10^{22}$ Pa s.

Analyzing the contributions coming from orbital decay and apsidal precession to the OTVs shown in Fig. 8, we can see that the occultations provide a way to disentangle between these effects when they have comparable contributions to the timing variations. We emphasize that the use of occultation timing analysis to disentangle between apsidal precession and orbital decay-induced timing variations has already been employed in Yee et al. (2020) to confirm the orbital decay of WASP-12 b, and we briefly present the curves in Fig. 8 to show that tidal interactions and GR can be analyzed separately if occultation data are available (i.e., there is no confusion between the two

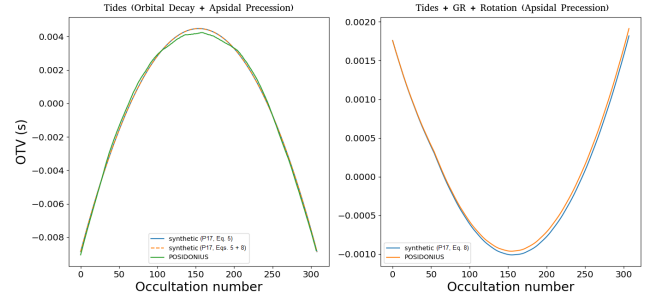


Fig. 8. Occultation timing variations considering the same simulations of Fig. 3, i.e., a K2-265 b with $e = 0.15$, a synchronous rotation rate, and a viscosity of $\eta = 10^{22}$ Pa s. The *panel on the left* shows the contribution of orbital decay and tidally induced apsidal precession to the OTVs, while the *panel on the right* shows the contribution of apsidal precession induced by three effects to the OTVs (i.e., for the latter, the effects of GR, tides, and rotation were considered). The synthetic OTV curves were generated by considering Eqs. (5) and (8) given in Sect. 4 of Patra et al. (2017), corresponding to P17 in the labels of the figure.

contributions if both transits and occultation curves are available). However, we emphasize that the only case for which apsidal precession can have a non-negligible effect on the timing curves corresponds to a synchronous rotation, in which case the orbital decay rate is much smaller when compared to nonsynchronous resonant states. In such a specific case, model comparison tools, such as the analysis of the Bayesian information criterion (see discussions in Patra et al. 2017 and Yee et al. 2020), have to be employed to choose between models with different numbers of free parameters (e.g., a model considering a fixed orbital decay rate and a model considering an eccentric orbit with fixed values for the apsidal precession rate and argument of periapsis).

5.3. Broad exploration of parameters space

The analysis performed in Sect. 4 regarding the broad exploration of tidally induced TTVs as a function of both planetary and stellar parameters has allowed for the conclusion that the main components leading to significant changes in TTV amplitudes are the stellar mass, planetary radius, and semi-major axis. The planetary mass has been shown to present little influence on the amplitudes of the tidally induced TTVs. Moreover, the results presented in Sect. 4 show that the most promising planetary systems for which tidally induced TTVs would be detectable are the ones for which the orbital period is on the order of 2 days or less, and in which the planet can have a moderate eccentricity on the order of 0.1 or higher, thus allowing for nonsynchronous spin-orbit resonant states to be maintained until the present, thus enhancing the amplitude of tidally induced TTVs when compared to the synchronous rotation rate case.

We emphasize that all calculations presented in this work for the tidally induced TTVs considered that the planet adjusts to hydrostatic equilibrium following a Newtonian creep equation for its shape evolution. We also neglected forced librations of the rotation rate by considering the constant rotation rate approximation of the creep tide theory⁴. Considering that the planet has permanent components of the flattenings as a consequence of, for example, reorientation or despinning (see e.g., Matsuyama & Nimmo 2008, 2009), this may lead to even

⁴ For planets trapped in spin-orbit resonances, forced librations can have an important role on the tidal heating of the planets (see e.g., discussions in Efroimsky 2018; Correia & Delisle 2019).

bigger TTVs⁵. Detecting these permanent shape-induced TTVs may be essential at characterizing planetary interior structures as well as studying their past orbital and rotational configuration.

6. Conclusion

The most important findings of this work regard the analysis of the tidally induced TTVs for nonsynchronous spin-orbit resonant states. For a given eccentricity value, nonsynchronous spin-orbit resonances lead to a faster tidally induced orbital evolution process when compared to synchronous rotation rate cases. As a consequence, planets in nonsynchronous spin-orbit resonances migrate faster and may present larger TTVs than the ones generally predicted by employing classical expressions to calculate the orbital decay rate induced by tides; we refer to classical expressions as the ones generally based on the CTL model, which assumes that the only possible equilibrium rotation state is pseudo-synchronism. Moreover, we have discussed that when occultation timing data are available in addition to transit timing data, the potential degenerescence of tidal interactions with other effects inducing timing variations (such as general relativity and stellar rotation) can be broken by analyzing the occultation timing variations. We also emphasize that in all cases of nonsynchronous rotation, the orbital decay-induced TTV is at least 2 orders of magnitude bigger than the apsidal precession-induced TTV.

Another discussion that ensued from this work is the possibility of the future detection of tidally induced TTVs caused by orbital decay for other exoplanetary systems containing a close-in rocky planet with a non-negligible eccentricity. A quick estimation of the tidally induced TTVs as a function of the semi-major axis in the case of a moderately eccentric planet (with $0.1 < e < 0.2$) in the $3/2$ spin-orbit resonance allows us to conclude that, for planets with $a \leq 0.02$ AU, an amplitude of the tidally induced TTVs on the order of 20–80 s may be reached even for small observation timescales (on the order of 2–3 yr), provided that the stellar mass is between 0.5 and 1.0 Solar masses. Some of the (putative) single-planet systems in which the planet satisfies such a semi-major axis criterion include, for instance, LHS-3844 b (Vanderspek et al. 2019) and L 168-9 b (Astudillo-Defru et al. 2020). Since very close-in planets are believed to have small eccentricities due to tidally induced orbital circularization processes, the search for the detection of tidally induced TTVs for Earth-like rocky planets may be more advantageous for planetary systems with at least one more planetary companion. In this case, eccentricity excitation as a consequence of planet-planet gravitational interactions could lead to moderate eccentricities for the inner planet. Consequently, nonsynchronous spin-orbit resonances may be maintained until the present. Some of the multiplanet systems which can present this configuration are K2-38 b-c (Sinukoff et al. 2016; Toledo-Adrón et al. 2020), LTT 3780 b-c (Nowak et al. 2020; Cloutier et al. 2020), and TRAPPIST-1 (Gillon et al. 2017). The new version of the Posidonius code introduced in this work, which has been shown to provide stable and precise

⁵ To take permanent components of the flattenings into account, a different implementation of tidal interactions must be used. In the frame of the creep tide, for instance, we would have to solve three additional first-order differential equations, dictating the shape evolution of the body instead of supposing the constant rotation rate approximation, which automatically neglects forced librations of the rotation rate (see e.g., discussions in Folonier et al. 2018; Gomes et al. 2019).

results, can thus be a powerful tool for studying the cases of these multiplanetary systems, for which analytical formulations of the transit and occultation timings may not be able to capture all the aspects of planet-planet perturbations.

Acknowledgements. The authors would like to thank the anonymous referee for helping improving the manuscript. G.O.G would like to thank FAPESP for funding the project under grants 2016/13750-6, 2017/25224-0 and 2019/21201-0, and David Nesvorný for a fruitful discussion about TTVs. This work has been carried out within the framework of the NCCR PlanetS supported by the Swiss National Science Foundation. This research has made use of NASA's Astrophysics Data System.

References

- Agol, E., Steffen, J., Sari, R., & Clarkson, W. 2005, *MNRAS*, 359, 567
 Agol, E., Dorn, C., Grimm, S. L., et al. 2021, *Planet. Sci. J.*, 2, 1
 Astudillo-Defru, N., Cloutier, R., Wang, S. X., et al. 2020, *A&A*, 636, A58
 Ballard, S., Chaplin, W. J., Charbonneau, D., et al. 2014, *ApJ*, 790, 12
 Blanco-Cuaresma, S., & Bolmont, E. 2017, in EWASS Special Session 4 (2017): Star-planet interactions (EWASS-SS4-2017)
 Bolmont, E., Breton, S. N., Tobie, G., et al. 2020a, *A&A*, 644, A165
 Bolmont, E., Demory, B. O., Blanco-Cuaresma, S., et al. 2020b, *A&A*, 635, A117
 Cloutier, R., Eastman, J. D., Rodriguez, J. E., et al. 2020, *AJ*, 160, 3
 Correia, A. C. M., & Delisle, J.-B. 2019, *A&A*, 630, A102
 Correia, A. C. M., Boué, G., Laskar, J., & Rodríguez, A. 2014, *A&A*, 571, A50
 Delisle, J. B., Correia, A. C. M., Leleu, A., & Robutel, P. 2017, *A&A*, 605, A37
 Efroimsky, M. 2012, *ApJ*, 746, 150
 Efroimsky, M. 2018, *Icarus*, 306, 328
 Ferraz-Mello, S. 2013, *Celest. Mech. Dyn. Astron.*, 116, 109
 Ferraz-Mello, S. 2015, *Celest. Mech. Dyn. Astron.*, 122, 359
 Folonier, H. A., Ferraz-Mello, S., & Andrade-Ines, E. 2018, *Celest. Mech. Dyn. Astron.*, 130, 78
 Fressin, F., Torres, G., Charbonneau, D., et al. 2013, *ApJ*, 766, 81
 Fulton, B. J., Petigura, E. A., Howard, A. W., et al. 2017, *AJ*, 154, 109
 Gillon, M., Triard, A. H. M. J., Demory, B.-O., et al. 2017, *Nature*, 542, 456
 Giménez, A., & Bastero, M. 1995, *Ap&SS*, 226, 99
 Gomes, G. O., Folonier, H. A., & Ferraz-Mello, S. 2019, *Celest. Mech. Dyn. Astron.*, 131, 56
 Haswell, C. A. 2018, *WASP-12b: A Mass-Losing Extremely Hot Jupiter*, eds. H. J. Deeg, & J. A. Belmonte (Berlin: Springer), 97
 Hebb, L., Collier-Cameron, A., Loeillet, B., et al. 2009, *ApJ*, 693, 1920
 Hernandez, D. M., & Dehnen, W. 2017, *MNRAS*, 468, 2614
 Lam, K. W. F., Santerne, A., Sousa, S. G., et al. 2018, *A&A*, 620, A77
 Lithwick, Y., Xie, J., & Wu, Y. 2012, *ApJ*, 761, 122
 Love, A. E. H. 1911, *Some Problems of Geodynamics* (Cambridge: Cambridge University Press)
 Makarov, V. V., & Efroimsky, M. 2013, *ApJ*, 764, 27
 Matsuyama, I., & Nimmo, F. 2008, *Icarus*, 195, 459
 Matsuyama, I., & Nimmo, F. 2009, *J. Geophys. Res. Planets*, 114, E01010
 Mayor, M., Pepe, F., Queloz, D., et al. 2003, *The Messenger*, 114, 20
 Mignard, F. 1979, *Moon and Planets*, 20, 301
 Nesvorný, D., & Morbidelli, A. 2008, *ApJ*, 688, 636
 Nesvorný, D., & Vokrouhlický, D. 2016, *ApJ*, 823, 72
 Nowak, G., Luque, R., Parviainen, H., et al. 2020, *A&A*, 642, A173
 Patra, K. C., Winn, J. N., Holman, M. J., et al. 2017, *AJ*, 154, 4
 Pedregosa, F., Varoquaux, G., Gramfort, A., et al. 2011, *J. Mach. Learn. Res.*, 12, 2825
 Ragozzine, D., & Wolf, A. S. 2009, *ApJ*, 698, 1778
 Rein, H., & Spiegel, D. S. 2015, *MNRAS*, 446, 1424
 Rein, H., & Tamayo, D. 2015, *MNRAS*, 452, 376
 Rodríguez, A., Callegari, N., & Correia, A. C. M. 2016, *MNRAS*, 463, 3249
 Sinukoff, E., Howard, A. W., Petigura, E. A., et al. 2016, *ApJ*, 827, 78
 Sullivan, P. W., Winn, J. N., Berta-Thompson, Z. K., et al. 2015, *ApJ*, 809, 77
 Tobie, G., Grasset, O., Dumoulin, C., & Mocquet, A. 2019, *A&A*, 630, A70
 Toledo-Adrón, B., Lovis, C., Suárez Mascareño, A., et al. 2020, *A&A*, 641, A92
 Vanderspek, R., Huang, C. X., Vanderburg, A., et al. 2019, *ApJ*, 871, L24
 Walterová, M., & Běhoučková, M. 2020, *ApJ*, 900, 24
 Yee, S. W., Winn, J. N., Knutson, H. A., et al. 2020, *ApJ*, 888, L5
 Youdin, A. N. 2011, *ApJ*, 742, 38

Appendix A: Code verification and performance

The Posidonius code considers the effects of additional forces other than N -body point-mass interactions by directly implementing the contribution of these effects in the force components acting on each body of a given system. Both a symplectic integration scheme with a fixed time-step (WHFast integrator) and an integrator with a variable time-step integration scheme (IAS15) are available for use in the code.

To test the proper functioning of the implementation of the creep tide theory in the Posidonius code, we compared the results coming from it with the ones coming from the use of a secular code giving the spin-orbit evolution of the body. The equations for the secular evolution are

$$\dot{a} = \frac{R^2 n \bar{\epsilon}_p}{5a} \sum_{k \in \mathbb{Z}} \left[3(2-k) \frac{\gamma(\nu + kn) E_{2,k}^2}{\gamma^2 + (\nu + kn)^2} - \frac{\gamma k^2 n E_{0,k}^2}{\gamma^2 + k^2 n^2} \right], \quad (\text{A.1})$$

$$\dot{e} = -\frac{3GMR^2 \bar{\epsilon}_p}{10na^5 e} \sum_{k \in \mathbb{Z}} \left[P_k^{(1)} \frac{\gamma(\nu + kn) E_{2,k}^2}{\gamma^2 + (\nu + kn)^2} + \frac{P_k^{(2)}}{3} \frac{\gamma k^2 n E_{0,k}^2}{\gamma^2 + k^2 n^2} \right], \quad (\text{A.2})$$

$$\dot{\Omega} = -\frac{3GM\bar{\epsilon}_p}{2a^3} \sum_{k \in \mathbb{Z}} \frac{\gamma(\nu + kn) E_{2,k}^2}{\gamma^2 + (\nu + kn)^2}, \quad (\text{A.3})$$

where $\nu = 2\Omega - 2n$ is the semidiurnal frequency of the primary, the coefficients P_k are eccentricity-dependent coefficients given by

$$P_k^{(1)} = 2\sqrt{1-e^2} - (2-k)(1-e^2), \quad (\text{A.4})$$

$$P_k^{(2)} = 1 - e^2, \quad (\text{A.5})$$

and the coefficients $E_{q,k}$ are the eccentricity-dependent Cayley coefficients. We can see that no short-period components exist (i.e., components depending on the true or mean anomaly), since they were already averaged out.

Figure A.1 shows an example of the results of three simulations considering the spin and orbit evolution of a homogeneous K2-265 b with a viscosity of $\eta = 10^{17}$ Pa s; the choice to consider such a value for η relies on the fact that lower values of η lead to bigger amplitudes of the short-period oscillations of Ω , thus representing the best scenario for identifying potential changes introduced by the averaging of the equations of motion, which are performed in the frame of the secular model.

We can see several characteristics which are classic of tidal evolution scenarios in Fig. A.1: firstly, the rotation of the planet is damped to a 2/1 spin-orbit resonant state. This process is followed by orbital shrinking and eccentricity damping until the 2/1 spin-orbit resonance is no longer stable. The rotation then evolves to the 3/2 spin-orbit resonance while the eccentricity and semi-major axis continue to decrease; we emphasize that the evolution of the orbit takes place on a timescale that is much bigger than the evolution of the rotation. The endpoint of tidal evolution is achieved when both orbital circularization and rotational synchronization take place. We can see that the values of the orbital elements at the endpoint of the tidal evolution are

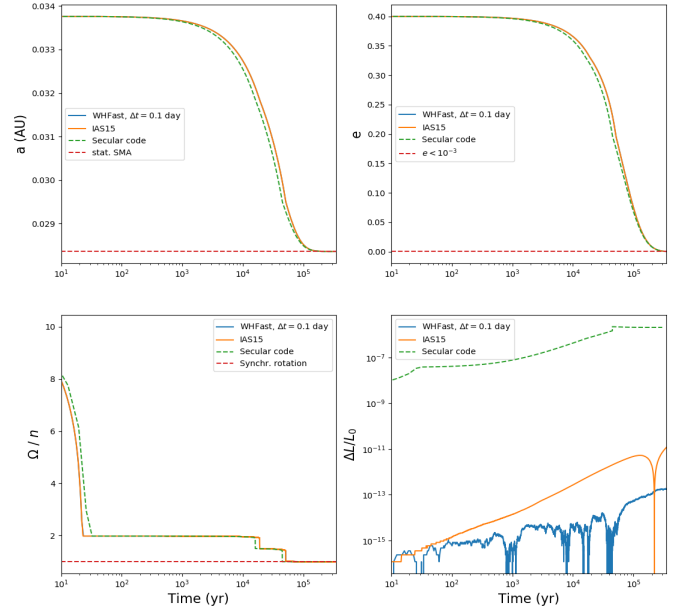


Fig. A.1. Semi-major axis, eccentricity, rotation, and angular momentum evolution of four simulations (see the labels in the panels). Solid lines correspond to simulations using the Posidonius code, and the green dashed line corresponds to the simulation using the secular code. The red dashed line shown in the panels of the orbital and rotational evolution of the planet corresponds to the predictions of the final values of the spin-orbit configuration of the planet, based on total angular momentum conservation.

in very good agreement with the analytical estimations coming from the angular momentum conservation of the system, namely $a_{\text{stat}} = a_0(1 - e_0^2)$ (see red dashed curve in the top panel on the left in Fig. A.1).

From the point of view of angular momentum conservation, we can see that the Posidonius code conserves it with a much better precision when compared to the secular code (see bottom panel on the right in Fig. A.1). Additionally, we verified that the WHFast code better conserves the angular momentum for a sufficiently long timescale, whereas the IAS15 integrator gives more precise results for short-term evolution scenarios. Lastly, we comment that the speed of integration is much slower for the IAS15 when compared to the WHFast integrator. The ratio of time taken to evolve the orbits with the IAS15 and WHFast integrators is approximately 25, which is an expected difference in integration time given the adaptative time-step scheme of the IAS15 integrator. We note that the value of the constant time-step chosen for the WHFAST was set so that it would be near the mean value of the time-step chosen by the adaptative time-step algorithm of the IAS15 integrator (for the latter case, we verified that the time-step oscillated between 0.08 and 0.13 days for the simulation shown in Fig. A.1). We also performed some experiments by tuning the time-step of the WHFast integrator and verified that the results obtained by considering a time-step smaller than 0.1 days do not change when compared to the case in which the time-step was chosen to be 0.1 days (i.e., the case corresponding to the blue curve in Fig. A.1). For a more comprehensive discussion on the precision and error analyses for symplectic integrators, see [Hernandez & Dehnen \(2017\)](#).

Conclusion

In this thesis, we presented several applications of the creep tide theory to study the spin and orbital evolution of Solar System bodies and exoplanetary systems. The thesis was thus focused on providing the essential equations for computing the time evolution of the spin and orbital parameters, without extensive theoretical developments of the creep tide theory. For each application we considered, different approximations of the creep tide were used and we pointed out which are the limits of applicability of each formulation (e.g., the pseudo-synchronous approximation or the constant rotation rate approximation). The theoretical aspects used in the applications were thus based on other previous works, mainly the works of Folonier et al. (2018); Gomes et al. (2019); Gomes and Ferraz-Mello (2020); Ferraz-Mello et al. (2020).

For the application we performed to Mercury, we focused on the study of the planet's rotation and figure evolution. We studied the dependence of the equilibrium spin-orbit resonant states with the eccentricity value. Since we know that Mercury's current rotation rate is entrapped in the 3/2 spin-orbit resonance, we were able to establish some constraints to Mercury's relaxation factor value. Using the value found for Mercury's relaxation factor to analyse its shape evolution leads to a discrepancy in the values observed for the equatorial prolateness and polar oblateness with respect to the corresponding values predicted by the creep tide theory by approximately 2 orders of magnitude. We have also compared the results of the creep tide theory for the flattenings with the results obtained by other versions of the Darwin theory. Such comparison allowed us to conclude that no theories based on the hydrostatic equilibrium of Mercury are able to reproduce its current values of flattening coefficients. Thus, mechanisms other than tidal interactions are necessary to explain Mercury's current shape.

In what concerns the applications we performed to study exoplanetary systems, we firstly considered an application for the study of the secular evolution of a two-body systems (more specifically, a hot Jupiter orbiting M, K, G and F stars). We considered the effects of both tidal interactions as well as the magnetic wind braking of the stellar rotation. Our results have shown that, for hot Jupiters orbiting M, K and G stars, the magnetic wind braking is a dominant mechanism which significantly slows the stellar rotation and leads to rapid planetary orbital decay. Thus, hot Jupiters are not likely to survive around these stars and it is expected that such systems are relatively young (otherwise, planet engulfment takes place and the planet no longer orbits the star). One special case which presented optimistic scenarios for the hot Jupiter survival is the case of a F host star. In such case, the magnetic wind braking is absent and the stellar rotation evolves only due to tidal interactions. Provided that the initial rotation rate of the star is sufficiently high (of the order 2.3 days of rotation period), the planet can be pushed from an initial orbital configuration for which $P_{\text{orb}} \approx 2$ days to a final configuration with $P_{\text{orb}} \approx 8$ days. We have also verified that estimations of the quality factor of some stars given by Penev et al. (2018) correspond to relaxation factor values that vary between 1 and 100 s^{-1} , with only one outlier for which the relaxation factor exceeds 10^3 s^{-1} .

After the application of the creep tide to study single-planet systems containing hot Jupiters, we considered an application to secularly-evolving exoplanetary systems containing potentially habitable exoplanets. We considered applications to LHS-1140 b-c and K2-18 b-c. For the LHS-1140 b-c exoplanetary system, the results of the study allow us to conclude that the planets are probably in nearly-circular orbits, provided that the value of the relaxation factor of the inner planet is close to the value estimated for the solid Earth, which is $0.9 \times 10^{-7} \text{ s}^{-1} \leq \gamma_{\text{Earth}} \leq 3.6 \times 10^{-7} \text{ s}^{-1}$. Since the eccentricities of the planets are not well constrained from observations, we cannot rule out the possibility that the planets are in eccentric orbits. Thus, we rely on future observations which can better constrain the planetary eccentricities to have more precise and concrete conclusions regarding the planetary relaxation factor values. For the application to the K2-18 b-c exoplanetary system, the current lack of knowledge of the planetary radius and mass value of the inner planet led us to perform an analysis of the scenarios of orbital evolution considering two cases: a rocky Earth-like K2-18 c (hereafter case 1) and a gaseous K2-18 c (hereafter case 2). Combining the analysis of the results considering cases 1 and 2 as well as the estimation

of the eccentricity of K2-18 b, we conclude that the inner planet cannot have a relaxation factor value which is close to the value of the Earth, since such hypothesis is inconsistent with the current eccentricity value of the planets. To conciliate the current eccentricity estimation of K2-18 b with the relaxation factor value of the inner planet, we need to have two specific regimes of values for γ_c . Either γ_c is very small, of the order 10^{-10} s^{-1} , or γ_c is very large, of the order $1 - 10 \text{ s}^{-1}$ (which is a typical value of mini-Neptunes).

Additionally to the applications we considered to study secularly-evolving systems, we considered an implementation of the creep tide equations in the Posidonius N-body code. Such an implementation significantly increases the applicability of the creep tide theory since it allows us to study systems in any configurations (provided that the system is coplanar and the eccentricities are not above 0.4). We have tested the efficiency and consistency of the results by performing two applications. Firstly, we considered a single-planet system, namely K2-265 b. We compared the results of spin-orbit simulations using Posidonius with the results coming from a secular evolution code (which calculates the evolution of the semi-major, eccentricity and rotation rate of the extended body). We also compared the results between the two main integrators currently available in Posidonius: WHFast and IAS15. We verified that the integrators are in very good agreement, as well as with the secular evolution code results. However, we verified that, in terms of computational efficiency, WHFast is approximately 20 times faster than IAS15. The second application we performed considered the CoRoT-7 b-c exoplanetary system, where we explored the scenarios of orbital evolution which could lead to the same eccentricity pumping evolution scenario as the ones described in Rodríguez et al. (2016). We have verified that, since the current eccentricities of the planets are moderate (with $e = 0.12$ for both planets), the planets relaxation factor values cannot be in the range $10^{13} - 10^{17} \text{ Pa s}$. If this was the case, the planets eccentricities would have already been damped to values smaller than 0.01. The current eccentricity values of the planets are more consistent with very small (of the order 10^{10} Pa s) or very large (of the order 10^{19} Pa s) values for the planets viscosities, which is consistent with the results presented in Rodríguez et al. (2016). In both these cases, the eccentricity mechanism takes place and causes eccentricity growth, which is consistent with the current eccentricity estimations for the planets.

Finally, we performed an application of the new Posidonius version containing the creep tide equations to study tidally-induced transit timing variations (TTVs). Such field of

study is relatively new, with the first statistically significant tidally induced TTV detected presented in Yee et al. (2020). We have considered the case of K2-265 b , a small close-in super-Earth with a possible eccentricity value of $e = 0.15$. We performed analyses of TTVs for different spin-orbit configurations, such as the 3/2, 2/1 and 5/2 spin-orbit resonances. We verified that, among all possible resonant states, the 3/2 resonance provides the most optimistic values for the tidally-induced TTVs. Moreover, we verified that the major contribution to the TTVs comes from the orbital decay of the planet induced by tidal interactions. This effect is much larger than other generally considered effects such as the general relativity or the stellar oblateness. Even in the cases where general relativity effects are comparable to tidal effects to the TTVs, we verified that using occultation timing variations (OTVs) can break the degenerescence between these effects, since they have contributions which are opposite in sign to the OTVs. In terms of quantitative results, we verified that it is not yet possible to detect tidally-induced TTVs for K2-265 b considering the current timespan of transit event results we have. In terms of numerical values for the physical and orbital parameters of exoplanetary systems for which the detection of tidally-induced TTVs would be optimistic, we concluded that, for planets with a semi-major axis smaller than 0.02 AU, an amplitude of the tidally induced TTVs on the order of 20 – 80 s may be reached even for small observation timescales (on the order of 2 – 3 yr), provided that the stellar mass is between 0.5 and 1.0 Solar masses.

Bibliography

- Amard L., Palacios A., Charbonnel C., Gallet F., Georgy C., et al.: First grids of low-mass stellar models and isochrones with self-consistent treatment of rotation. From 0.2 to 1.5 M_{\odot} at seven metallicities from PMS to TAMS, *A&A*, 2019, vol. 631, p. A77
- Baluev R. V., Sokov E. N., Hoyer S., Huitson C., da Silva J. A. R. S., Evans P., Sokova I. A., Knight C. R., Shaidulin V. S., WASP-4 transit timing variation from a comprehensive set of 129 transits, *MNRAS*, 2020, vol. 496, p. L11
- Batygin K., Adams F. C., Magnetic and Gravitational Disk-Star Interactions: An Interdependence of PMS Stellar Rotation Rates and Spin-Orbit Misalignments, *ApJ*, 2013, vol. 778, p. 169
- Blanco-Cuaresma S., Bolmont E., Studying Tidal Effects In Planetary Systems With Posidonium. A N-Body Simulator Written In Rust.. In *EWASS Special Session 4 (2017): Star-planet interactions (EWASS-SS4-2017)* , 2017a
- Blanco-Cuaresma S., Bolmont E., What can the programming language Rust do for astrophysics?. In *Astroinformatics* , vol. 325, 2017b, p. 341
- Boisse I., Bouchy F., Hébrard G., Bonfils X., Santos N. C., Vauclair S., Disentangling stellar activity and planetary signals. In *European Physical Journal Web of Conferences* , vol. 11 of *European Physical Journal Web of Conferences*, 2011, p. 02005
- Bolmont E., Raymond S. N., Leconte J., Hersant F., Correia A. C. M., Mercury-T: A new code to study tidally evolving multi-planet systems. Applications to Kepler-62, *A&A*, 2015, vol. 583, p. A116

- Bouma L. G., Winn J. N., Baxter C., Bhatti W., Dai F., Daylan T., Désert J. M., Hill M. L., Kane S. R., Stassun K. G., Villaseñor J., Ricker G. R., Vanderspek R., Latham D. W., Seager S., Jenkins J. M., Berta-Thompson Z., Colón K., Fausnaugh M., Glidden A., Guerrero N., Rodríguez J. E., Twicken J. D., Wohler B., WASP-4b Arrived Early for the TESS Mission, *AJ*, 2019, vol. 157, p. 217
- Bouvier J., Forestini M., Allain S., The angular momentum evolution of low-mass stars., *A&A*, 1997, vol. 326, p. 1023
- Callegari N., Rodríguez Á., Dynamics of rotation of super-Earths, *Celestial Mechanics and Dynamical Astronomy*, 2013, vol. 116, p. 389
- Chambers J. E., A hybrid symplectic integrator that permits close encounters between massive bodies, *MNRAS*, 1999, vol. 304, p. 793
- Chandrasekhar S., *Ellipsoidal Figures of Equilibrium*. Yale University Press, New Haven, 1969, 252 p.
- Cloutier R., Astudillo-Defru N., Doyon R., Bonfils X., Almenara J. M., et al.: Confirmation of the radial velocity super-Earth K2-18c with HARPS and CARMENES, *A&A*, 2019, vol. 621, p. A49
- Correia A. C. M., Boué G., Laskar J., Pumping the Eccentricity of Exoplanets by Tidal Effect, *ApJ*, 2012, vol. 744, p. L23
- Correia A. C. M., Boué G., Laskar J., Rodríguez A., Deformation and tidal evolution of close-in planets and satellites using a Maxwell viscoelastic rheology, *A&A*, 2014, vol. 571, p. A50
- Correia A. C. M., Rodríguez A., On the Equilibrium Figure of Close-in Planets and Satellites, *ApJ*, 2013, vol. 767, p. 128
- Cram L. E., Kuhl L. V., Jordan S., Thomas R., Goldberg L., Pecker J.-C., FGK stars and T Tauri stars. vol. 502, 1989
- Darwin G. H., On the Secular Changes in the Elements of the Orbit of a Satellite Revolving about a Tidally Distorted Planet, *Philosophical Transactions of the Royal Society of London Series I*, 1880, vol. 171, p. 713

-
- Dittmann J. A., Irwin J. M., Charbonneau D., Bonfils X., Astudillo-Defru N., et al.: A temperate rocky super-Earth transiting a nearby cool star, *Nature*, 2017, vol. 544, p. 333
- Everhart E., An efficient integrator that uses Gauss-Radau spacings. In *IAU Colloq. 83: Dynamics of Comets: Their Origin and Evolution* , vol. 115 of *Astrophysics and Space Science Library*, 1985, p. 185
- Ferraz-Mello S., A rheophysical tidal theory for exoplanets and satellites. In *European Planetary Science Congress 2012* , 2012, p. EPSC2012
- Ferraz-Mello S., Tidal synchronization of close-in satellites and exoplanets. A rheophysical approach, *Celestial Mechanics and Dynamical Astronomy*, 2013, vol. 116, p. 109
- Ferraz-Mello S., Ferraz-Mello S., Tidal synchronization of close-in satellites and exoplanets: II. Spin dynamics and extension to Mercury and exoplanet host stars., *Celestial Mechanics and Dynamical Astronomy*, 2015, vol. 122, p. 359. [Errata: *Celest. Mech. Dyn. Astr.* 130, 78 (2018), p. 20], 2015
- Ferraz-Mello S., Beaugé C., Folonier H. A., Gomes G. O., Tidal friction in satellites and planets. The new version of the creep tide theory, *European Physical Journal Special Topics*, 2020, vol. 229, p. 1441
- Ferraz-Mello S., Rodríguez A., Hussmann H., Tidal friction in close-in satellites and exoplanets: The Darwin theory re-visited, *Celestial Mechanics and Dynamical Astronomy*, 2008, vol. 101, p. 171
- Ferraz-Mello S., Tadeu dos Santos M., Beaugé C., Michtchenko T. A., Self-consistent Determination of the Mass of the Super-Earth CoRoT-7b. In *AAS/Division of Dynamical Astronomy Meeting #41* , vol. 41 of *AAS/Division of Dynamical Astronomy Meeting*, 2010, p. 4.05
- Ferraz-Mello S., Tadeu Dos Santos M., Beaugé C., Michtchenko T. A., Rodríguez A., On the mass determination of super-Earths orbiting active stars: the CoRoT-7 system, *A&A*, 2011, vol. 531, p. A161

- Ferraz-Mello S., Tadeu dos Santos M., Folonier H., Csizmadia S., do Nascimento J. D. J., Pätzold M., Interplay of Tidal Evolution and Stellar Wind Braking in the Rotation of Stars Hosting Massive Close-In Planets, *ApJ*, 2015, vol. 807, p. 78
- Folonier H. A., Ferraz-Mello S., Andrade-Ines E., Tidal synchronization of close-in satellites and exoplanets. III. Tidal dissipation revisited and application to Enceladus, *Celestial Mechanics and Dynamical Astronomy*, 2018, vol. 130, p. 78
- Folonier H. A., Ferraz-Mello S., Kholshchevnikov K. V., The flattenings of the layers of rotating planets and satellites deformed by a tidal potential, *Celestial Mechanics and Dynamical Astronomy*, 2015, vol. 122, p. 183
- Goldreich P., Final spin states of planets and satellites, *AJ*, 1966, vol. 71, p. 1
- Gomes G. O., Bolmont E., Blanco-Cuaresma S., Influence of equilibrium tides on transit-timing variations of close-in super-Earths. I. Application to single-planet systems and the case of K2-265 b, *A&A*, 2021, vol. 651, p. A23
- Gomes G. O., Ferraz-Mello S., Tidal evolution of exoplanetary systems hosting potentially habitable exoplanets. The cases of LHS-1140 b-c and K2-18 b-c, *MNRAS*, 2020, vol. 494, p. 5082
- Gomes G. O., Folonier H. A., Ferraz-Mello S., Rotation and figure evolution in the creep tide theory: a new approach and application to Mercury, *Celestial Mechanics and Dynamical Astronomy*, 2019, vol. 131, p. 56
- Hansen B. M. S., Calibration of Equilibrium Tide Theory for Extrasolar Planet Systems, *ApJ*, 2010, vol. 723, p. 285
- Hansen B. M. S., Calibration of Equilibrium Tide Theory for Extrasolar Planet Systems. II, *ApJ*, 2012, vol. 757, p. 6
- Happel J., Brenner H., *Low Reynolds number hydrodynamics*. Martinus Nijhoff, 1983, 563 p.
- Hatzes A. P., Dvorak R., Wuchterl G., Guterman P., Hartmann M., Fridlund M., Gandolfi D., Guenther E., Pätzold M., An investigation into the radial velocity variations of CoRoT-7, *A&A*, 2010, vol. 520, p. A93

- Hut P., Tidal evolution in close binary systems., *A&A*, 1981, vol. 99, p. 126
- Irwin J., Berta Z. K., Burke C. J., Charbonneau D., Nutzman P., West A. A., Falco E. E.,
On the Angular Momentum Evolution of Fully Convective Stars: Rotation Periods for
Field M-dwarfs from the MEarth Transit Survey, *ApJ*, 2011, vol. 727, p. 56
- Jackson B., Miller N., Barnes R., Raymond S. N., Fortney J. J., Greenberg R., The roles
of tidal evolution and evaporative mass loss in the origin of CoRoT-7 b, *MNRAS*, 2010,
vol. 407, p. 910
- Kaltenegger L., Traub W. A., Transits of Earth-like Planets, *ApJ*, 2009, vol. 698, p. 519
- Kaula W. M., Tidal Dissipation by Solid Friction and the Resulting Orbital Evolution,
Reviews of Geophysics and Space Physics, 1964, vol. 2, p. 661
- Lam K. W. F., Santerne A., Sousa S. G., Vigan A., Armstrong D. J., Barros S. C. C.,
Brugger B., Adibekyan V., Almenara J. M., Delgado Mena E., Dumusque X., Barrado
D., Bayliss D., Bonomo A. S., Bouchy F., Brown D. J. A., Ciardi D., Deleuil M.,
Demangeon O., Faedi F., Foxell E., Jackman J. A. G., King G. W., Kirk J., Ligi R.,
Lillo-Box J., Lopez T., Lovis C., Louden T., Nielsen L. D., McCormac J., Mousis O.,
Osborn H. P., Pollacco D., Santos N. C., Udry S., Wheatley P. J., K2-265 b: a transiting
rocky super-Earth, *A&A*, 2018, vol. 620, p. A77
- Lanza A. F., Bonomo A. S., Moutou C., Pagano I., Messina S., Leto G., Cutispoto G.,
Aigrain S., Alonso R., Barge P., Deleuil M., Auvergne M., Baglin A., Collier Cameron
A., Photospheric activity, rotation, and radial velocity variations of the planet-hosting
star CoRoT-7, *A&A*, 2010, vol. 520, p. A53
- Laskar J., Large Scale Chaos and Marginal Stability in the Solar System, *Celestial Mecha-
nics and Dynamical Astronomy*, 1996, vol. 64, p. 115
- Leger A., Rouan D., Schneider J., Barge P., Fridlund M., Samuel B., Ollivier M., Guenther
E., Deleuil M., Deeg H. J., Auvergne M., Alonso R., Aigrain S., Alapini A., Almenara
J. M., Baglin A., Barbieri M., Bruntt H., Bordé P., Bouchy F., Cabrera J., Catala C.,
Carone L., Carpano S., Csizmadia S., Dvorak R., Erikson A., Ferraz-Mello S., Foing
Transiting exoplanets from the CoRoT space mission. VIII. CoRoT-7b: the first super-
Earth with measured radius, *A&A*, 2009, vol. 506, p. 287

- MacDonald G. J. F., Tidal Friction, *Reviews of Geophysics and Space Physics*, 1964, vol. 2, p. 467
- Mardling R. A., Lin D. N. C., Calculating the Tidal, Spin, and Dynamical Evolution of Extrasolar Planetary Systems, *ApJ*, 2002, vol. 573, p. 829
- Matsuyama I., Nimmo F., Gravity and tectonic patterns of Mercury: Effect of tidal deformation, spin-orbit resonance, nonzero eccentricity, despinning, and reorientation, *Journal of Geophysical Research (Planets)*, 2009, vol. 114, p. E01010
- McQuillan A., Mazeh T., Aigrain S., Stellar Rotation Periods of the Kepler Objects of Interest: A Dearth of Close-in Planets around Fast Rotators, *ApJ*, 2013, vol. 775, p. L11
- Ment K., Dittmann J. A., Astudillo-Defru N., Charbonneau D., Irwin J., et al.: A Second Terrestrial Planet Orbiting the Nearby M Dwarf LHS 1140, *AJ*, 2019, vol. 157, p. 32
- Mignard F., The Evolution of the Lunar Orbit Revisited. I., *Moon and Planets*, 1979, vol. 20, p. 301
- Mikkola S., Innanen K., Symplectic Tangent Map for Planetary Motions, *Celestial Mechanics and Dynamical Astronomy*, 1999, vol. 74, p. 59
- Montet B. T., Morton T. D., Foreman-Mackey D., Johnson J. A., Hogg D. W., et al.: Stellar and Planetary Properties of K2 Campaign 1 Candidates and Validation of 17 Planets, Including a Planet Receiving Earth-like Insolation, *ApJ*, 2015, vol. 809, p. 25
- Pätzold M., Endl M., Csizmadia S., Gandolfi D., Jorda L., et al.: Transiting exoplanets from the CoRoT space mission. XXIII. CoRoT-21b: a doomed large Jupiter around a faint subgiant star, *A&A*, 2012, vol. 545, p. A6
- Pecaut M. J., Mamajek E. E., Bubar E. J., A Revised Age for Upper Scorpius and the Star Formation History among the F-type Members of the Scorpius-Centaurus OB Association, *ApJ*, 2012, vol. 746, p. 154
- Penev K., Bouma L. G., Winn J. N., Hartman J. D., Empirical Tidal Dissipation in Exoplanet Hosts From Tidal Spin-up, *AJ*, 2018, vol. 155, p. 165

-
- Penev K., Jackson B., Spada F., Thom N., Constraining Tidal Dissipation in Stars from the Destruction Rates of Exoplanets, *ApJ*, 2012, vol. 751, p. 96
- Penev K., Zhang M., Jackson B., POET: A Model for Planetary Orbital Evolution Due to Tides on Evolving Stars, *PASP*, 2014, vol. 126, p. 553
- Perry M. E., Neumann G. A., Phillips R. J., Barnouin O. S., Ernst C. M., et al.: The low-degree shape of Mercury, *Geophys. Res. Lett.*, 2015, vol. 42, p. 6951
- Pont F., Husnoo N., Mazeh T., Fabrycky D., Determining eccentricities of transiting planets: a divide in the mass-period plane, *MNRAS*, 2011, vol. 414, p. 1278
- Queloz D., Bouchy F., Moutou C., Hatzes A., Hébrard G., Alonso R., Auvergne M., Baglin A., Barbieri M., Barge P., Benz W., Bordé P., Deeg H. J., Deleuil M., Dvorak R., Erikson A., Ferraz Mello S., Fridlund M., Gandolfi D., Gillon M., Guenther E., Guillot T., Jorda L., Hartmann M., Lammer H., Léger A., Llebaria A., Lovis C., Magain P., Mayor M., Mazeh T., Ollivier M., Pätzold M., Pepe F., Rauer H., Rouan D., Schneider J., Segransan D., Udry S., Wuchterl G., The CoRoT-7 planetary system: two orbiting super-Earths, *A&A*, 2009, vol. 506, p. 303
- Ragozzine D., Wolf A. S., Probing the Interiors of very Hot Jupiters Using Transit Light Curves, *ApJ*, 2009, vol. 698, p. 1778
- Rein H., Liu S. F., REBOUND: an open-source multi-purpose N-body code for collisional dynamics, *A&A*, 2012, vol. 537, p. A128
- Rein H., Spiegel D. S., IAS15: a fast, adaptive, high-order integrator for gravitational dynamics, accurate to machine precision over a billion orbits, *MNRAS*, 2015, vol. 446, p. 1424
- Rein H., Tamayo D., WHFAST: a fast and unbiased implementation of a symplectic Wisdom-Holman integrator for long-term gravitational simulations, *MNRAS*, 2015, vol. 452, p. 376
- Rodríguez A., Callegari N., Correia A. C. M., Coupled orbital and spin evolution of the CoRoT-7 two-planet system using a Maxwell viscoelastic rheology, *MNRAS*, 2016, vol. 463, p. 3249

- Rodríguez A., Ferraz-Mello S., Michtchenko T. A., Beaugé C., Miloni O., Tidal decay and orbital circularization in close-in two-planet systems, *MNRAS*, 2011, vol. 415, p. 2349
- Saha P., Tremaine S., *Symplectic Integrators for Solar System Dynamics*, *AJ*, 1992, vol. 104, p. 1633
- Sarkis P., Henning T., Kürster M., Trifonov T., Zechmeister M., et al.: The CARMENES Search for Exoplanets around M Dwarfs: A Low-mass Planet in the Temperate Zone of the Nearby K2-18, *AJ*, 2018, vol. 155, p. 257
- Tamayo D., Rein H., Shi P., Hernandez D. M., REBOUNDx: a library for adding conservative and dissipative forces to otherwise symplectic N-body integrations, *MNRAS*, 2020, vol. 491, p. 2885
- Teitler S., Königl A., Why is there a Dearth of Close-in Planets around Fast-rotating Stars?, *ApJ*, 2014, vol. 786, p. 139
- Wisdom J., Holman M., Symplectic maps for the N-body problem., *AJ*, 1991, vol. 102, p. 1528
- Yee S. W., Winn J. N., Knutson H. A., Patra K. C., Vissapragada S., Zhang M. M., Holman M. J., Shporer A., Wright J. T., The Orbit of WASP-12b Is Decaying, *ApJ*, 2020, vol. 888, p. L5

Appendix

Appendix A

Structure and usage of Posidonius

In this Appendix we discuss the structure and installation guide of the Posidonius code, as it is currently given in this GitHub repository. Such a version contains all the improvements in the numerical integrator subroutines (such as corrections for non-conservative forces when using WHFast) as well as optimizations for the inclusion of the tidal interactions using the creep tide equations. We mention that several parts of this Appendix are based on the official Posidonius installation and usage guide made available at <https://github.com/marblestation/posidonius>.

A.1 Installation of requirements

Posidonius uses both Rust and Python programming languages. Thus, it is mandatory that both a Rust compiler and a Python interpreter are installed in the local machine. For Rust, one can perform the download of the compiler in the link <https://rustup.rs/>, while Python interpreter and package manager can be installed using anaconda through <https://www.anaconda.com/products/individual>.

After installing both Python and Rust, the Posidonius package must be installed from the GitHub repository. To clone the GitHub repository to the local machine, use `git clone https://github.com/gabogomes/posidonius.git`. Afterwards, the directory will be downloaded in a new directory in the local machine. The Posidonius code is then ready to be installed.

A.2 Installation of Posidonius

First, we should install the N-body simulator by running, from the current directory, the following line of command in the command line interface:

```
cargo install --path . --force.
```

The executable will be copied into HOME/.cargo/bin/. Then, install the python package to create cases by running:

```
curl -O https://www.cfa.harvard.edu/~sblancoc/posidonius/input.tar.gz
tar -zxvf input.tar.gz && rm -f input.tar.gz
python setup.py install --user
```

A.3 Code structure and functioning

The Posidonius package is composed by two parts: the Python wrapper (which is used to plot results, prepare initial conditions files and transform binary files in text files), and the Rust source code (which performs the numerical integrations)¹. We show (in a diagram format) the structure of the two aforementioned parts of Posidonius in Fig. A.1

It is important to comment that the most important directory when it comes to adding new effects in Posidonius (which is a relatively easy task since the effects are completely uncoupled) is the effects directory in both the src and the posidonius directories. For instance, to add the creep tide equations we modified the files effects/tides which, for the sake of organization, has been divided in two files (in the Rust src directory) for a better organization and generalization in case other tidal models are added in the future.

Regarding the functioning of the code, we provide in Fig. A.2 a diagram showing the functioning of the code from the initial conditions file until the output procedure of the time evolution data.

In a more detailed description, we have: the initial python script file containing the specifications of the simulation (orbital elements, number of bodies of the system, interactions to be taken into account, timestep for writing data in the output files and numerical inte-

¹ Additional directories, functions and modules exist, although they are used mainly for development and testing the code. Thus, they are not explicitly cited or described here.

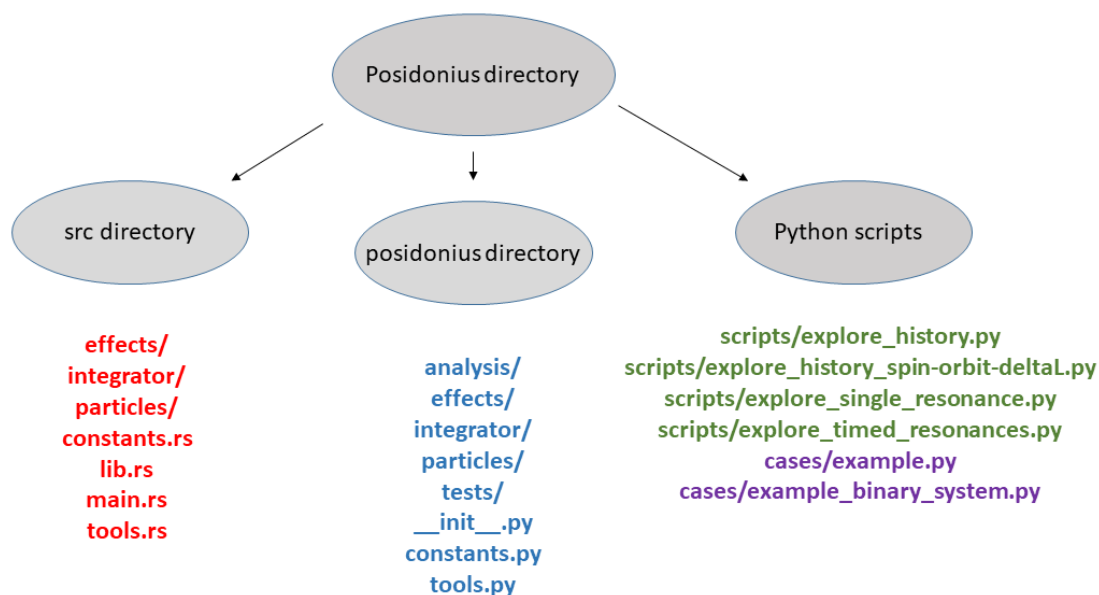


Figure A.1: Structure of Posidonius: src directory (with Rust codes for integration), the Python wrapper of Posidonius Rust code (in the middle) and the main script files for generating plots (on the top, in green) and initial condition files (on the bottom, in purple).

grator to be used). The python script is then transformed in a JSON file which is readable by the Rust code. By executing the Rust code, the numerical integration is performed all the way in the Rust language, without interactions with the Python wrapper (although it is possible to generate Python plots of preliminary data in the middle of an ongoing numerical integration). Afterwards, a Python scripts transforms the binary format files (containing the time evolution of the system parameters) into text files and plots.

A.4 Performing simulations

Now we discuss the specific commands to be used in the command line to perform the simulations using Posidonius. The Posidonius simulations are performed based on a initial conditions file which must be given in JSON format, which is generated by means of a Python script containing the initial conditions and physical parameters of the system. For instance, to generate a initial conditions JSON file corresponding to one of the simulations presented in Gomes et al. (2021), one can use

```
python cases/Gomes_et_al_2021/K2-265b.py target/K2-265b.json
```

To run a simulation based on the file generated after the compilation of the code above,

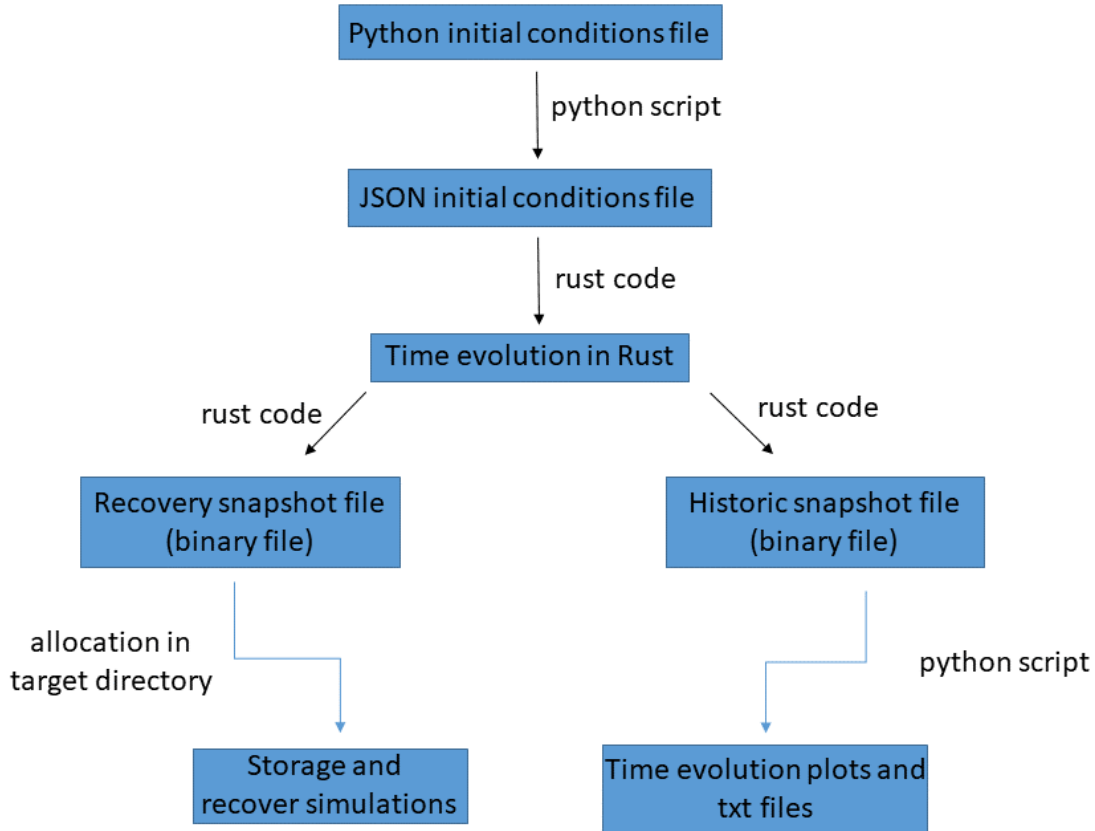


Figure A.2: Functioning of Posidonius, from the top to the bottom. More details are given in the main text.

one can use

```
posidonius start target/K2-265b.json target/K2-265b.bin
target/K2-265b_history.bin
```

To resume a simulation which was previously stopped, we can use

```
posidonius resume target/K2-265b.bin target/K2-265b_history.bin
```

Note that, differently from the start command, we do not need the JSON initial conditions file to resume a simulation, since the initial conditions are taken as the last timestep values of the system, which are written in the binary history file.

A.5 Plotting and analysing results

To plot results of the spin and orbital parameters of a given simulation, we can use

```
python scripts/explore_history.py target/K2-265b.json target/K2-265b_history.bin
```

To explore more specific results such as mean-motion resonances which may be present in the system, we can type

```
python scripts/explore_timed_resonances.py target/K2-265b_history.bin
```

We would like to mention that the Python scripts to generate figures and plots are well documented and can be modified by the user to select specific parameters to be plotted in the figures, according to the specific need.